



**Search for New Massive Long-Lived Neutral Particles  
decaying to Photons in  $pp$  Collisions at  $\sqrt{S} = 8$  TeV**

A DISSERTATION  
SUBMITTED TO THE FACULTY OF THE GRADUATE SCHOOL  
OF THE UNIVERSITY OF MINNESOTA  
BY

Tambe Ebai Norbert

IN PARTIAL FULFILLMENT OF THE REQUIREMENTS  
FOR THE DEGREE OF  
Doctor of Philosophy

Prof. Yuichi Kubota

July, 2015

**© Tambe Ebai Norbert 2015  
ALL RIGHTS RESERVED**

# Acknowledgements

Humility is not about thinking less of yourself, rather, humility is thinking about yourself less.

There are many people that have earned my gratitude for their contribution to my time in graduate school.

I want to thank my supervisor Prof. Yuichi Kubota, who gave me countless failure-tolerant opportunities throughout my PhD. Before I knew him, the fear of failure always did paralyzed me, not anymore.

*The universe is unbiased, she chooses to reveal herself to all who have the correct attitude.*

Tambe E. Norbert

*So I would claim you are profoundly misled by thinking about physics as similar to logic or number theory. Its not! its dynamical evolution, and most results of physics problems are not nice numbers like 1 or  $\pi$  or even  $e^\pi$ .*

by Prof. Matt Strassler

# Dedication

What ever it is that doesnt workout, get up...I think youve got to realized that there is no personal ambition you have which can be extinguished by anybody else...Only YOU by giving up your dreams can extinguish them. And if your dreams doesnt work out EXACTLY like you intended, it will still take you someplace interesting and you will make a DIFFERENCE. So, DONT be AFRAID TO FAIL because you probably will whether you are afraid to or not and it's scary. You just gotta get out. The world belongs to tomorrow not yesterday. Dont give anybody else permission to take your life away, just keep living and keep giving and never make the perfect enemy the good.Never think that what Im doing is too little to make a difference, THAT'S NOT TRUE!, THAT'S NOT TRUE! Do something everyday. Someday, for all of us, it will be our last day and what would matter will be all the steps we took along the way and what they amounted to, NOT the home run we hit on day X. I wish you well.

US Pres Bill Clinton, Dallas, TX

*No, I have nothing against Mr. Einstein. He is a kind person and has done many good things, some of which will become part of the music. I will write to him and try to explain that the ether exists, and that its particles are what keep the Universe in harmony, and the life in eternity.*

Nikola Tesla

*The Universe is unbiased, she chooses to reveal herself to whomever she wants.*

Tambe E. Norbert

## Abstract

We have performed a search for events with delayed photons and large missing transverse momentum from the decay of neutral long-lived particles produced in proton-proton collisions with a center of mass energy,  $\sqrt{S} = 8$  TeV at the LHC. Capitalizing on the excellent time resolution of the CMS electromagnetic calorimeter, we searched for events with delayed photons using the measured photon arrival time at the electromagnetic calorimeter. We observed a single event, consistent with our background expectations from the standard model and proceeded to set limits on the cross section,  $\sigma_{\tilde{\chi}_1^0} > 0.02$  pb, for the production and decay of the lightest neutralino ( $\tilde{\chi}_1^0$ ) with mass,  $m_{\tilde{\chi}_1^0} \geq 235$  GeV/ $c^2$ , and lifetime,  $\tau_{\tilde{\chi}_1^0} \geq 35$  ns, according to an R-parity conserving gauge mediated supersymmetry breaking model. We show, for the first time, that using only the timing information of the CMS electromagnetic calorimeter, the CMS detector is sensitive to neutralinos with lifetimes up to 30 ns and masses up to 260 GeV/ $c^2$ . Description of timing measurement by the electromagnetic calorimeter and its performance are presented.

# Contents

<b>Acknowledgements</b>	<b>i</b>
<b>Dedication</b>	<b>ii</b>
<b>Abstract</b>	<b>iii</b>
<b>List of Tables</b>	<b>vii</b>
<b>List of Figures</b>	<b>ix</b>
<b>1 Introduction</b>	<b>1</b>
<b>2 Phenomenology of Long-Lived Particles</b>	<b>6</b>
2.1 The Standard Model of Particle Physics . . . . .	6
2.1.1 Main Components of the SM . . . . .	7
2.1.2 Spontaneous Symmetry Breaking . . . . .	13
2.1.3 Limitations of the Standard Model . . . . .	16
2.2 Beyond Standard Model Physics . . . . .	17
2.2.1 Supersymmetry . . . . .	18
2.2.2 Minimal Supersymmetric Standard Model . . . . .	19
2.3 Gauge Mediated Supersymmetry Breaking Models . . . . .	23
2.3.1 Phenomenology . . . . .	23
2.3.2 Long-Lived Particles in GMSB Models . . . . .	25
2.4 Previous Search Experiments . . . . .	31

<b>3 Hadron Collider and Detector</b>	<b>33</b>
3.1 Large Hadron Collider . . . . .	33
3.1.1 Overview . . . . .	33
3.1.2 Colliding Energy . . . . .	34
3.1.3 Luminosity . . . . .	35
3.1.4 LHC Bunch Structure . . . . .	36
3.2 Compact Muon Solenoid . . . . .	40
3.2.1 Overview . . . . .	40
3.2.2 Calorimeter . . . . .	42
3.2.3 Muon Chambers . . . . .	47
3.2.4 Triggering . . . . .	49
<b>4 Time Reconstruction and Resolution</b>	<b>50</b>
4.1 Electromagnetic Calorimeter Readout Electronics . . . . .	50
4.2 Time Reconstruction . . . . .	52
4.3 ECAL Time Performance from Test Beam . . . . .	54
4.3.1 ECAL Time Resolution . . . . .	54
4.4 ECAL Time Performance from Collision . . . . .	56
4.4.1 Time Calibrations . . . . .	57
4.4.2 Time Bias . . . . .	62
4.4.3 ECAL Time Performance With Z Events . . . . .	64
<b>5 Event Reconstruction</b>	<b>68</b>
5.1 Event Reconstruction Overview . . . . .	68
5.2 Supercluster Reconstruction . . . . .	68
5.3 Track and Vertex Reconstruction . . . . .	70
5.4 Photon and Electron Reconstruction . . . . .	71
5.5 Muon Reconstruction . . . . .	74
5.6 Jet Reconstruction . . . . .	76
5.7 Missing Transverse Energy Reconstruction . . . . .	77
5.8 Anomalous Signals . . . . .	78

<b>6 Search Analysis for Long-Lived Particles</b>	<b>80</b>
6.1 Analysis Strategy . . . . .	80
6.1.1 Signal Modeling . . . . .	82
6.1.2 Background Modeling . . . . .	83
6.1.3 Datasets . . . . .	83
6.1.4 ECAL Time . . . . .	87
6.2 Event Selection . . . . .	96
6.2.1 Trigger Selection . . . . .	97
6.2.2 Offline Selection . . . . .	98
6.3 Background Estimation . . . . .	101
6.3.1 Collision Background . . . . .	102
6.3.2 Non-Collision Background . . . . .	103
6.3.3 Event Vetoing, Performance and Fake Rates . . . . .	109
6.3.4 Background Estimation with ABDC Method . . . . .	112
6.3.5 Background Estimation Cross Check . . . . .	116
6.4 Systematic Studies . . . . .	122
6.5 Results . . . . .	124
<b>7 Statistical Analysis</b>	<b>125</b>
7.1 Limit Computation . . . . .	125
7.1.1 CLs Technique . . . . .	126
7.1.2 Statistical Test Formalism . . . . .	127
7.1.3 Test Statistics and $p$ -values . . . . .	129
<b>8 Limit Interpretation</b>	<b>133</b>
8.1 Signal Efficiency and Acceptance . . . . .	133
<b>9 Conclusion</b>	<b>138</b>
<b>Bibliography</b>	<b>139</b>
<b>Appendix A. Glossary and Acronyms</b>	<b>144</b>
A.1 Glossary . . . . .	144
A.2 Acronyms . . . . .	144

# List of Tables

2.1	SM particles and their gauge multiplets(representation) with quantum numbers. the numbers for example ( <b>3</b> , <b>2</b> , $\frac{1}{6}$ ) means ( <i>triplet, doublet, Y = 1/6</i> ) representations. . . . .	13
2.2	Supermultiplets and particle spin in SM and Supersymmetry. . . . .	19
2.3	Chiral supermultiplets and representation in Minimal Supersymmetric SM (MSSM). Super symmetric particles (sparticles) have a $\sim$ on them. Spin -0 fields are complex scalars while spin-1/2 fields are left-handed two component Weyl fermions. . . . .	20
2.4	Gauge supermultiplets and representations in Minimal Supersymmetric SM (MSSM). Super symmetric particles (sparticles) have a $\sim$ on them. . . . .	20
3.1	LHC operation parameter conditions during RUN 1, 2010-2013 . . . . .	39
3.2	CMS detector material, [22], and resolution(Time resolution: $N \approx 35$ ns, $\bar{C} \approx 0.070$ ns [39]) . . . . .	42
4.1	ECAL timing resolution absolute time and single precision for 2011 and 2012 of LHC Run 1 . . . . .	67
5.1	Simple cut-based selection criteria for electron and photon identification. . . . .	74
6.1	Data samples and their corresponding integrated luminosity totaling $19.1 \text{ fb}^{-1}$ used in the our delayed photon search analysis . . . . .	84
6.2	Signal GMSB SPS8 Monte Carlo samples for different $\Lambda$ with $50 \text{ cm} < c\tau < 1000 \text{ cm}$ and Branching Ratios (BR) studied in this analysis . . . . .	85
6.3	The $\gamma +$ jets samples studied in this analysis . . . . .	85
6.4	The photon identification and selection criteria used in this analysis . . . . .	99
6.5	The Jet ID and MET selection used in this analysis . . . . .	100
6.6	Fake rates for different non-collision vetoing. . . . .	110

6.7	Summary of missing transverse expectation for events with out-of-time photons. . . . .	111
6.8	ABCD Control Samples (CSs) definitions used for estimating non-collision background events in the signal CS D. Events must satisfy the $\cancel{E}_T > 60 \text{ GeV}$ selection requirement. . . . .	112
6.9	$A' B' C' D'$ and $I I'$ Control Samples (CSs) used for estimating collision background events contamination to CSs B and D. Events here must satisfy $\cancel{E}_T^\gamma > 60 \text{ GeV}$ selection requirements. . . . .	113
6.10	Event yields used in validity test for the ABCD background estimation method using 0 and 1-jet events sample. Beam halo/cosmic/spikes yields are obtained from tagged events. Events must pass photon, jet and $E_T^{\text{miss}}$ selection requirements. . . . .	115
6.11	Summary of systematic uncertainties for signal efficiency and background estimation in this analysis and applied to our final results. . . . .	123
6.12	Event yields used in our final background estimation for signal candidate events with at least a single photon and at least 2 jets, $\cancel{E}_T^\gamma > 60 \text{ GeV}$ , and $\cancel{E}_T > 60 \text{ GeV}$ . . . . .	124
8.1	Final number for $\Lambda = 180 \text{ TeV}$ GMSB SPS8 MC signal events events passing our selection cuts. . . . .	134
A.1	Acronyms . . . . .	145

# List of Figures

2.1	Higgs boson “Mexican hat” potential, $V(\phi^*\phi) = \mu^2(\phi^*\phi) + \lambda(\phi^*\phi)^2$ , which leads to spontaneous symmetry breaking with choice of parameters $\mu^2 < 0$ , $\lambda > 0$ . . . . .	15
2.2	SM particles and their interactions with vector bosons as mediators. . . . .	15
2.3	Higgs mass contributions from its coupling to fermions (a) and scalar (b) fields. . . . .	17
2.4	Supersymmetry particle mass spectra in the SPS8 or minimal GMSB (mGMSB) model. . . . .	22
2.5	Feynman diagrams of gravitino/golstino, $\tilde{G}$ , gaugino and scalar interactions with superpartner pairs $(\psi, \phi)$ scalar (a) and $(\lambda, A)$ gaugino (b) decay to gravitino. . . . .	24
2.6	Supersymmetry production cross-section against sparticle mass for different modes of supersymmetry production at a proton-proton collider. $pp \rightarrow \tilde{g}\tilde{g}$ processes have the dominant production cross section. . . . .	26
2.7	Feynmann diagrams for neutralino production from the cascade decay of a produced gluino ( <i>top</i> ) and squark ( <i>bottom</i> ). The final event has a single ( <i>left diagrams</i> ) or double photons ( <i>right diagrams</i> ) neutralino decay at LHC. . . . .	28
2.8	Neutralino lifetime and mass upper limit from ATLAS(left) and CMS(right) 7 TeV analysis with non-pointing photons and MET. . . . .	32
3.1	Schematic diagram showing the full Large hadron Collider. . . . .	34
3.2	Cumulative luminosity versus day delivered to (blue), and recorded by CMS (orange) during stable beams and for p-p collisions at 8 TeV center-of-mass energy in 2012. . . . .	36

3.3	Longitudinal Profile taken with Longitudinal Density Monitor (LDM) detector showing definition of Ghost/Satellite bunches with respect to main bunches. . . . .	37
3.4	(left)Arrival time distribution(red) of ATLAS MBTS for LHC fill 1533 during 2010 Pb-Pb run and LDM profile(black) for Beam2(same for Beam1). (Right) Timing of Clusters in the CMS endcap calorimeters for fill 1089:Left: EEP detector(left side of IP $z > 0$ ) Right: EEM detector( right side of IP, $z < 0$ ). Plots from ATLAS [30] and CMS, [31] . . . . .	38
3.5	CMS Detector showing the different subdetectors and their material. . .	41
3.6	CMS detector schematic view with definition of $x - y - z$ coordinates. .	41
3.7	Schematic diagram of CMS calorimetry system with HCAL enclosing ECAL in the Barrel and Endcap regions. . . . .	43
3.8	Layout of the CMS electromagnetic calorimeter showing the arrangement of crystal modules, supermodules in the barrel with the preshower in front of endcap with supercrystals. . . . .	48
3.9	Cross section view showing the coverage range of CMS sub-detectors and their longitudinal distance from the IP. . . . .	48
4.1	Schematic diagram of the CMS ECAL electronics readout for a single channel(Left) and the entire Trigger Tower or Front End (FE) Card(Right).	52
4.2	(a) A measured ECAL pulse shape for a single channel. (b) $\mathbf{T} - \mathbf{T}_{\max}$ Vs $R(T)$ relationship whose inverse is $T(R)$ . Solid line is pulse shape from test beam while dots are typical 10 discrete samples corresponding to signal from proton-proton collision. . . . .	53
4.3	Difference in the time measurements as a function of $A_{eff}/\sigma_n$ of two crystals sharing an energy and belonging to the same electromagnetic shower obtained during electron testbeam measurements. The single crystal energy scales for barrel (EB) and endcap (EE) is overlaid. The fitted results give $N = (35.1 \pm 0.2)$ ns and $\bar{C} = (20 \pm 4)$ ns. . . . .	56

4.4	<i>Top 3:</i> Time calibration maps showing the distribution of mean time for each channel/PbWO <sub>4</sub> crystal in EB (top) and EE (below: EE-(left), EE+(right)) before calibration. <i>Bottom 3:</i> Time calibration maps showing the distribution of mean time after calibration. After calibration most crystals have an average time of zero( <b>GREEN</b> ). . . . .	60
4.5	Distribution of mean time ( $\mu$ , <i>top row</i> ) and time deviation ( $\sigma$ , <i>bottom row</i> ) as a function of crystal energy for EB prior (left) and after (right) time bias corrections depending on energy have been applied. . . . .	63
4.6	Distribution of the time standard deviation ( $\sigma$ ) against crystal geometrical position, $\eta$ , in the ECAL barrel. Almost flat distribution of $\sigma$ with $\eta$ . . . . .	64
4.7	Ecal time difference between the two reconstructed electrons in $Z \rightarrow e^-e^+$ decay. The electron time is the seed (crystal with highest energy deposit) time with additional correction due to the time of flight of the electron in EB and EE . . . . .	65
4.8	Ecal absolute time of a single reconstructed electron in $Z \rightarrow e^-e^+$ decay. The electron time is the seed (crystal with highest energy deposit)time of the electron in EB and EE . . . . .	66
4.9	Timing resolution from: <i>left:</i> Two most energetic crystals in the same readout unit, <i>right:</i> Two most energetic crystals belonging to different readout units, as a function of effective amplitude( $A_{eff} = A_1 A_2 / \sqrt{A_1^2 + A_2^2}$ ) normalized to noise in EB. Both crystals are from reconstructed electrons in $Z \rightarrow e^-e^+$ events. . . . .	67
5.1	Superclustering algorithm direction in the $(\eta, \phi)$ plane in EB and fraction of electromagnetic shower energy coverage in a crystal energy matrix. .	69
5.2	$Z$ mass distribution from $Z \rightarrow e^+e^-$ decay showing improvement in the measurement of the $Z$ mass after performing energy adjustments to account for intrinsic spread in crystal, photo-detector response and time-dependent corrections to compensate for channel response loss for EB (right) and EE (left) . . . . .	72

5.3	Z mass reconstructed using electron superclusters shows improvement in Z mass measurement after applying energy adjustment at superclusters for EB (right) and EE (left). . . . .	73
5.4	Illustration of muons from proton-proton collision, cosmic rays and beam halo. (a) Muons from collision propagating from the center and moving outwards, (b) Cosmic muons traveling through the detector leaving signals in opposite hemispheres of the muon system, (c) Cosmic muons leaving signals in the tracker and opposite hemispheres, (d) cosmic muons entering and leaving the detector without passing through the muon detector layers, (e) beam halo muons penetrating the detector and leaving signals in the endcaps and (f) Cosmic muons entering the detector through the endcap and leaving through the barrel and which can happen in a <i>vice-versa</i> manner. . . . .	75
6.1	Number of photons (top left), Number of jets (top right) and $E_T^{\text{miss}}$ (bottom) for events with $\tilde{\chi}_1^0$ decay to $\gamma$ and $\tilde{G}$ for different $c\tau = 2000 \text{ mm}, 4000 \text{ mm}, 6000 \text{ mm}$ points of $\Lambda = 180 \text{ TeV}$ of the SPS8 model. A $\gamma+\text{jet}$ with $120 < p_T^{\gamma} < 170 \text{ GeV}/c$ sample shown for comparison with the signal samples. . . . .	86
6.2	Measuring the photon time using either seed time (black) or average time (blue). $\sigma$ of the Gaussian fit from seed time slightly better average time which is computationally intensive. . . . .	88
6.3	Pulse shape profile(left) showing a spike (solid line) and a true EM shower (dashed line) from data. The $\chi^2$ against ECAL time distribution(right) shows spikes misidentified as photons with very large $\chi^2$ and negative ECAL time. The region of $\chi^2 > 4$ is mostly dominated by spikes events. . . . .	89
6.4	ECAL time distributions of in-time photons from MC $\gamma+\text{jets}$ (blue) and data (red) samples before (left) and after (right) we adjusted the photon time from MC. . . . .	90
6.5	Neutralino transverse momentum ( $p_T^{\tilde{\chi}_1^0}$ ) distribution (top left) and transverse distance traveled (top right). Transverse momentum (bottom left) and time (bottom right) of photon from neutralino decay for different $\Lambda$ and $c\tau$ points in GMSB SPS8 model. . . . .	92

6.6	Schematic diagram showing $\tilde{\chi}_1^0 \rightarrow \gamma + \tilde{G}$ decay topology within the ECAL volume of the CMS detector ( <i>Left</i> ). The estimated photon arrival time at ECAL from the decay of $\tilde{\chi}_1^0$ in the SPS8 model with $m_{\tilde{\chi}_1^0} = 256 \text{ GeV}/c^2$ and $c\tau = 600 \text{ cm}$ ( <i>Right</i> ). . . . .	93
6.7	ECAL timing distribution of photons in barrel ( <b>EB</b> ), endcap ( <b>EE</b> ) and all of ECAL (ALL ECAL) with $p_T > 50 \text{ GeV}$ from data. A 2.5 ns delay timing structure is observed in endcaps. . . . .	94
6.8	Our HLT trigger efficiency turn-on curves for photon $p_T$ (right) and event $\cancel{E}_T$ (left). The $\gamma + \text{jets}$ samples require photon $p_T > 170 \text{ GeV}/c$ . . . . .	98
6.9	Comparing ECAL time distribution of events with different jet multiplicity from small sample of data and a single GMSB $\Lambda = 180 \text{ TeV}$ and $c\tau = 6000 \text{ mm}$ sample. Accepted photons must have $p_T > 60 \text{ GeV}$ . . . . .	100
6.10	ECAL time against $\eta$ (left) and ECAL time against $\phi$ (right) for photons with $p_T > 60 \text{ GeV}$ from data. . . . .	101
6.11	(Left) ECAL time $V.s \Delta\phi(\text{CSC Seg}, \gamma)$ for in time(black) and out-of-time(red and blue) photons. (Right) Photon ECAL time $V.s \eta$ , expected halo photon time is shown as two red lines. . . . .	105
6.12	Using $\Delta\phi(\text{CSC Seg}, \gamma) < 0.05$ to tag photons with $\phi_\gamma = 0, \pm\pi$ in the endcaps. A good portion of endcap photon candidates are tagged. . . . .	105
6.13	Scatter plot showing $\Delta\eta(\text{DT Seg}, \gamma)$ against $\Delta\phi(\text{DT Seg}, \gamma)$ for out-of-time ( $t_\gamma > 2 \text{ ns}$ and $t_\gamma < -3 \text{ ns}$ ) photons (right) compared to in-time( $ t_\gamma  < 1 \text{ ns}$ ) photons (left). Cosmic photon candidates have small $\Delta\eta$ and $\Delta\phi$ . . . . .	107
6.14	Scatter plot of $\Delta\eta(\text{DT Seg}, \gamma)$ against $\Delta\phi(\text{DT Seg}, \gamma)$ for photons from pure cosmic muon data. Small $\Delta\eta$ and $\Delta\phi$ are cosmic photons. . . . .	107
6.15	<i>Number of crystals</i> in photon supercluster plot (Left) for in-time photon candidates (black), spike photon candidates (magenta) and halo photon candidates (red). The spike photon candidates are selected with an energy swiss-cross variable ( $1 - E_4/E_1$ ) (right) shown comparing in-time photons ( $ t_\gamma  < 1.0$ ) to spike candidate sample selected with $S_{\text{Minor}}$ and $S_{\text{Major}}$ variables. . . . .	109

6.16	ECAL photon time for a data sample of 0 and 1-jet events showing our tagging performance for non-collision background events. . . . .	110
6.17	ECAL time $Vs \eta$ (top plots) and $Vs \phi$ (bottom plots) for photon candidates from <b>SinglePhoton</b> dataset (left) compared to electron candidates from the <b>DoubleElectron</b> dataset (right). All photons or electron candidates are in barrel subdetector. Most of the photons with $\phi = 0, \pm\pi$ are halo photons which are not observed in the Z boson candidate sample.	117
6.18	Di-electron mass distribution (left) and the time (right) of the two electron candidates for the signal $76 < m_{e^+e^-} < 100$ GeV/ $c^2$ Z boson sample and for sideband sample ( $50 < m_{e^+e^-} < 76$ GeV/ $c^2$ and $100 < m_{e^+e^-} < 130$ GeV/ $c^2$ ). Events are from the <b>Single/DoubleElectron</b> data sample.	119
6.19	<i>Top:</i> Polynomial fit (red & blue lines) of the di-electron invariant mass of candidate Z events for the sideband control sample (left) only and all Z events (right). <i>Bottom:</i> Fitting the total Z event sample with template extracted from fitting the sideband CS to extract the scale factor use for estimating the background event contribution in true Z signal events sample. . . . .	120
6.20	ECAL time distribution of genuine Z bosons after background contribution is subtracted. . . . .	121
7.1	Sampling distributions for $f(t_\mu \mu)$ showing how one extracts the $p$ -vlaues. left: is the using a analytic of the Asymptotic method and right: is from the HybridNew method. . . . .	130
7.2	Distribution of $p$ -vlaues showing how upper limit on $\mu$ is extracted for a given threshold probability. . . . .	132
8.1	The reconstruction and selection efficiency (left) $\times$ Acceptance ( $t > 3$ ns) (right) against transverse decay length in laboratory frame for different $c\tau$ points. . . . .	134
8.2	Neutralino production cross section against proper delay length upper limit interpretation in SPS8 model. (Left) $\Lambda = 100$ TeV, (Right)(left) $\Lambda = 180$ TeV . . . . .	135

8.3	Neutralino production cross section against neutralino mass upper limit at 95% confidence levels interpretation in SPS8 model.(Left) $C\tau = 11000$ mm, (Right) $C\tau = 6000$ mm . . . . .	136
8.4	Neutralino two dimensional exclusion limit of neutralino mass ( $\Lambda$ ) against proper delay length upper limit interpretation in SPS8 model in the decay $\tilde{\chi}_1^0 \rightarrow \gamma + \tilde{G}$ with limits from previous experiments shown. . . . .	137

# Chapter 1

## Introduction

Astronomical observations such as gravitational lensing and galaxy rotation curves and precision cosmology studies through the Wilkinson Microwave Anisotropy Probe by a NASA Explorer mission, all indicate the presence of a new form of matter in the universe which only interacts significantly with visible matter through gravity [1]. This illusive matter in the universe, also known as *Dark Matter* (DM), does not emit or scatter off electromagnetic radiation and makes up about 23% of the universe. There have been no reports on the direct detection of DM and its supposed existence is one of the strongest indications for a new kind of physics beyond the standard model of particle physics, as no known particles of the standard model can be attributed to dark matter.

Visible matter, which does emit and can scatter off electromagnetic radiation, make up only 4.5% of the total matter in the universe and its properties like its particle content and their interactions, are best understood through simple symmetries of nature known as *gauge symmetries*. These gauge symmetries, expressed mathematically as gauge groups, are the building blocks in the formulation of a theoretical model known as the *Standard Model* (SM) which is used for understanding the contents and interaction properties of visible matter. The SM describes with unmatched precision, the possible types of interactions and their strengths, the fundamental particle contents and their properties which make up the entire visible matter. Despite this unprecedented success of the SM compared to most scientific models, the SM fails to describe DM which make up the largest portion of the matter in our universe.

There have been numerous experimental reports on the discovery of all the particles

predicted by the SM. On the nature of DM, results from theoretical models and numerical N-body simulations [2], support speculation that dark matter could be made up of particles which are neutral and stable i.e. particles which can remain stable enough for a long period of time comparable to the age of our universe, before they disintegrate. Such particles generally referred to as *dark matter candidate* particles could themselves be produced from the disintegration (decay) of not entirely stable or meta-stable particles with sufficiently long lifetimes on the length scale of a particle detector particles[3]. These meta-stable particles with sufficiently long lifetimes are called *Long-Lived* (LL) particles. LL particles can either be charged or neutral (i.e. in the context of the SM, carry no net charge). There is significant interest towards neutral DM particles, since DM does not interact with light. A good amount of effort is directed towards the search for dark matter particles produced from the decay of *neutral long-lived* particles[4]. Experimental techniques for detecting neutral particles are very limited and so previous methods for searching for DM particles are often being updated with few new methods entirely developed.

The search for dark matter particles covers a wide range of experiments, from deep space search experiments like the Hubble and James Webb Space Telescope experiments, the Alpha Magnetic Spectrometer detector on board the International Space Station of NASA, ground based particle detector experiments like the Super Cryogenic Dark Matter Search experiment which try to detect dark matter particles produced in cosmic rays, to collider experiments like the Large Hadron Collider (LHC) of the European National Laboratory for Nuclear Research in Geneva, Switzerland, where dark matter particles can be produced during particle collisions. The interest in collider experiments is base on theoretical model predictions that dark matter particles or particles which decay into dark matter particles can be produced in a collider like the LHC, provided there is sufficient center-of-mass energy. These models are extensions of the standard model to allow for the existence of new fundamental particles. The models are called *Beyond Standard Models* (BSM) and there are several of them. *Supersymmetry* is a BSM which extends the gauge symmetries to a much larger family of symmetries and allows for the doubling of the particles in the SM to include a wide variety of new fundamental particles which can be dark matter particles[3, 4]. A particular branch of supersymmetry models called Gauge Mediating Supersymmetry Breaking (GMSB) models, predict

the production of new, massive, meta-stable, neutral, weakly interacting and long-lived particles which can decay into a candidate dark matter particle and isolated energetic photons. The candidate dark matter particle is stable and also neutral and weakly interacting. It has a lifetime comparable to the age of the universe. Detecting photons from the decay of a supersymmetry neutral and weakly interacting long-lived particle will be an indication of new particles, as there are no neutral, weakly interacting and long-lived particles which decay into photons in the SM. Numerous previous experiments have searched for these photons. Often, the results from these experiments have been negative. Nevertheless, new experiments with new detection techniques and clever search methods depending on the manner of production and decay of these new particles are continuously being developed. We will refer to such new, massive, weakly interacting and neutral long-lived particles which decay into isolated photons and candidate dark matter particles as *Neutral Massive Long-Lived Particles* (NMLLP).

Our search analysis is motivated by the classic signature of a delayed photon from the decay of a NMLLP in GMSB models, produced in the LHC proton collider. The decay products of the NMLLP are detected using the multi-purpose Compact Muon Solenoid (CMS) particle detector. We consider the NMLLP to be the Next-To-Lightest Supersymmetric Particle (NLSP) called the *lightest neutralino* ( $\tilde{\chi}_1^0$ ). This lightest neutralino decays into a photon and the Lightest Supersymmetric Particle (LSP) called the gravitino ( $\tilde{G}$ ). The gravitino is neutral and weakly interacting with visible matter, and being the LSP makes it stable. These properties make the gravitino a good dark matter particle.. The neutralino decay can in general be instantaneous (prompt) or *delayed* depending on the choice of parameters in the neutralino decay model. In a subset of models called *R-Parity Conserving* (RPC) GMSB models, supersymmetry particles are pair produced either, directly during particle collisions, or from the cascade decay of higher massive supersymmetry particles produced also in particle collisions. As a result, in these models, the LSP is very stable and automatically a dark matter candidate particle while the NLSP (neutralino) is often long-lived and the photons are energetic, isolated and often delayed in their arrival time at a detector. These often delayed photons can be detected using the electromagnetic calorimeter (ECAL) of the

CMS detector. The ECAL has an excellent timing resolution better than a *nanosecond* (ns). In cases where the neutralino is produced from the cascade decay of higher massive particles, large transverse momentum ( $p_T$ ) spray of hadronic particles collectively called jets are also part of the neutralino production and decay event. Since the gravitino is weakly interacting with the detector material, it is undetected. The gravitino presence is inferred using *missing transverse momentum* which in combination with the transverse momenta of the jets and photons should conserve the total momentum of the event in the transverse plane of the detector. In the decay scenario of the neutralino where its lifetime is large, say above, 3 ns, the photon is delayed and its measured arrival time is large (many nanoseconds (ns)). This is because of the inherently long neutralino lifetime and the extra distance it has to travel inside the detector before it decays. Finding an event, with the combination of jets, missing transverse momentum and at least a delayed photon is a clear signal for new particles not known in the standard model (SM). The CMS detector is located in the LHC tunnel at one of the proton bunch crossing points also known as *Interaction Point* (IP). We measure the arrival time of the photon from the IP to the surface of the ECAL. Relying on the excellent timing and energy resolution of the ECAL, we can distinguish between high energy photons from the decay of a NMLLP from those produced by the SM which are often prompt and not delayed. To ensure this excellent timing resolution, the ECAL detector is continuously time calibrated throughout the entire LHC proton-proton collision year. We will describe in future chapters how the ECAL timing alignment is done to realize this excellent timing resolution. Observation of a delayed photon event at the LHC using ECAL timing measurements, will confirm the existence of NMLLPs and will help answer important questions in particle physics like: What is the source and nature of dark matter?, Is there any reason why known SM particles are classified into 3 generations and have very different masses as known? Why do we observe so much matter compared to anti-matter in our universe? Is there a single universe or multi-verses? Answers to these questions will provide a clear understanding and direction for future research in physics beyond the SM.

In this thesis, we have described our search for a NMLLP decaying to a photon using arrival time information of the photon to the ECAL and use this information to

distinguish between the signal from new long-lived particles and background from SM interactions. Our search analysis uses data recorded using the CMS detector produced from proton-proton ( $pp$ ) collisions at the Large Hadron Collider (LHC) with a center-of-mass energy  $\sqrt{S} = 8$  TeV. The contents of this thesis is arranged beginning with this introduction as chapter 1, followed by chapter 2, which gives a brief description of the SM, highlighting its strengths and weaknesses which motivates why we need to go beyond the SM in our efforts to understanding the universe. The study *supersymmetry* as our BSM physics model, paying particular attention to GMSB models which allows for the existence of NMLLP which can decay into a photon and a gravitino with jets in the associate event. In Chapter 3, we describe the LHC and CMS particle detector, dueling only on the sub-detectors which have been used in our search analysis. How timing measurements of a particle are made by the ECAL sub-detector is described in chapter 4. The reconstruction of a full event with its constituent particles is described in chapter 5 with the definition of quantities like jets and missing transverse energy ( $E_T^{\text{miss}}$ ) according the CMS standards is described. Anomalous signals called *spikes* observed in the ECAL is mentioned. Our search strategy is described in chapter 6 with details of which datasets and triggers we have used, what is trigger efficiency, our choice of search observable, event selection and background estimation techniques used. We describe the various systematic sources considered and their contribution to our search result is presented in this chapter. Chapter 7 presents the statistical and analysis methods used with clear meaning of  $p$ -values as used in our analysis. The cross section times branching ratio limits depending on the lifetime and mass of the production and decay of a NMLLP using the minimal *Gauge Mediating Supersymmetric Model*, with *Snowmass Signal Point 8* (SPS8) as our benchmark model is presented in chapter 8. The interpretation of our results in terms of exclusion regions reached by our analysis is also presented in this chapter. Chapter 9 covers the conclusion.

## Chapter 2

# Phenomenology of Long-Lived Particles

### 2.1 The Standard Model of Particle Physics

The Standard Model (SM) of particle physics provides a thorough and experimentally verified mathematical model description of the fundamental constituents of visible matter and its interactions (except gravity) in the universe. Predictions of particle properties and interactions by the SM agree with most of the available experimental data with unmatched precision.

Despite the numerous success of the SM, there are some theoretical and experimental inconsistencies with the SM such as the observation of Dark Matter (DM) in the universe which is indescribable by the SM, the observation of neutrino oscillation and neutrino masses unexplained by the SM and the absence of gravitational interactions in the SM. These shortcomings of the SM, promotes the believe that the SM is part of a more general model. A candidate mathematical model beyond the SM which provides possible explanations for the above observations is *supersymmetry*.

In the next sections, we briefly describe the major components of the SM, its strengths and limitations and also introduce supersymmetry as a leading candidate for models beyond the SM.

### 2.1.1 Main Components of the SM

Mass, charge, spin and lifetime can be used to identify and categorize fundamental particles of nature. Particles with the same charge, mass and spin but opposite charge are called *Anti-particles* while particles with equal amounts for positive and negative charge are said to be neutral. A interesting classification of particles and anti-particles is using their *spin* ( $s$ ). A particle's spin is an *internal quantum number* expressed as  $n\hbar$ , where  $n$  can be *integer* or *half-integer*. Half-integer spin ( $\frac{1}{2}, \frac{3}{2}, \dots \times \hbar$ ) particles obey a *Fermi-Dirac* distribution or statistics and are called *fermions*. Integer spin particles ( $0, 1, 2, \dots \times \hbar$ ) obey *Bose-Einstein* statistics and are called *Bosons*. No two identical fermions can occupy the same quantum state but any number of bosons can occupy a given quantum state.

Fermions are the fundamental building blocks of matter while bosons mediate interactions between fermions. No particle with spin,  $s = 0\hbar$ , had ever been experimentally observed until the 4th of July 2012 when the *Higgs* boson with spin,  $s = 0\hbar$ , was observed[7]. The Higgs boson is responsible for providing mass to both fermions and bosons. Its discovery completes the SM.

The particle spin set,  $S$ , shown in Equation 2.1.1, shows the spins of particles discovered and yet-to-be-discovered in the universe.

$$S = \left\{ s = \left( \dots 0, \frac{1}{2}, 1, \frac{3}{2}, 2 \dots \right) \cdot \hbar \right\}$$

Looking at the set  $S$ , our present and possibly future understanding of particles in the universe can be summarize as follows:

- $\mathbf{S = \frac{1}{2}\hbar}$  Particles which make up visible matter in the universe.
- $\mathbf{S = 1\hbar}$  Particles mediating gauge interactions.
- $\mathbf{S = 0\hbar}$  Particle responsible for giving mass to other particles.
- $\mathbf{S = 2\hbar}$  Yet-to-be-discovered particle mediating gravitational interactions.
- $\mathbf{S = \frac{3}{2}\hbar}$  Yet-to-be-discovered particle likely to make up **Dark Matter?**

It is interesting to note that the set particles with spins,  $s = \{0, \frac{1}{2}, 1\} \hbar$ , describes precisely only 4.6% of the entire matter in the universe through the SM. The SM is

a *relativistic quantum field theory* in which particles are represented as *quantum fields* and their dynamics and interaction with other particles is expressed using a mathematical functions called *Lagrangian density*,  $\mathcal{L}$ . The Lagrangian density is invariant under certain transformations or symmetries and carries the description of the dynamics of fermions, bosons and their interactions with the Higgs boson. Fermions and bosons obtain their mass by interacting with the Higgs boson through a process crucial to the SM called *Higgs Mechanism*. Our brief description of the SM, will be divided into the following sections:

- **Fermions:** All of visible matter is described using fermion fields.
- **Interactions:** Fermions interact either through electromagnetic, weak and strong interactions with vector bosons mediating the interactions. An interaction is the realization of some generic symmetry and associated with this symmetry is a conserved quantity.
- **Spontaneous Symmetry Breaking or Higgs Mechanism:** Fermions originally have no mass. They get their mass by interacting with the Higgs field through the *Higgs mechanism*. New states of matter or fermions can be formed through mixing with other states of matter or fermions.

## Fermions

The *Dirac* equation given by Equation 2.1 is part of the SM Lagrangian describing

$$\mathcal{L}(\bar{\psi}, \psi, G^\mu) = \bar{\psi} (i\gamma^\mu \mathcal{D}_\mu - m) \psi. \quad (2.1)$$

fermion dynamics with its electromagnetic interaction through the  $\mathcal{D}_\mu$  term. In the full SM Lagrangian, including the description of electromagnetic, weak and strong interactions, fermions participate in these interactions as pairs or *doublets* called a representation. According to the SM, fermions exists as either leptons ( $\ell$ ) or quarks ( $q$ ) and come in 3 *generations*. The SM provides no explanation for the existence of only 3 generations. Leptons can participate in electromagnetic and weak interactions but not in strong interactions while quarks can participate in both interactions and strong interactions. Leptons have integer charge while quarks have fractional charge. The 3

generations of quarks and leptons also known as *flavors* are arranged in a mass hierarchy with the third generation being the heaviest. The second and third generations are meta stable can disintegrate or *decay* into the first generation through weak interactions. A lepton pair consists of a particular lepton flavor and its corresponding neutral neutrino type. There is a corresponding neutrino for each lepton generation. For example, an **electron** ( $e$ ) and its corresponding electron **neutrino** ( $\nu_e$ ) make the first generation pair, ( $e, \nu_e$ ). Other lepton flavors include **muon** ( $\mu$ ) and **muon neutrino** ( $\nu_\mu$ ) pair ( $\mu, \nu_\mu$ ) and **tau** ( $\tau$ ) and **tau neutrino** ( $\nu_\tau$ ) pair ( $\tau, \nu_\tau$ ). In the SM, neutrinos are described as having no mass, however, numerous experiments have confirmed that neutrinos have a very tiny mass (order of electronvolts (eV)) and can oscillate from one generation into another over sufficiently large distances.

For quarks, a first generation pair of quarks consists of an “*up-type*” and a “*down-type*” quark. In addition to the electric charge, quarks also carry a *color* charge and as a result can equally participate in strong interactions. *Up-type* quarks like **up** ( $u$ ), **charm** ( $c$ ), **top** ( $t$ ) have charge of  $+\frac{2}{3}$  and *down-type* quarks such as **down** ( $d$ ), **strange** ( $s$ ), **bottom** ( $b$ ) have a charge of  $-\frac{1}{3}$ . Charges are expressed in units of elementary charge  $e$ . The quark include ( $u, d$ ) is the first generation and ( $c, s$ ) and ( $t, b$ ) are respectively, the second and third generations. Quarks do not exist as free particles in nature but are found bound forming composite particles like *pions* and *protons* collectively called *hadrons*. Hadrons consisting of a quark and antiquark (same mass and spin as a quark but different charge) bound together are called *mesons*, e.g. pions ( $\pi^0, \pi^\pm$ ), while those with at least 3 quarks bound together are called *baryons*, e.g. protons. The distributions of these quarks inside hadrons can be modeled using *parton distribution functions* (PDF) which depends on the fraction of momentum of the given hadron carried by each quark.

One can distinguish between “Left” from the “Right” handed quarks and leptons from the nature of their interaction with electroweak bosons.

Since most particles in the second and third generation are meta-stable, and do decay into the first generation particles, it is possible to describe all visible matter in our universe using only one generation of leptons, **electron** and the **electron neutrino** ( $e, \nu$ ) and one generation of quarks, **up-quark** and **down quark** ( $u, d$ ).

## Interactions

Interaction between fermions is mediated by vector *bosons* with spin,  $s = 1\hbar$ . The SM describes the electromagnetic, weak and strong force and their force mediators. The *electromagnetic force* whose force carrier is a massless vector boson; the *photon* ( $\gamma$ ), is described using the mathematical formulation called *Quantum Electrodynamics* (QED). It is responsible for the interaction of light with matter. The *weak force* has 3 massive vector bosons;  $W^\mp$ ,  $Z^0$ , as its force mediators and it is responsible for the decay of the second and third generation quarks into the first generation. The weak force was independently developed by Sidney Glashow, Abdus Salam and Steven Weinberg [8] in the 1960s unifying it with the electromagnetic force in a mathematical formulation called the *Electro-Weak Field Theory*. The 3 massive vector bosons were predicted in the late 1960s and were eventually discovered at CERN in 1983. Finally, the *strong force* described using the mathematical formulation of *Quantum Chromodynamics* (QCD) has a massless *gluons* (g) as its force mediators. The strong force like the weak force is a nuclear force, however, the same unification of the weak and electromagnetic forces is not observed with the strong force. It remains an open question whether at much higher energies, all 3 forces become unified behaving as a single force.

It is speculated that the gravity interaction not described by the SM, is mediated by a spin-2 particle called the *graviton* which is yet to be discovered.

The formulation of the SM, relies on the concept of *symmetry* and *conserved quantum numbers*. A symmetry is a transformation which leaves invariant the dynamics (Lagrangian density,  $\mathcal{L}$ ) describing a particle interaction. Every particle interaction is associated with a symmetry and a conserved quantity. The conserved quantity is called *conserved quantum number*. Belonging to the SM, are *gauge symmetries*, meaning the SM Lagrangian remains invariant under space-time dependent gauge transformations. The gauge symmetry of the SM is a combination of 3 different gauge symmetries;  $SU(3)_C$ ,  $SU(2)_L$  and  $U(1)_Y$ , each describing a particular particle interaction type. This combination is expressed as given in equation 2.2.

$$SU(3)_C \otimes SU(2)_L \otimes U(1)_Y \quad (2.2)$$

$SU(3)_C$  is the gauge symmetry associated with strong interactions and the conserved quantum number is the *color* ( $C$ ) charge allowing the gluon to interact with itself and with quarks. There are 8 (in the *octet* representation of the  $SU(3)$  gauge symmetry) colorless and massless gluons and three different color type quarks for each quark flavor. Anti-quarks carry anti-color charges. Leptons, like electrons, do not carry the color charge and as a result cannot participate in strong interactions.

$SU(2)_L \otimes U(1)_Y$  is the gauge transformation group with conserved quantum number, *isospin* ( $T_3$ ), necessary for the electroweak interaction. Corresponding to the  $SU(2) \otimes U(1)$  gauge group, there are 4 massless gauge bosons,  $W_\mu^{1,2,3}, B_\mu$ , which combine to form the physical electroweak bosons of charged  $W^\mp$  and neutral  $Z^0$  and  $\gamma$ . The  $W^\mp$  and  $Z^0$ , through the spontaneous breaking of the electro-weak symmetry, obtain their masses. These physical mass states is responsible for quarks to be able to transform from one generation to the other. These bosons couple using the “charge” of the weak interaction called *isospin*,  $T_3$ , and the *hypercharge*,  $Y$ , to matter fields. The  $W^\mp$  only interacts with **left-handed** fermions and **right-handed** anti-fermions. This leads to a phenomenon called *parity* violation. The electromagnetic charge,  $Q$ , is the result of a combination of the third component of the weak isospin,  $T_3$  and the hyper charge,  $Y$ , through the following relation:

$$Q = T_3 + \frac{Y}{2} \quad (2.3)$$

Left handed fermions have  $T_3 = \pm \frac{1}{2}$  and form representations known as isospin *doublets*, while, right-handed fermions have  $T_3 = 0$  and form isospin *singlets* in the SM . The particles in the SM together in their representations given by the gauge symmetry as *multiplets*(*doublets*, *triplets*, etc) and the corresponding conserved quantum numbers is presented in Table 2.1. The  $SU(2)_L \otimes U(1)_Y$  guage group is a combination of two symmetry groups with coupling strengths  $g$  and  $g'$  connected to the electric charge of each fermion as  $e = g \sin \theta_w = g' \cos \theta_w$ .

The angle,  $\theta_w$ , is the *Weinberg angle*,  $\sin^2 \theta_w \approx 0.231$  is not predicted by the SM but measured from experiments. Gauge bosons can rotate from their *weak* eigen states

to physically observed states using this angle.

$$W^\mp_\mu = \frac{W_\mu^1 \mp i W_\mu^2}{\sqrt{2}}, \quad \begin{pmatrix} A_\mu \\ Z_\mu \end{pmatrix} = \begin{pmatrix} \cos \theta_w & \sin \theta_w \\ -\sin \theta_w & \cos \theta_w \end{pmatrix} \begin{pmatrix} B_\mu \\ W_\mu^3 \end{pmatrix} \quad (2.4)$$

This angle,  $\theta_w$ , also allows for the transformation of a quark from one flavor into another through the  $W^\mp$  bosons. In the lepton sector, according to formulation of the SM, such flavor transformation could in principle be possible but does not lead to any possible observable effects as neutrinos are considered to be massless in the SM. On the other hand, recent neutrino experiments have proven otherwise, as mixing between different neutrino types have been observed, indicating that neutrinos are not massless as thought but rather do have mass. The transformation of quarks into different flavors is a typical interaction happening inside the core of our sun in the decay of neutrons to protons and similarly in a nuclear reactor. The complete transformation of all quark flavors is described by the *Cabibbo-Kobayashi-Maskawa* (CKM) 3 by 3 matrix whose elements are parameters only measured from experiments and not predicted by the SM.

Particle and Their Gauge Symmetry Representation

Particle Name(Symbol)	Spin	Multiplet	$SU(3)_C \otimes SU(2)_L \otimes U(1)_Y$
Quarks ( $Q$ )	$1/2$	$(\mathbf{u}_L, \mathbf{d}_L)$	$(\mathbf{3}, \mathbf{2}, \frac{1}{6})$
$\bar{\mathbf{u}}$	$1/2$	$\mathbf{u}_R^\dagger$	$(\bar{\mathbf{3}}, \mathbf{1}, -\frac{2}{3})$
$\bar{\mathbf{d}}$	$1/2$	$\mathbf{d}_R^\dagger$	$(\bar{\mathbf{3}}, \mathbf{1}, \frac{1}{3})$
( $\times 3$ families)			
Leptons ( $L$ )	$1/2$	$(\nu, \mathbf{e}_L)$	$(\mathbf{1}, \mathbf{2}, -\frac{1}{2})$
$\bar{\mathbf{e}}$	$1/2$	$\mathbf{e}_R^\dagger$	$(\bar{\mathbf{1}}, \mathbf{1}, 1)$
( $\times 3$ families)		$\nu_R^\dagger$	$(\bar{\mathbf{1}}, \mathbf{1}, 1)$
Higgs ( $\mathbf{H}_u$ )	$0$	$(\tilde{\mathbf{H}}^+_u, \tilde{\mathbf{H}}^0_u)$	$(\mathbf{1}, \mathbf{2}, +\frac{1}{2})$
Higgs ( $\mathbf{H}_d$ )	$0$	$(\tilde{\mathbf{H}}^+_d, \tilde{\mathbf{H}}^-_d)$	$(\mathbf{1}, \mathbf{2}, -\frac{1}{2})$
<b>Force Carriers</b>			
Gluons	$1$	$\mathbf{g}$	$(\mathbf{8}, \mathbf{1}, 0)$
<b>(Strong Force)</b>			
W bosons	$1$	$\mathbf{W}$	$(\mathbf{1}, \mathbf{3}, 0)$
B boson	$1$	$\mathbf{B}^0$	$(\mathbf{1}, \mathbf{1}, 0)$
<b>(Electro-Weak Force)</b>			

Table 2.1: SM particles and their gauge multiplets(representation) with quantum numbers. the numbers for example  $(\mathbf{3}, \mathbf{2}, \frac{1}{6})$  means (*triplet, doublet,  $Y = 1/6$* ) representations.

### 2.1.2 Spontaneous Symmetry Breaking

*Spontaneous symmetry breaking* is the spontaneous breaking of the gauge symmetry from a parent symmetry into an entirely, new sub-symmetry. In the SM, spontaneous symmetry is realized as represented by the expression in equation 2.5.

$$SU(3)_C \otimes SU(2)_L \otimes U(1)_Y \xrightarrow{SSB \text{ into}} SU(3)_C \otimes U(1)_{QED} \quad (2.5)$$

Early attempts prior to the 1960s to construct a gauge theory of weak interactions failed because the gauge bosons were massless while experimental evidence proved otherwise.

The Higgs (or Higgs-Brout-Englert) mechanism [10], is achieved by introducing a complex weak isospin *scalar doublet*,  $\phi$ , i.e spin  $s = 0\hbar$ . During this process, the  $SU(2)_L \otimes U(1)_Y$  symmetry is spontaneously broken into a  $U(1)$  symmetry which describes electromagnetic interaction. Figure 2.1 shows a picture of the potential of the spin-0 complex Higgs field. The minimum value of the potential,  $|\phi_0| = \sqrt{\frac{-\mu^2}{\lambda}} = \nu$ , based on the choice of the parameters  $\mu^2 < 0$  and  $\lambda > 0$ , is to spontaneously break the  $SU(2)_L \otimes U(1)_Y$  symmetry into  $U(1)$  symmetry. During spontaneous symmetry breaking, both matter and gauge bosons, except the photon  $\gamma$ ), obtain masses. The process is referred to as *Higgs-Brout-Englert mechanism* or *Higgs mechanism*.

Quarks and leptons obtain their masses through their interaction with the Higgs field. A fermion's mass,  $m_f$ , is proportional to the strength of its interaction (Yukawa coupling  $\lambda_f$ ) with the Higgs field. Electro-weak interaction mediating gauge bosons,  $Z^0$  and  $W^\pm$  obtain their mass  $m_Z$  and  $m_{W^\pm}$ , respectively, by engulfing or “*eating*” the available massless components (*Nambu-Goldstone bosons*) of the complex Higgs doublet. From the four scalar fields(complex Higgs doublet), only a physically massive *Higgs boson* remains.

$$m_f = \lambda_f \frac{\nu}{\sqrt{2}}, \quad \frac{m_{W^\pm}}{m_Z} = \frac{\frac{1}{2}\nu g}{\frac{1}{2}\nu \sqrt{g^2 + g'^2}} = \cos \theta_w \quad (2.6)$$

The search for the Higgs boson was one of the purpose for building the large hadron collider at CERN. The discovery of the Higgs candidate scalar boson through its decay into two photons,  $H \rightarrow \gamma\gamma$ , and a pair of Z bosons,  $H \rightarrow ZZ$ , was presented to the public on July 04, 2012. Its measured mass was  $m_H = 125 \pm 0.21 \text{ GeV}/c^2$ .

It is important to note that there is no fundamental reason given by the SM why there should be only one type of the Higgs field to which all fermions couple to obtain their masses nor any prediction from the SM for the choice of parameters. There are other models such as supersymmetry, which allows for the possibility of more than one Higgs field. In Figure 2.2, we show a complete summary of particles and their interactions as described by the SM.

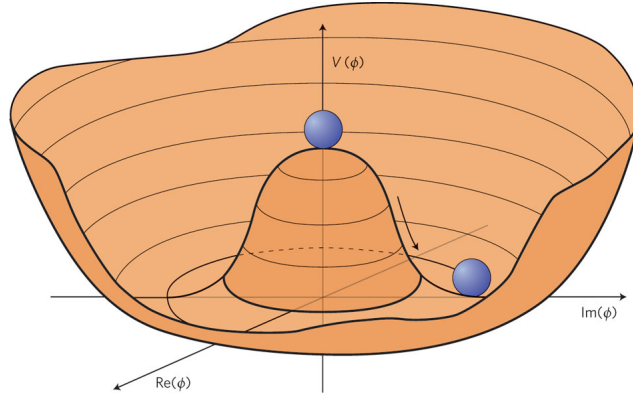


Figure 2.1: Higgs boson “Mexican hat” potential,  $V(\phi^*\phi) = \mu^2(\phi^*\phi) + \lambda(\phi^*\phi)^2$ , which leads to spontaneous symmetry breaking with choice of parameters  $\mu^2 < 0$ ,  $\lambda > 0$ .

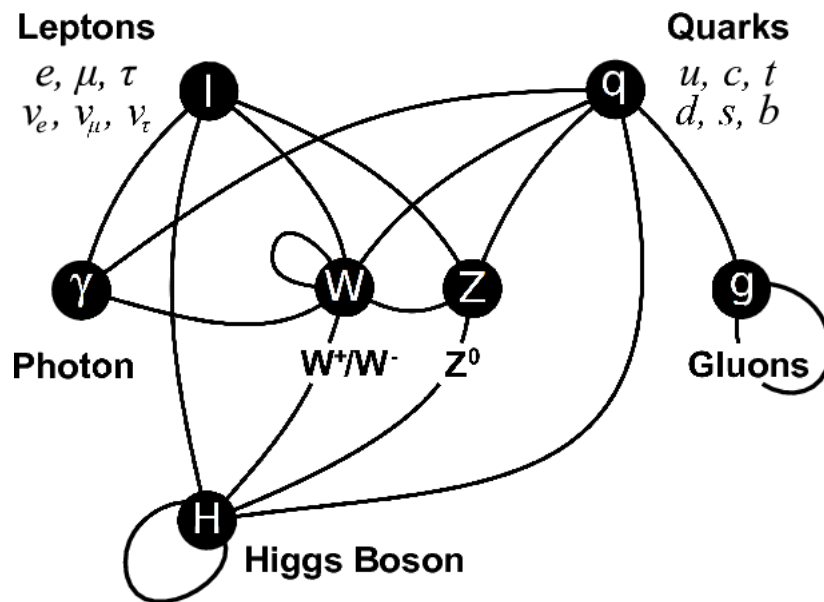


Figure 2.2: SM particles and their interactions with vector bosons as mediators.

### 2.1.3 Limitations of the Standard Model

Although numerous experiments support the SM in its description of particle properties with unmatched precision, there are many unanswered questions by the SM. We provide a summary below of those of our interest.

- **General Formalism**

Many important parameters like particle masses, Weinberg angle, the CKM matrix elements, for example, cannot not be derived from the SM. These are measured from experiments. Why only 3 generations of particles? Why the specific doublet representation of fields in the SM? These are questions to which the SM provides no answer.

- **Cosmological**

Why is there so much matter than anti-matter in the universe? *Cosmic Microwave Background* (CMB) and the *Wilkinson Microwave Anisotropy Probe* (WMAP) experimental results indicate the presence of excess matter which does not interact with light called *Dark Matter* (DM) and *Dark Energy* (DE). DE is responsible for the increase energy density causing rapid accelerating expansion of the universe. The nature of DM and DE and such observations cannot be explained using the current SM.

- **Theory**

SM description of nature does not include gravitational interactions. Observation of SM coupling constants varying with energy begs the question of whether at some higher energy scale, all the weak, strong and electromagnetic coupling constants behave as one i.e unified as a single coupling constant. If possible, at what energy scale does this force unification occur?

- **Mass Hierarchy or Naturalness**

Particle masses ranges from neutrino masses, a few eV to the top particle's mass of  $173 \text{ GeV}/c^2$ . The SM does not explain this mass hierarchy. To some physicist, the energy gap between the electro-weak symmetry breaking energy scale ( $\approx 246 \text{ GeV}$ ) and the Planck energy scale (reduced Planck mass,  $M_p = 10^{18} \text{ GeV}$ ) seems unnatural.

## 2.2 Beyond Standard Model Physics

The Higgs boson mass from SM predictions include additional corrections,  $\delta m^2$ , to the higgs mass through its couplings with fermions such as the diagram shown in Figure 2.3(a). These additional corrections are given as shown in equation 2.7.

$$\delta m_f^2 = \frac{1}{16\pi^2} |\lambda_f|^2 \left( -2\Lambda^2 + 6m_f^2 \ln \left( \frac{\Lambda}{m_f} \right) + \dots \right) \quad (2.7)$$

Where  $\lambda_f$  is the Higgs to fermion coupling,  $\lambda_f H \bar{f} f$  and  $\Lambda$  is an arbitrarily large energy scale (can be of order  $10^{18}$  GeV) called the *cut-off* energy scale. As a result of this cut-off scale being very large, these corrections can also be very large. However, large corrections to the Higgs boson's mass are not observed in experimental measurements of the Higgs boson's mass which is  $125$  GeV/ $c^2$ . The SM provides no explanation for why these corrections are not observed.

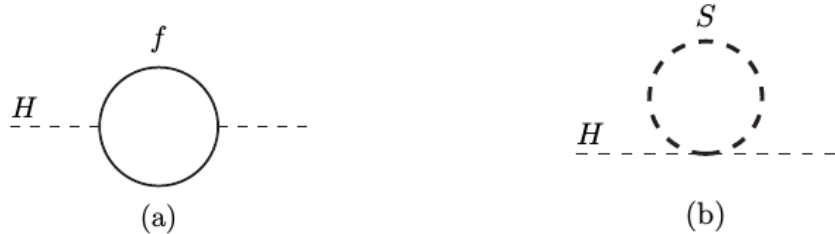


Figure 2.3: Higgs mass contributions from its coupling to fermions (a) and scalar (b) fields.

Models beyond the SM like *supersymmetry*, provide a plausible explanation as to why these corrections are not observed in experiments. The explanations is that, there are in addition to the higgs boson being the only scalar particle in the SM, new scalar particles, yet to be observed, which can also couple to the higgs field as shown in the diagram in figure 2.3(b). These scalar coupling contribution, given in equation 2.8 is of the opposite sign and as a result cancel the fermion contributions to the Higgs boson's mass. This is the explanation why the corrections to the Higg Boson's mass cannot be observed experimentally.

$$\delta m_S^2 = \frac{1}{16\pi^2} |\lambda_S|^2 \left( \Lambda^2 - 2m_S^2 \ln \left( \frac{\Lambda}{m_S} \right) + \dots \right) \quad (2.8)$$

This problem is known as the *Hierarchy problem* and is explained using supersymmetry. This cancellation is provided at all levels of the Higgs boson interaction and for whatever energy scale the cut-off value may be. Supersymmetry does not only provide an explanation to the Hierarchy problem, but also provide a good framework for the unification of fundamental forces. In addition, supersymmetry also predicts the existence of additional particles to the SM which are non interacting with ordinary matter and having very long lifetime making these particles exceptional candidates as dark matter particles. These properties motivates the study of supersymmetry as an interesting extension of the SM for understanding physics beyond the SM (BSM).

### 2.2.1 Supersymmetry

Supersymmetry is a relativistic Quantum Field Theory (QFT), relating space-time symmetries (rotation and translation) and gauge symmetries ( $SU(3)_C \otimes SU(2)_L \otimes U(1)_Y$ ). During the early period, very little was understood about supersymmetry. Progress in understanding began with the *Haag-Lopuszanski-Sohnius* theorem [11] in 1975. This led to the introduction of supersymmetry generators called *Lie-superalgebra* generators,  $Q_i$ ,  $i = 1, \dots, N$ , where  $N$  is the number of supersymmetry generators, which anti-commute with the group and space-time generators. The consequence is that fermions can be transformed into bosons and vice-versa. This boson-to-fermion and fermion-to-boson transformation is expressing using Equations 2.9.

$$Q|\text{Fermion}\rangle = |\text{Boson}\rangle, \quad Q|\text{Boson}\rangle = |\text{Fermion}\rangle \quad (2.9)$$

Thus, in supersymmetry, particles in a given state have the *same* mass but differ in their spin by half  $\hbar$  and in every irreducible representation of supersymmetry, like the chiral representation, there is an equal number of fermionic and bosonic degrees of freedom. Every particle has a supersymmetric partner with the same mass belonging to the same state representation or *supermultiplet*.

These supermultiplets are either *Chiral*, *Vector* or *Gravity* multiplets. The minimal supersymmetric extension of SM uses Chiral and Vector supermultiplets shown in Table 2.2.

<b>Supermultiplets</b>	<b>Spin in SM,</b>	<b>Spin in Supersymmetry</b>
<i>Chiral</i>	0	$\frac{1}{2}$
<i>Chiral</i>	$\frac{1}{2}$	0
<i>Vector</i>	1	$\frac{1}{2}$
<i>Gravity</i>	2	$\frac{3}{2}$

Table 2.2: Supermultiplets and particle spin in SM and Supersymmetry.

Models in supersymmetry are developed using *superfields*,  $\Phi$ . A given superfield consists of ordinary scalar real or complex fields ( $\phi$ ), a Lorentz vector field ( $A_\mu$ ) and Left-handed or Right-Handed Weyl(2 degrees of freedom) spinor fields ( $\psi$ ). *Chiral* and *Vector* superfields are used in constructing the minimal supersymmetric standard model. The simplest supersymmetric model is an extension of the SM to include supersymmetric particles with the same mass as their standard model partners. It is called the *Minimal Supersymmetric Standard Model* because it only involves the use of a single supersymmetry generator.

### 2.2.2 Minimal Supersymmetric Standard Model

In the Minimal Supersymmetric Standard Model (MSSM), the number of fundamental particles is increased. The full particle content in MSSM with this extension from SM is shown in Table 2.3 and 2.4.

The nomenclature of supersymmetric particles is derived from their SM counterparts by adding an “*s*” in front of the SM particles names. For example, a *selectron* is the supersymmetric partner of the electron, *squarks* are the supersymmetric partners of SM quarks. There are exceptions to this nomenclature which we will mentioned later. Both supersymmetry particles and their SM partners should have the equal masses, however, there have been no experimental evidence for such supersymmetric particles having the same mass as SM particles. Therefore, Supersymmetry is definitely not an exact symmetry in nature and must be spontaneously broken.

Particle Names	Symbol	spin 0	spin 1/2	$SU(3)_C \otimes SU(2)_L \otimes U(1)_Y$
squarks, quarks ( $\times 3$ families)	$Q$	$(\tilde{u}_L, \tilde{d}_L)$	$(u_L, d_L)$	$(\mathbf{3}, \mathbf{2}, \frac{1}{6})$
	$\bar{u}$	$\tilde{u}_R^*$	$u_R^\dagger$	$(\bar{\mathbf{3}}, \mathbf{1}, -\frac{2}{3})$
	$\bar{d}$	$\tilde{d}_R^*$	$d_R^\dagger$	$(\bar{\mathbf{3}}, \mathbf{1}, \frac{1}{3})$
sleptons, leptons ( $\times 3$ families)	$L$	$(\tilde{\nu}, \tilde{e}_L)$	$(\nu, e_L)$	$(\mathbf{1}, \mathbf{2}, -\frac{1}{2})$
	$\bar{e}$	$\tilde{e}_R^*$	$e_R^\dagger$	$(\bar{\mathbf{1}}, \mathbf{1}, 1)$
higgsinos, Higgs	$H_u$	$(H_u^+, H_u^\circ)$	$(\tilde{H}_u^+, \tilde{H}_u^\circ)$	$(\mathbf{1}, \mathbf{2}, +\frac{1}{2})$
	$H_d$	$(H_d^\circ, H_d^-)$	$(\tilde{H}_d^\circ, \tilde{H}_d^-)$	$(\mathbf{1}, \mathbf{2}, -\frac{1}{2})$

Table 2.3: Chiral supermultiplets and representation in Minimal Supersymmetric SM (MSSM). Super symmetric particles (sparticles) have a  $\sim$  on them. Spin -0 fields are complex scalars while spin-1/2 fields are left-handed two component Weyl fermions.

Particle Names	spin 1/2	spin 1	$SU(3)_C \otimes SU(2)_L \otimes U(1)_Y$
gluino, gluon	$\tilde{g}$	$g$	$(\mathbf{8}, \mathbf{1}, 0)$
winos, $W$ bosons	$\tilde{W}^\pm, \tilde{W}^\circ$	$W^\pm, W^\circ$	$(\mathbf{1}, \mathbf{3}, 0)$
bino, $B$ boson	$\tilde{B}^\circ$	$B^\circ$	$(\mathbf{1}, \mathbf{1}, 0)$

Table 2.4: Gauge supermultiplets and representations in Minimal Supersymmetric SM (MSSM). Super symmetric particles (sparticles) have a  $\sim$  on them.

Similar to the Higgs mechanism, supersymmetry breaking is also spontaneous and breaking supersymmetry can happen in many different ways. One of the ways in which supersymmetry is spontaneously broken is by gauge interactions. Supersymmetric models formulated using gauge interactions as the way to spontaneously break supersymmetry is called *Gauge Mediated Supersymmetry Breaking* (GMSB) models. GMSB models are interesting because they allow for only 5 fundamental parameters and still provide candidate dark matter particles. Supersymmetry breaking is realized in each model through a *superpotential* and the breaking defines the phenomenology and particle mass spectrum. In MSSM, particles interact with the Higgs bosons through a superpotential to

obtain their masses . This superpotential can be expressed as given in Equation 2.10.

$$W_{\text{mssm}} = \bar{u} \mathbf{y_u} Q H_u - \bar{d} \mathbf{y_d} Q H_d - \bar{e} \mathbf{y_e} L H_d - \mu H_d H_u \quad (2.10)$$

The objects  $H_u$ ,  $H_d$ ,  $Q$ ,  $L$ ,  $\bar{u}$ ,  $\bar{d}$ ,  $\bar{e}$  are chiral superfields of the chiral supermultiplets given in Table 2.3 above. The dimensionless couplings  $\mathbf{y_u}, \mathbf{y_d}$ , and  $\mathbf{y_e}$  are  $3 \times 3$  matrices of the Yukawa couplings. Rather than a single Higgs *doublet* which is assumed in the SM, supersymmetry breaking requires two Higgs doublets:  $H_u$  and  $H_d$ . The two Higgs give mass to **up-type** and **down-type** quarks, respectively, and to leptons, The superpartners of these Higgses are fermions and those of the gauge bosons called *gauginos* mix to produce new neutral and charged fermions called *Neutralinos* and *Charginos*, respectively. In order for GMSB models predictions of the proton lifetime to agree with experimental measurements of the proton lifetime being  $> 10^{32}$  years, a matter symmetry relating the quarks to leptons through the *baryon* ( $B$ ) and *lepton* numbers ( $L$ ), a symmetry called *R-Parity* is introduced. R-parity is defined as,  $R_P = (-1)^{3(B-L)+2S}$ , where  $S$  is the particle's spin. SM particles like quarks have an *even* R-parity,  $R_P = 1$ , while supersymmetric particles like squarks have odd parity  $R_P = -1$ . The phenomenological consequence of R-parity is that, first, in the decay of supersymmetric particles, the lightest SUSY particle (LSP) have odd parity  $R_P = -1$  and is considered to be absolutely stable. Second, every supersymmetric particle produced and is not the LSP, will eventually decay into the LSP or an odd number of LSPs. Third, supersymmetric particles can only be produced in pairs in a collider experiment. If, in addition to being stable, the LSP is neutral and interacts only very weakly with ordinary matter, then this makes it a good candidate for non-baryonic dark matter as required by cosmology, [3]-[5].

*R-parity Conserving* (RPC) models with the LSP stable are different from models without the conservation of R-parity. These R-parity non-conserving models are called *R-parity Violating* (RPV) models. In RPV models the LSP is unstable and decays to SM particles. A simplified version of GMSB models studied in this thesis is the *Snowmass Point and Slopes* (SPS8),[6], models whose phenomenological predictions are within the reach of the large hadron collider. It is possible to produce supersymmetric particles with mass of about a few TeV at the large hadron collider (LHC).

Figure 2.4 presents the mass spectrum for supersymmetric particle as predicted by the SPS8 model. The mass difference is determine by the supersymmetry breaking energy scale represented by  $\Lambda$ .

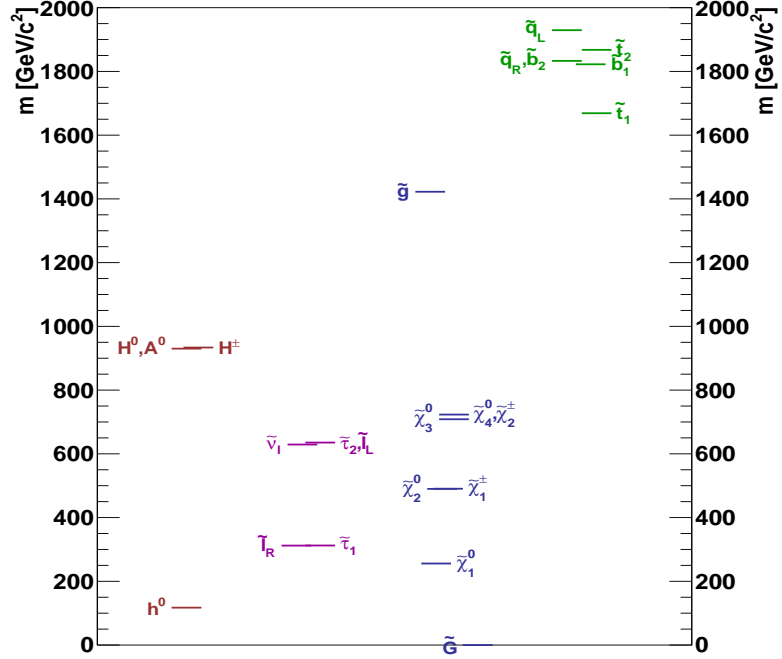


Figure 2.4: Supersymmetry particle mass spectra in the SPS8 or minimal GMSB (mGMSB) model.

In summary, MSSM predicts the existence of new particles whose spin ( $S$ ) differ from their SM counterparts by half-integer. Bosons (fermions) in the SM have superpartners which are fermions (bosons). The superpartners of SM fermions are scalars called *sfermions* ( $\tilde{l}$ ), sneutrinos ( $\tilde{\nu}$ ) and squarks ( $\tilde{q}$ ) while *gluinos* ( $\tilde{g}$ ) are the superpartners of the massless gauge bosons of strong interaction, gluons. The scalar Higgs (2 needed) bosons and the vector gauge bosons of Electro-Weak interaction have fermionic superpartners called *higgsinos*, *Winos* and *Binos*. These can mix to form a pair of mass eigenstates called *charginos* ( $\tilde{\chi}_j^\pm, j = 1, 2$ ), i.e.,  $\tilde{\chi}_{1,2}^\pm$  are mixtures of  $\tilde{W}^+, \tilde{W}^-, \tilde{H}^+, \tilde{H}^-$  and a quartet of mass eigenstates called *neutralinos* ( $\tilde{\chi}_i^0, i = 1, \dots, 4$ ), i.e.,  $\tilde{\chi}_{1-4}^0$  are mixtures of  $\tilde{B}^\circ, \tilde{W}^\circ, \tilde{h}^\circ, \tilde{H}^\circ$ .

## 2.3 Gauge Mediated Supersymmetry Breaking Models

GMSB models have 5 main parameters:

$$\{\Lambda, M_{\text{mess}}, N_5, \tan(\beta), sgn(\mu), C_{\text{grav}}\} \quad (2.11)$$

where  $\Lambda$  is the effective supersymmetry breaking scale,  $M_{\text{mess}}$  is the mass of the messenger particle involved in mediating supersymmetry breaking to the MSSM energy scale,  $N_5$  is the number of messenger particles. The other parameters,  $\tan \beta$  and  $sgn(\mu)$  are related to the two Higgs bosons necessary for supersymmetry breaking with  $\tan \beta$  being the ratio of the vacuum expectations values for both Higgs bosons. The sign of the Higgs potential is defined by  $sgn(\mu)$ . In these models, the gravitino can become very light with its mass bounded only by cosmological observations and as such is identified as the Least Stable supersymmetric particle (LSP). The mass of the gravitino is expressed in terms of the parameter  $C_{\text{grav}}$  according to equation 2.12.

$$m_{\tilde{G}} = C_{\text{grav}} \cdot \frac{\Lambda M_{\text{mess}}}{\sqrt{3} M_{pl}} \quad (2.12)$$

where  $M_{Pl} = 1.3 \times 10^{19}$  GeV/c<sup>2</sup>.  $C_{\text{grav}}$  is a scaling parameter, which determines the lifetime of the Next-to-Lightest-Supersymmetric Particle (NLSP) since the neutralino decay rate to the gravitino will depend on the mass difference between the neutralino and gravitino.

### 2.3.1 Phenomenology

Light gravitinos with unique gravitino-scalar-chiral fermion and gravitino-gaugino-gauge boson interactions shown in Figure 2.5 in GMSB models allow for the gravitino mass to be as low as a few eV and up to an upper bounded for them to provide the right amount of dark matter observed in the early universe. In addition to this, being neutral and stable makes them an excellent candidate particle for dark matter.

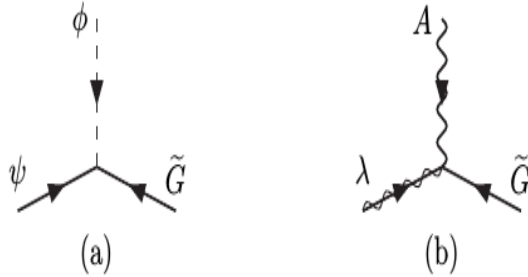


Figure 2.5: Feynman diagrams of gravitino/golstino,  $\tilde{G}$ , gaugino and scalar interactions with superpartner pairs  $(\psi, \phi)$  scalar (a) and  $(\lambda, A)$  gaugino (b) decay to gravitino.

The decay of the NLSP to the gravitino is always accompanied by the SM partner of the NLSP, in order to conserve R-parity. If the particle,  $\tilde{p}$ , is the NLSP, its decay to gravitino and its SM particle,  $p$ , is given as  $\tilde{p} \rightarrow p + \tilde{G}$ . In the SPS8 benchmark model, the choice of parameters is as follows:  $\mathbf{M}_{\text{mess}} = 2\Lambda$ ,  $\tan(\beta) = 15$ ,  $\mathbf{N}_5 = 1$ . Only  $\Lambda$  and  $C_{\text{grav}}$  are allowed to vary, [6]. The gravitino ( $\tilde{G}$ ), is the LSP. The NLSP,  $\tilde{p}$ , is the lightest neutralino ( $\tilde{\chi}_1^0$ ). There are four types of neutralinos which are a mixture of the supersymmetric particles Bino ( $\tilde{B}^\circ$ ), Wino ( $\tilde{W}^\circ$ ), higgsino ( $\tilde{H}_u^\circ, \tilde{H}_d^\circ$ ), depending on the choice of parameters  $\Lambda$ ,  $\tan \beta$ , and  $\text{sgn}(\mu)$ . The particle  $p$  could be a photon ( $\gamma$ ), Z boson ( $Z$ ) (or  $Z'$ ) and a higgs boson ( $h$ ). This thesis, for experimental convenience, will focus on the parameter space for which the particle  $p$  is a photon ( $\gamma$ ) and  $C_{\text{grav}} > 1$ . This ensures that the lifetime of the NLSP is long enough but still its decay happens within the detector volume and the resulting photon is delayed or non-prompt on length scales of size of the detector. The decay rate for a NLSP to its SM partner and a gravitino can be approximated using only the mass of the NLSP and the effective supersymmetry breaking scale,  $\mathbf{F} = C_{\text{grav}} \cdot \Lambda \cdot \mathbf{M}_{\text{mess}}$  giving in equation 2.13.

$$\Gamma(N\tilde{LSP} \rightarrow \gamma \tilde{G}) \approx \frac{m_{NLSP}^5}{\mathbf{F}^4} \quad (2.13)$$

This approximation is almost the same for the non-minimal GMSB models except that additional parameters are present showing explicit dependence of the neutralino life time on its states as a mixture of other supersymmetric particles.

### 2.3.2 Long-Lived Particles in GMSB Models

Measuring a particle's life time or distance traveled before it decays can be a useful method to uncover new fundamental interactions. As the lifetime is related to the decay rate which is determined by the particles interactions and available energy space.

#### Production of Supersymmetric Particles at Hadron Colliders

The production of a particle in a particle collider is a probabilistic process. This probability is expressed as a measurable quantity called *cross section*. For example, the cross section of producing a particle in proton-proton collider such as the LHC, is the probability that the proton beams will collide and interact in a certain way to produce that particle. Although this cross section ( $\sigma$ ) is measured in units of area as *barns* ( $1b = 10^{-24} \text{ cm}^2$ ), usually it has very little relation to the physical interpretation of area as used in everyday life. It is rather a technical term for counting the number of the particle produced when these proton beams collide. The cross section of producing the particle depends on the available energy of the proton beams compared to the mass of the particle, the type of interaction during collision which in turn depends on the coupling constants, and the flux of the proton beams. The rate or number per unit time of the particle produced at a specific particle collider is given as a product of its cross section times the instantaneous luminosity ( $\mathcal{L}$ ). The instantaneous luminosity is the number of incident particles per unit area per unit time. The typical cross section of producing a supersymmetry particle at the LHC is of the order of  $1 \text{ pb} = 10^{-12} \times 10^{-24} \text{ cm}^2$  or at times  $1 \text{ fb} = 10^{-15} \times 10^{-24} \text{ cm}^2$  for extremely rare SUSY processes. While that for a standard model process like the production of the Z or  $W^\pm$  bosons is of the order of a few  $nb = 10^{-9} \times 10^{-24} \text{ cm}^2$ . This means there are more SM processes than supersymmetry process and so the search for supersymmetric particles in the LHC is very challenging.

The rate of production of a supersymmetric particle at the LHC depends on the mass of supersymmetric particle. The masses of supersymmetric particles are much higher than those of SM particles and as a result, the cross section for producing supersymmetry particles at a hadron collider is much smaller compared to that for SM particles. The cross section of a given supersymmetric process happening at the particle collider

can be computed and compared with experimental measurements. Using diagrammatic representations called *Feynmann* diagrams of the process happening, the cross section is derived from the Feynmann diagrams as the computed probability of the process. Supersymmetry processes which leads to the production and decay of neutralino ( $\tilde{\chi}_1^0$ ) at the LHC can involve electro-weak and strong interactions. The production of supersymmetry particles in strong interactions have larger cross sections compared to electro-weak processes because of the strong coupling in strong interaction processes. Many interaction processes in the LHC are strong interactions as the LHC is a proton-proton collider. We show in Figure 2.6 a diagram showing the variation of the supersymmetry production cross section against the mass of the supersymmetric particle. From this figure, it is clear that the production of supersymmetric particle at the LHC through strong interactions like  $pp \rightarrow \tilde{g}\tilde{g}$ ,  $\tilde{q}\tilde{q}$  is higher than through electro-weak interactions like  $pp \rightarrow \tilde{\chi}^\pm\tilde{\chi}^\mp$ ,  $\tilde{\chi}^0\tilde{\chi}^\pm$ .

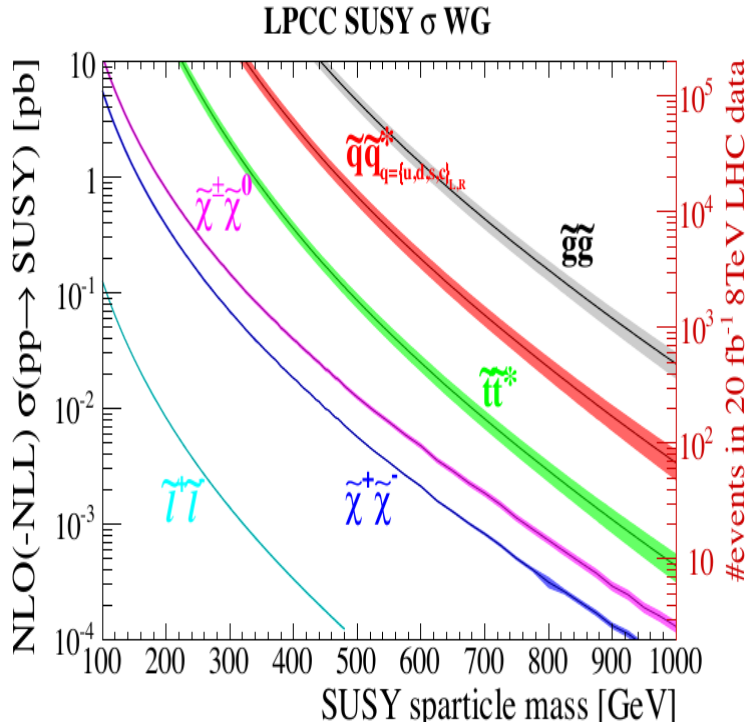


Figure 2.6: Supersymmetry production cross-section against sparticle mass for different modes of supersymmetry production at a proton-proton collider.  $pp \rightarrow \tilde{g}\tilde{g}$ ,  $\tilde{q}\tilde{q}$  processes have the dominant production cross section.

We will concentrate on the production of neutralinos from processes like  $pp \rightarrow \tilde{g}\tilde{g}$ ,  $\tilde{q}\tilde{q}$ , as these processes have a higher production cross section at the LHC. We mentioned earlier that a probable manner in which neutralinos can be produced is from the production and subsequent decay of higher massive supersymmetric particles. Some of these higher massive supersymmetric particles include squarks ( $\tilde{q}$ ), excited squarks ( $\tilde{q}^*$ ) and gluinos ( $\tilde{g}$ ). In this scenario, the neutralino is produced *indirectly* or as we say from the *cascade decay* of higher massive supersymmetric particles. The Feynmann diagram for these production processes,  $pp \rightarrow \tilde{g}\tilde{g}$ ,  $\tilde{q}\tilde{q}^*$ , are given in figure 2.7. Squarks and gluinos do not directly decay into gravitinos but through neutralinos and eventually to gravitinos because their coupling to the gravitinos is not possible. The reason for this is that, in GMSB models, there are no gravitino-gluino-gauge boson or gravitino-squark-gauge boson couplings but rather gravitino-gaugino-gauge boson or gravitino-scalar-chiral fermion couplings.

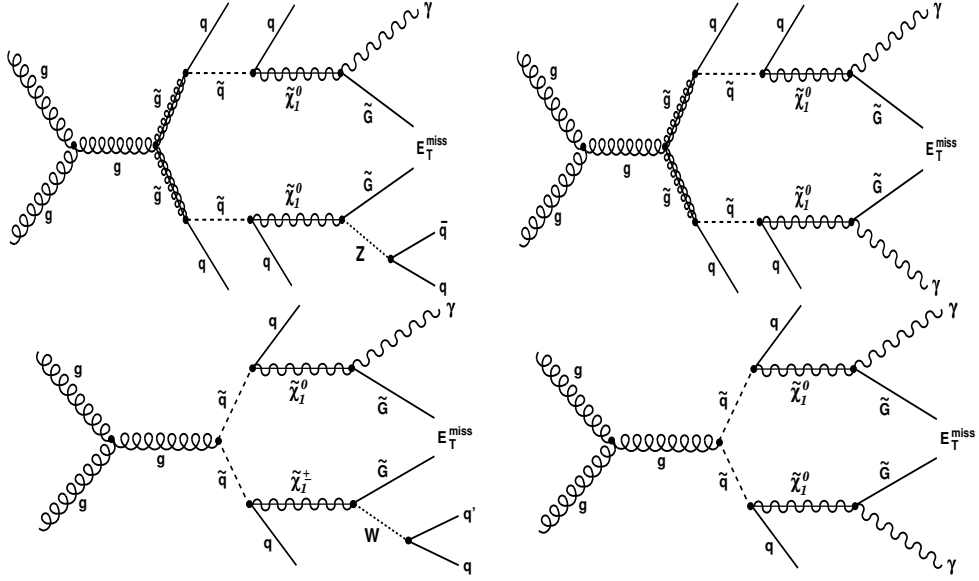


Figure 2.7: Feynmann diagrams for neutralino production from the cascade decay of a produced gluino (top) and squark (bottom). The final event has a single (left diagrams) or double photons (right diagrams) neutralino decay at LHC.

### Particle Decay Rate

When a particle is produced, say particle **A**, its coupling to other particles, say particles **B<sub>1</sub>** … **B<sub>n</sub>**, where  $n$  is total number of particles particle, allows for it to decay into these other particles. In addition to the coupling, if the mass of particle **A** is greater than the total sum of mass of particles **B<sub>1</sub>** … **B<sub>n</sub>**, i.e  $m_{\mathbf{A}} > m_{\mathbf{B}_1} + \dots + m_{\mathbf{B}_n}$ , then we say, particle **A** *decays* to particles **B<sub>1</sub>** … **B<sub>n</sub>**. Particle for which no such channel for decay is possible are termed *stable*. Our current understanding is that only the electron (e) and the proton (p) are stable( although there are theories which predict the proton to decay after  $10^{34}$  years and also theories where stable heavy or light particles will explain the nature of Dark Matter. This time through which a particle lived before it decays is called its *lifetime*. Particle decays in which the particle decays instantly as soon as they are produced are called *prompt* decays while particle decays with observable lifetime are *non-prompt* decays. Non-prompt decays might range from factors of a seconds i.e. *nanoseconds* ( $1 \text{ ns} = 10^{-9} \text{ s}$ ) to minutes. In particle decay, strong *couplings* and large *mass difference* between the parent and the daughter particle(s) leads to faster

the decay. The process of obtaining the decay rate during experiments is expressed mathematically as;  $N(t) = N(0)e^{-t/\tau}$ , where both  $N(t)$  and  $N(0)$  are the number of the particles present at time  $t$  and at the beginning,  $t = 0$ .  $\tau$  is the particle's *lifetime*. The rate at which a particle decays is its *decay width* ( $\Gamma$ ). The decay width relies on the availability of daughter particle(s) the parent particle can couple to and the mass(es) of the daughter particle(s) must be less than the mass of the parent particle. Thus, a given particle, **A** will preferentially decay to particles **C<sub>1</sub>** … **C<sub>n</sub>** with which it has stronger couplings and its mass is much larger than their masses. This preferential decay into a specific set of particles or channel brings about terms like *Branching Ratio* (BR). The BR is related to the total decay width through  $BR = \Gamma/\Gamma_{\text{Total}}$ , where,  $\Gamma_{\text{Total}}$  is the particle's total decay width and  $\Gamma$  is its decay width to a preferential channel. For example, the  $\tilde{\chi}_1^0$  does not only decay to  $\gamma$  but also to  $Z$  bosons, *Higgs*,  $e^+e^-$  and the  $\tilde{G}$ . However, its decay to a  $\gamma$  and  $\tilde{G}$  is the dominant mode of decay. With the BR for single photon decay of the  $\tilde{\chi}_1^0$  to a  $\gamma + \tilde{G}$  about 83 to 94%. We observed that 97 to 99% of all our simulated signal events contain at least a single photon. The decay width is related to lifetime,  $\tau$ , as the inverse of the lifetime. This relationship is expressed as given in Equation 2.14.

$$\tau = \frac{\hbar}{\Gamma} \quad (2.14)$$

$\tau$  is the particle's lifetime in a frame where the particle is not moving. It is convenient to express lifetime in units of lengths rather than time. The lifetime in units of lengths e.g. meters (m), is  $c\tau$ , where  $c$  is the speed of light in vacuum.  $c\tau$  is also called the *proper decay length* just as the lifetime,  $\tau$ , is also called the *proper lifetime*. Since most particles have mass and travel with velocity  $\vec{v}$  not equal to  $c$ , this distance travel considering  $|\vec{v}| \neq c$  is fully expressed using equation 2.15.

$$\vec{L} = \vec{\beta}\gamma c\tau \quad (2.15)$$

where  $\vec{\beta} = \frac{\vec{v}}{c}$ ,  $\vec{v}$  is the particle's traveling velocity and  $\gamma = \frac{1}{\sqrt{1 - \frac{v^2}{c^2}}}$  is a factor relating the motion when it is not moving (rest frame) to a frame where it is moving. Equation 2.15 can also be expressed in as  $\vec{L} = \frac{\vec{p}}{m}c\tau$ , in terms of the particle's momentum  $p$  and mass,  $m$ . A particle with a large mass,  $m$ , produced with a small momentum, will travel slow covering some distance before it decays. Since decay rate,  $\Gamma$ , depends on

the coupling, particle decaying through electromagnetic, weak and strong interactions have very different decay rates. Particles decaying through strong interactions have the largest decay rate and equally shortest lifetime of about  $10^{-17}$  to  $10^{-25}$  seconds. Electromagnetic particle decays have lifetime which can vary from  $10^{-12}$  seconds to about  $10^{-9}$  seconds and weak interactions have lifetimes that can vary from *nanoseconds* to several minutes. Particle lifetime may also vary from a few femtoseconds ( $1 \text{ fs} = 10^{-15} \text{ s}$ ) to the age of the universe or equivalently its measured distance traveled can vary from a few  $\mu\text{m}$  to billions of km [12, 13]. The term *long-lived* particles refers to particles which live long enough to travel a distance comparable to the detector size. This distance traveled might range from a few  $\mu\text{m}$  to meters.

### Neutralino as Long-Lived Neutral Particle

The neutralino being the next-to-lightest-supersymmetry particle (NLSP), can decay into a photon ( $\gamma$ ), Higgssino ( $\tilde{H}^0$ ), Z boson and gravitino ( $\tilde{G}$ ) [14, 15]. The probability for a neutralino ( $\tilde{\chi}_1^0$ ), produced with energy  $E_{\tilde{\chi}_1^0}$  and mass  $m_{\tilde{\chi}_1^0}$  to travel a distance  $x$  before decaying to a photon and gravitino in the laboratory frame can be expressed as  $\mathcal{P}(x) = 1 - \exp\left(-\frac{x}{L}\right)$ , where the distance traveled in a particle detector by the neutralino is given by Equation 2.16.

$$L = \left( c\tau_{\tilde{\chi}_1^0} \right) \cdot (\beta\gamma)_{\tilde{\chi}_1^0} \quad (2.16)$$

From Equation 2.16, it is clear that this distance depends on two main factors. The boost factor,  $(\beta\gamma)_{\tilde{\chi}_1^0} = \frac{|\vec{p}_{\tilde{\chi}_1^0}|}{m_{\tilde{\chi}_1^0}} = \sqrt{\left(\frac{E_{\tilde{\chi}_1^0}}{m_{\tilde{\chi}_1^0}}\right)^2 - 1}$ , which indicates how fast the neutralino is traveling before it decays. For slow moving neutralino,  $(\beta\gamma)_{\tilde{\chi}_1^0} \ll 1$ .

This means that the momentum ( $p_{\tilde{\chi}_1^0}$ ) of the neutralino during production from gluino or squarks decays must be much smaller than the its mass,  $m_{\tilde{\chi}_1^0}$ . Neutralinos, produced, with their mass and momentum satisfying the slow condition,  $p_{\tilde{\chi}_1^0}/m_{\tilde{\chi}_1^0} \ll 1$ , are definitely good candidates for detectable long-lived neutralinos. The other factor is the inherent long lifetime,  $c\tau_{\tilde{\chi}_1^0}$ , of the neutralino. Neutralinos with  $c\tau_{\tilde{\chi}_1^0} > 1$  are long-lived and would make good candidates for detectable long-lived neutralinos. This

inherent neutralino lifetime can be expressed as given in equation 2.17.

$$c\tau_{\tilde{\chi}_1^0} \approx \left( \frac{m_{\tilde{\chi}_1^0}}{\text{GeV}} \right)^{-5} \left( \frac{\sqrt{\mathbf{F}}}{\text{TeV}} \right)^4 \quad (2.17)$$

$$c\tau_{\tilde{\chi}_1^0} \approx C_{grav}^2 \left( \frac{m_{\tilde{\chi}_1^0}}{\text{GeV}} \right)^{-5} \left( \frac{\sqrt{\Lambda \cdot \mathbf{M}_{\text{mess}}}}{\text{TeV}} \right)^4 \quad (2.18)$$

It is important to note that by changing the supersymmetry breaking scale,  $\mathbf{F}$ , the lifetime of the neutralino also changes. In the SPS8 model, the parameter  $C_{grav}$  is used to adjust the inherent lifetime of the neutralino. Thus, we re-write the neutralino lifetime as given in equation 2.18. This equation is used to simulate physics events with the production and decay of neutralino in CMS detector using Monte Carlo (MC) simulations. The supersymmetry breaking scale,  $\Lambda$ , determines the mass of gluino ( $\tilde{g}$ ), squarks ( $\tilde{q}$ ) which decay to the neutralino. Therefore the neutralino momentum,  $p_{\tilde{\chi}_1^0}$  is determined by the masses of gluino and squarks. If the gluino or squark decays to the neutralino in association with a many gluons and quarks seen in the detector as *jets*, then the neutralino momentum is small with the ratio  $p_{\tilde{\chi}_1^0}/m_{\tilde{\chi}_1^0} \ll 1$ , this means the neutralino is slow and therefore long-lived. However, if the gluino or squark is decays with less number of jets, then the neutralino momentum is not so small and the neutralino is not very long-lived. It is worth noting that kinematic properties of the neutralino like momentum, arrival time at the CMS ECAL and the number of associated jets can be influenced by the gluino or squark decay properties. The gluino or squark is produced during proton-proton ( $pp$ ) collisions at the LHC and the data recorded by the CMS detector is analyzed to search for events with neutralino decay.

## 2.4 Previous Search Experiments

The have been previously other search experiments for neutral long-live particles decaying to photons. Obviously, negative findings from these experiments led to possible search exclusion regions in terms of the lifetime, mass and cross section of the existence of supersymmetry particles in different supersymmetry models. Results from experiments(DO, CDF, CMS and ATLAS) [16, 17, 18, 19, 20] of the search for Neutralino NLSP decaying to photon and gravitino interpreted using the SPS8 benchmark

model is shown in 2.8. These results show that within the SPS8 model, neutralinos with mass  $m_{\tilde{\chi}_1^0} \leq 245$  GeV and proper decay length  $c\tau_{\tilde{\chi}_1^0} \leq 6000$  mm have not been found at hadron colliders. The diagram on the left of figure 2.8 are exclusion results in the neutralino mass or supersymmetry breaking scale  $\Lambda$  on the horizontal axis and the neutralino lifetime,  $c\tau_{\tilde{\chi}_1^0}$  on the vertical axis from the 7 TeV search analysis by the ATLAS experiment while the diagram on the right is that for CMS experiment. The colored regions on the plots shows the parameter space where these searches have been performed and the findings were negative.

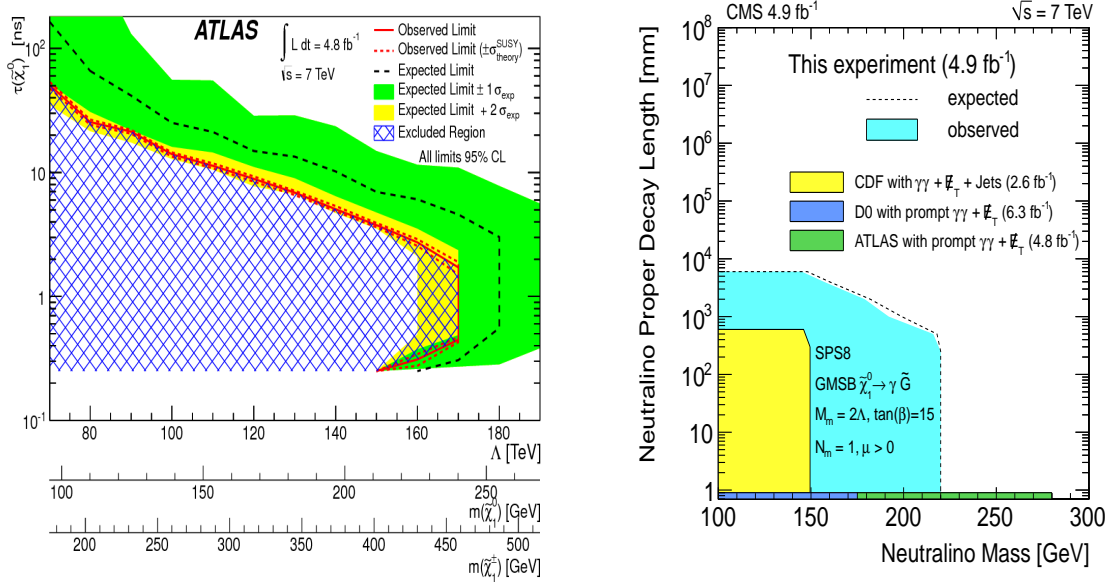


Figure 2.8: Neutralino lifetime and mass upper limit from ATLAS(left) and CMS(right) 7 TeV analysis with non-pointing photons and MET.

# Chapter 3

## Hadron Collider and Detector

This section describes the particle collider and detector. The first section describes the particle accelerator which is the Large Hadron Collider (LHC) and the next section describes the Compact Muon Solenoid (CMS) detector with emphasis to those sections directly relevant to this analysis. A detailed description of the LHC and CMS detector is found in [21] and [22].

### 3.1 Large Hadron Collider

#### 3.1.1 Overview

The LHC is a proton-proton and heavy ion collider designed to achieve a center of mass  $\sqrt{S}$  energy of 14 TeV. It is hosted by the European Organisation for Nuclear Research (CERN). Unlike linear colliders, the LHC is a circular collider with nearly 27 km in circumference located at the border between France and Switzerland. It is designed to smash protons and ions against each other controlled by powerful magnets at four main points. The Compact Muon Solenoid (CMS) is one of the multi-purpose particle detectors at each collision point. Fig. 3.1 shows the LHC and the different stages before particle collision.

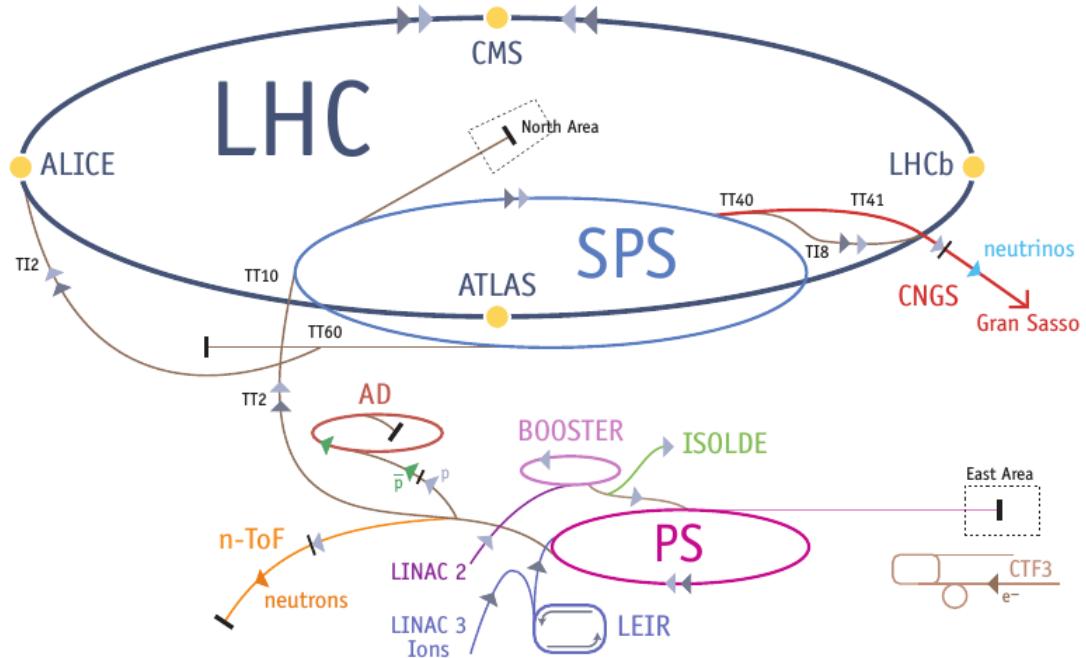


Figure 3.1: Schematic diagram showing the full Large hadron Collider.

### 3.1.2 Colliding Energy

Hydrogen ions also known as protons from hydrogen gass where the orbiting electron has been striped away is inserted into a linear accelerator called *Linac 2*. Using electromagnetic fields in Radio Frequency (RF) cavities, these protons are accelerated to an energy of 50 MeV creating a stream of particles called *particle beams* arranged in packets known as *bunches*. Protons from the Linac2 are injected into the circular synchrotron Booster (PSB). The circular synchrotron accelerator ensures that the protons pass many times through a cavity with their energy slowly increasing each time to reach the design energy. The PSB accelerates the protons up to 1.4 GeV and inject them into the Proton Synchrotron (PS) which increases their energy to 25 GeV. These protons traveling at 99.93% the speed of light are sent to the Super Proton Synchrotron (SPS) and accelerated to an energy of 450 GeV. They are finally transferred into the LHC ring(accelerating in a clockwise and anti-clockwise direction) and accelerated for about 20 minutes to their nominal energy of 7 TeV. By now the protons are traveling with the

speed of 99.9999% the speed of light. Powerful bending magnets are used to keep the beams traveling in the circular LHC ring. The advantage of circular particle colliders over fix target is that, the energy available to make new particles called the *center of mass* (COM) energy, denoted as  $\sqrt{S}$  is simply the sum of the energy of the two beams i.e.  $\sqrt{S} = E_{\text{beam1}} + E_{\text{beam2}}$  compared to  $\sqrt{E_{\text{beam}}}$  for fix target experiments. For the LHC, each beam is designed to have energy of 7 TeV making  $\sqrt{S} = 14$  TeV. In circular colliders, synchrotron radiation (is inversely proportional to the mass of the charge particle to the fourth power) by an accelerating charge particle contributing to loss its energy. This would require a continuous addition of energy after each turn to maintain the beam energy to a stable value. However, since the proton's mass is about 0.938 GeV, and are to be accelerated to about 7 TeV, this loss of energy is not very significant unlike for electrons whose mass is about 0.000511 GeV and the energy loss is more. Thus protons are preferred to electrons for a circular collider. Then again, the debris of particles produced when electrons collide is much less compared to that of protons making analysis in a hadron collider very challenging.

### 3.1.3 Luminosity

In colliding beams experiments, the center of mass energy available for the production of new effects is very important. However, the number of useful interactions producing effects (events) is equally important, especially in cases where the probability (also known as cross section,  $\sigma$ ) of producing rare events is very small. The quantity which measures the ability of a particle accelerator to produce the events from the required number of interactions is called *luminosity*. The luminosity is also the proportionality factor between the number of events per second and the cross section. Luminosity ( $\mathcal{L}$ ) is therefore a measure of the number of collisions that can be produced in a collider per squared area per second. The cross section is calculated from theory while the luminosity depends on factors ranging from the flux i.e. number of particles per second of the beams, the beam sizes at collision, and the frequency of collision. For physics experiments, the integrated luminosity which is total luminosity over a given period of time usually a year gives the amount of data that has been recorded by a given detector.

Using the luminosity ( $\mathcal{L}$ ) and the cross section ( $\sigma_p$ ) of a given process, we can calculate event rate ( $\mathcal{R}$ ) or the number of events per second produced in proton collisions

by the given interaction process. By calculating the event rate, we are measuring a given cross section ( $\sigma_p$ ) through  $(\sigma_p = \frac{\mathcal{R}}{\mathcal{L}}$  in order to prove or disprove theories which make prediction on  $\sigma_p$ .

$$\mathcal{R} = \mathcal{L} \cdot \sigma_p \quad (3.1)$$

In CMS we have a “recorded” and “delivered” luminosity. Delivered luminosity refers to the luminosity delivered by LHC to CMS and one would expect this to be equal to the amount recorded. However, there are instances where the CMS detector is unable to take data either because the data acquisition chain (DAC) or one of the CMS sub-detectors is temporarily down and also trigger dead time. Figure 3.2 shows the total integrated luminosity delivered by LHC and recorded using the CMS detector during the 8 TeV proton-proton collision by the LHC.

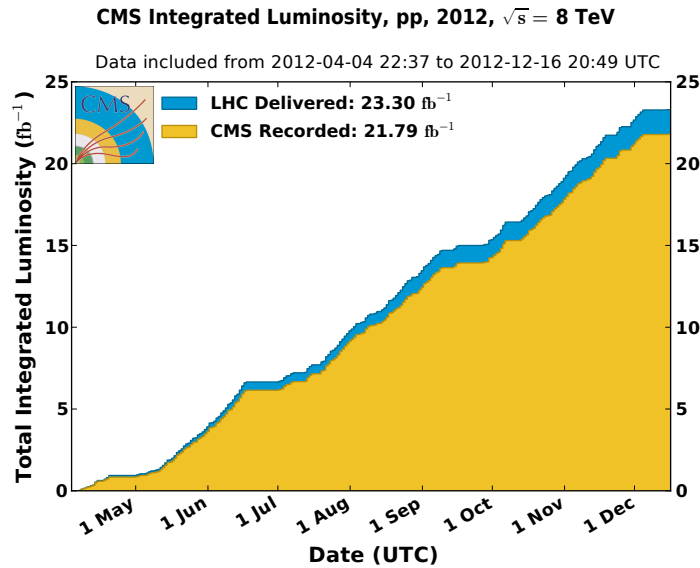


Figure 3.2: Cumulative luminosity versus day delivered to (blue), and recorded by CMS (orange) during stable beams and for p-p collisions at 8 TeV center-of-mass energy in 2012.

### 3.1.4 LHC Bunch Structure

Each LHC proton bunch is placed inside an RF buckets during beam filling. The filling scheme is such that not all RF buckets have proton bunches. Those empty buckets or beam gaps are necessary to avoid parasitic collision near IP and to make room for beam dump and beam halos known as beam cleaning. The separation in time between two

buckets/bunches filled or unfilled is approximately 2.5 ns. There are about  $10^{11}$  protons per bunch during filling and acceleration. However, during filling and eventual bunch splitting at PS, it is possible that some empty buckets are filled with a much smaller proton population compared to the main bunch. These buckets with few protons can be either trailing the main bunch by  $\Delta t = 2.5, 5.0, 7.5, \dots$  ns, or leading the main bunch by  $\Delta t = -2.5, -5.0, -7.5, \dots$  ns. If these less populated bunches are 2.5 to 3.0 ns spaced in time from each other, they are referred to as *satellite* bunches and if 5.0 ns, they are referred to as *ghost* bunches. Figure 3.3 shows ghost and satellite bunches and a main proton bunch.

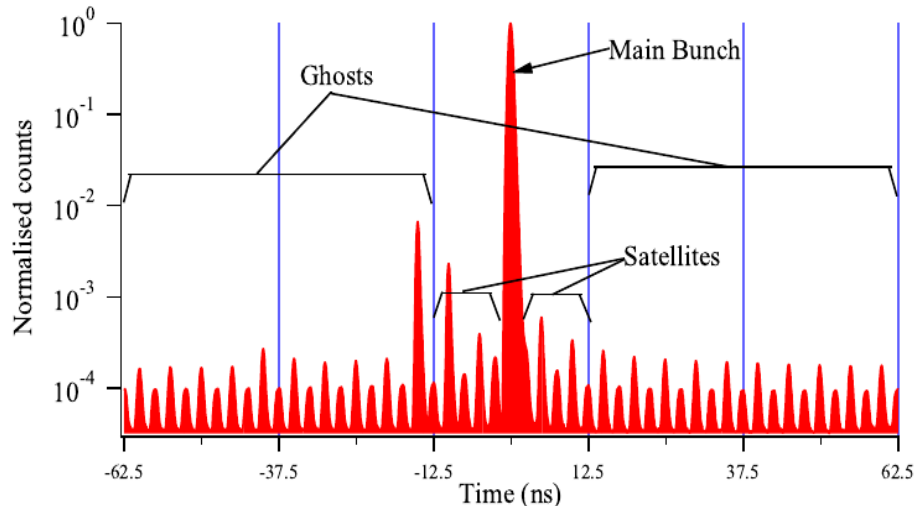


Figure 3.3: Longitudinal Profile taken with Longitudinal Density Monitor (LDM) detector showing definition of Ghost/Satellite bunches with respect to main bunches.

The presence of ghost/satellite bunches increases the uncertainty in LHC luminosity measurements and can also generate proton-proton interactions near but not at the collision region. Effects on ghost/satellite bunches on instantaneous luminosity measurements have been studied using CMS, ATLAS and ALICE detectors. Their results showing clear observation of physics events produced from ghost and satellite bunch collisions is shown in figure 3.4. CMS uses energy deposits in the endcap calorimeters to observe time space which is consistent with the expectation from ghost/satellite bunches while in ATLAS uses the Longitudinal Density Monitor (LDM) detector to study ghost/satellite bunches.

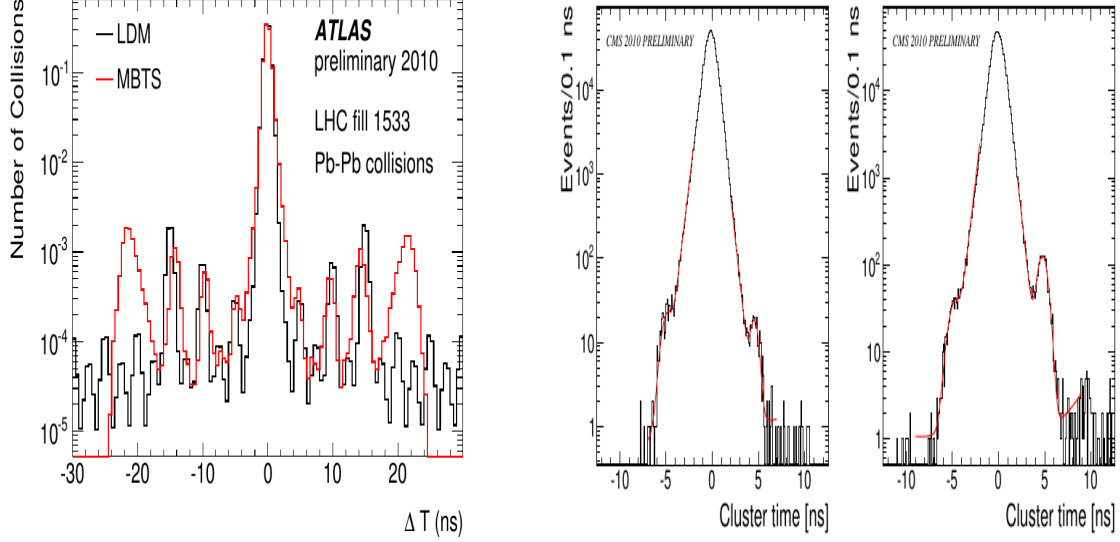


Figure 3.4: (left) Arrival time distribution(red) of ATLAS MBTS for LHC fill 1533 during 2010 Pb-Pb run and LDM profile(black) for Beam2(same for Beam1).  
 (Right) Timing of Clusters in the CMS endcap calorimeters for fill 1089:Left: EEP detector(left side of IP  $z > 0$ ) Right: EEM detector( right side of IP,  $z < 0$ ). Plots from ATLAS [30] and CMS, [31]

Table 3.1 gives a summary of the LHC design conditions compared to the conditions used during the LHC RUN 1 operation.

LHC Operation Parameters 2010-2013

Parameter	2010 value	2011 Value	2012/13 Value	Design Value
Beam energy[TeV]	3.5	3.5	4.0	7
$\beta^*$ in IP 5[m]	3.5	1.0	0.6	0.55
Bunch spacing [ns]	150	75/50	50	25
Number of bunches	368	1380	1380	2808
Protons/bunch	$1.2 \times 10^{11}$	$1.45 \times 10^{11}$	$1.7 \times 10^{11}$	$1.15 \times 10^{11}$
Normalised emittance[mm.rad]	$\approx 2.0$	$\approx 2.4$	$\approx 2.5$	3.75
Peak luminosity[ $cm^{-2}s^{-1}$ ]	$2.1 \times 10^{32}$	$3.7 \times 10^{33}$	$3.7 \times 10^{33}$	$1 \times 10^{34}$
Evts/bunch crossing	4	17	37	19
Stored Beam energy(MJ)	$\approx 28$	$\approx 110$	$\approx 140$	$\approx 362$
Int. Luminosity by CMS[ $pb^{-1}$ ]				-
Circumference[km]	26.659	26.659	26.659	26.659
Dipole Magnet B[T]	8.33	8.33	8.33	8.33

Table 3.1: LHC operation parameter conditions during RUN 1, 2010-2013

## 3.2 Compact Muon Solenoid

### 3.2.1 Overview

The Compact Muon Detector (CMS) is a modern particle detector design for many different particle detection capability. It is one of the general purpose detectors located at one of the proton-proton collision points along the 27 km LHC ring. Its main feature is the presence of a superconducting solenoid of 6 m internal diameter providing a field of 3.8 T for measuring a charge particle's momentum as the particle bends under the influence of this field traveling in the detector. This magnetic field encloses an entirely silicon pixel and strip tracker detector used for vertex finding and for detecting and reconstructing the tracks of charged particles, a lead-tungstate scintillating-crystals electromagnetic calorimeter (ECAL) and a brass-scintillating sampling hadron calorimeter (HCAL). Very long lived particles like muons are measured in gas-ionization detectors embedded in the flux-return iron-yoke located at the outermost section of the detector. It has a simple cylindrical structure consisting of barrel and endcap detectors and an extensive forward calorimetry and detectors to provide a near  $4\pi$  solid angle coverage assuring good hermetic particle detection. The CMS apparatus has an overall length of 21.6 m, a diameter of 14.6 m, and weighs 12,500 tons. Figure 3.5 shows the CMS detector indicating the different sub-detectors and their material design type. We provide a performance summary and material type of each sub-detector in Table 3.2 of the CMS detector. The CMS uses a coordinate system with the origin coinciding with the center of the detector where proton-proton or nominal collision occurs. This point is commonly referred to as the *interaction point* (IP). The direction of  $x$ ,  $y$ , and  $z$ -axes are as shown in figure 3.6. However, for particle identification, CMS uses a more convenient coordinate system based on the polar coordinates. In this polar coordinate system, the azimuthal angle,  $\phi$ , is measured in the  $x - y$  plane, where  $\phi = 0$ , is the  $x$ -axis and  $\phi = \pi/2$ , the  $y$ -axis. The radial distance in this plane is denoted  $R$  and the polar angle  $\theta$  measured from the  $z$ -axis is related to *pseudo-rapidity*,  $\eta$ , through the relation;  $\eta = -\ln \tan(\frac{\theta}{2})$ . The coordinate system  $(\eta, \phi)$  and its radial distance  $R$  identifies a point in the cylindrical volume of the CMS detector. In the coming sections, we describe the geometry, material characteristics and functionality of the CMS subdetectors used in our analysis.

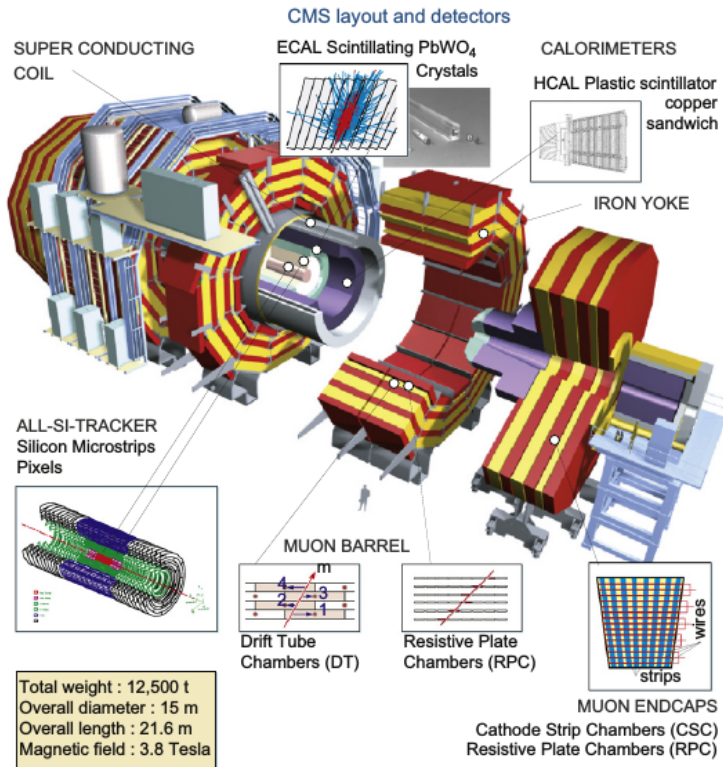


Figure 3.5: CMS Detector showing the different subdetectors and their material.

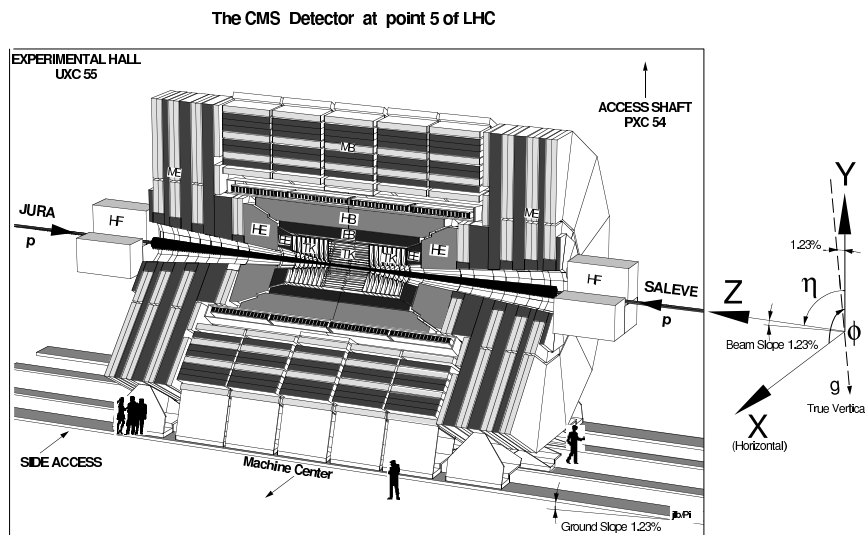


Figure 3.6: CMS detector schematic view with definition of  $x - y - z$  coordinates.

### CMS Detector and Resolution

Subdetector	Quantity	Resolution	Uses
Tracker	Momentum[GeV/c]	$\sigma_T/p_T \approx 1.5 \times 10^{-4} p_T + 0.005$	Silicon Pixels and Strips
ECAL	Energy[GeV]	$\sigma/E \approx 3\%/E + 0.003$	PbWO <sub>4</sub> Crystals
ECAL	Time[ns]	$\sigma(\Delta t) = \frac{N}{A_{eff}/\sigma_n} \oplus \sqrt{2}\bar{C}$	PbWO <sub>4</sub> Crystals
HCAL	Energy[GeV]	$\sigma/E \approx 100\%/E + 0.05$	Brass + Scintillator
Muon Chambers	Momentum[GeV/c]	$\sigma_T/p_T \approx 1\% \quad 50 \text{ GeV to } 10\% \quad 1 \text{ TeV}$	inner tracker + Muon Systems
Magnetic field	B-field strength[T]	3.8 T + 2 T	Solenoid + Return Yoke
Triggers	On/Off-line	Levels	L1(On-line) +HLT(Off-line)(L2+L3)

Table 3.2: CMS detector material, [22], and resolution(Time resolution:  $N \approx 35$  ns,  $\bar{C} \approx 0.070$  ns [39])

#### 3.2.2 Calorimeter

A CMS calorimeter absorbs a good fraction of energy of an incident particle and produces a signal with an amplitude proportional to the energy absorbed. This absorption is through the cascade production of secondary particles with energy of the incident particle directly proportional to the number of secondary particles produced. There are two types of calorimeters choices used in the CMS detector; the *Electromagnetic calorimeter* (ECAL); for absorbing the energy of electromagnetic particles such as photons and electrons and a *Hadronic calorimeter* (HCAL) made of more than one type of material for stopping and absorbing the energy of hadrons such as kaons and pions through strong interactions. The combined calorimeter detectors of CMS covers a region in  $|\eta| < 5$  making it nearly hermetic for good missing energy measurements. The ECAL

and HCAL are arranged in a nested fashion shown in figure 3.7 so that electromagnetic particles can be distinguished from hadronic particles by comparing the depth of the particle shower penetration in both calorimeters.

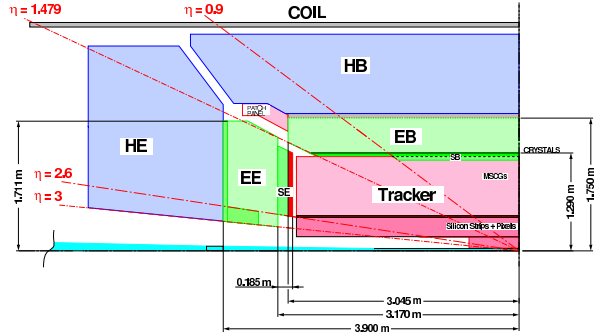


Figure 3.7: Schematic diagram of CMS calorimetry system with HCAL enclosing ECAL in the Barrel and Endcap regions.

### Electromagnetic Calorimeter

The electromagnetic calorimeter (ECAL) detects photons and electrons. High energy photons and electrons are detected through their interaction with the lead tungstate ( $\text{PbWO}_4$ ) crystals. During this interaction which happens either through electromagnetic showering or electron-positron pair production (*bremsstrahlung*), the incoming photon or electron deposit practically almost all of its energy. There are 75848 crystals in total mounted in a cylindrical geometry, with a barrel (EB) and an endcap (EE) structure. The choice of  $\text{PbWO}_4$  crystals as calorimetry material by CMS for operation in the LHC environment is because of its a high density ( $8.28 \text{ g/cm}^3$ ), short radiation length ( $X_0=0.89 \text{ cm}$ ) and a small Molière radius (22 cm). In a high radiation dose and fast timing (25 ns proton bunch spacing) environment like the LHC,  $\text{PbWO}_4$  crystals is preferred to other crystal materials for its high radiation resistance and a scintillation decay time which is comparable to the LHC bunch crossing interval of 25 ns and about 80% of the light is emitted in 25 ns. The probability of an electromagnetic object with high energy to interact either through *Bremsstrahlung* or *pair production* with the material in ECAL is proportional to the nuclear charge,  $Z$ , of the material.  $\text{PbWO}_4$  is a high  $Z$  material and this makes it once more the preferred material choice for electromagnetic calorimetry by CMS. The small Molière radius ensures that on average about

95 % of the electromagnetic shower energy is contained within a crystal crystal volume of about 9 crystals. This reduces the transverse spread of the electromagnetic cascade from multiple scattering of electrons and helps improve on the estimation of the transverse position of impact of an incident particle. It also provides a fine granularity for measuring the particle's energy by providing fewer overlap of particle signals. Its dense nature also allows for the electromagnetic shower to develop early and therefore likely to be fully contained within a compact device like CMS.

The EB section of the ECAL covers a pseudo-rapidity of  $|\eta| < 1.479$ . It has 61,200 crystals providing a granularity of 360 degree fold in  $\phi$  and  $(2 \times 85)$ -fold in  $\eta$ . The crystals are mounted in a quasi-projective geometry so that their axes make an angle of 3% with respect to a line vector from the nominal interaction vertex in  $\eta$  and  $\phi$  directions. This avoids cracks aligned with a particle's trajectory. A crystal in EB is approximately  $0.0174 \times 0.0174$  in  $\eta - \phi$  or  $22 \times 22 \text{ mm}^2$  at its front face and  $26 \times 26 \text{ mm}^2$  at its rear face. Each crystal is 230 mm long corresponding to about  $25.8 X_0$  radiation lengths. The crystal's radial distance measuring from the center of the face of the crystal to the beam line is 1.29 m. A number of crystals are placed in a thin-walled alveolar structure made with aluminum forming a *submodule*. Each submodule is arranged into 4 modules of different types according to their  $\eta$  position. There are about 400 to 500 crystals in each module and these 4 combined make one *supermodule* containing 1700 crystals. To reduce crystal reflective lost, the aluminum surface is coated to avoid oxidation leading to coloration. On the rear end of each EB crystal, two *Avalanche Photodiodes* (APD) is glued to collect the scintillating light from the crystals converting light into charge current which is further collected by the read-out electronics.

The endcap sector covers a pseudo-rapidity region of  $1.479 < |\eta| < 3.0$  with a Preshower (ES) detector made of silicon strip sensors interleaved with lead placed immediately in front of it. The purpose of the preshower is to identify photons from the decay of neutral pion,  $\pi^0 \rightarrow \gamma\gamma$  and also to help separate photons producing electrons through pair production from photons not producing electrons before their arrival at the EE. The endcap located on the  $+z$  side of the nominal interaction is denoted EE+ while the other located on the  $-z$  side is denoted as EE-. The longitudinal distance between the IP and the center of the surface of the EE crystals is 3.154 cm. Each endcap is divided into two halves called *Dees* with each Dee holding 3662 crystals. Crystals in EE with identical shape

are grouped into  $5 \times 5$  units called *supercrystals* (SC). The crystals in the SC form an  $x - y$  grid. Each crystal is 220 mm ( $24.7 X_o$ ) in length and has a front face and rear cross section of  $28.62 \times 28.62$  square mm and  $30 \times 30$  square mm, respectively. Vacuum Phototriodes (VPT) instead of APDs is glued on the rear face of each crystal for scintillating light conversion into electrical signals. The VPT is used in the EE because of its high resistance to radiation and smooth operation in a strong magnetic field environment. These APDs and VPTs are used because of their high gain relative to regular photodiodes with no gain and the fact that they are not affected by the high magnetic field. Although the light yield for  $\text{PbWO}_4$  crystals is rather low ( $\approx 70$  photons/ MeV), these photo-detectors have internal gain (50 for APDs and 10 for VPTs) and quantum efficiency of 75 % for APDs and 20 % for VPTs of the emission wavelength. This makes it possible that signals from incident particles with energies of a few to high GeV longer than noise.

The signals from the APDs and VPTs are digitized by voltage-sensitive analogue-to-digital converters and through fibre-optic links transported as light signals to the counting room located adjacent to the experimental cavern.

The energy resolution and geometry structure of the ECAL ensures that the photon or electron's arrival energy, time, position and even the direction through the shape of its electromagnetic shower in the crystals can be identified and measured with good precision.

### **Hadronic Calorimeter**

The CMS Hadron Calorimeter (HCAL) is comprised of four distinct subdetectors: the Barrel (HB), the Endcap (HE), the Outer Barrel (HO), and the Forward (HF). Unlike the ECAL, the HB, HE and HO subdetectors are scintillator-sampling calorimeters with embedded wavelength shifting fibers (WLS). HB, HE and HO uses brass plates as the inactive material and plastic scintillator with WLS as the active material. The brass plate is used for absorbing the hadronic shower which comprise of an *electromagnetic*(particles like  $\pi^0$ s,  $\eta$ s and other mesons generated in the absorption process and decay to  $\gamma$ s which develop electromagnetic (em) showers) and *non-electromagnetic* components. The plastic scintilator is divided into 16  $\eta$  sectors resulting in segmentation of  $\Delta\eta \times \Delta\phi = 0.087 \times 0.087$ . It was chosen for its long-term stability and moderate

radiation hardness. energy. The scintillating light through the WLS brings the light to hybrid photodiodes (HPDs) in the HB and HE. HPDs which have high electrical noise and will be replaced with silicon photon multipliers (SiPM) which have low noise during the current CMS detector upgrade. The HB and HE combine cover a region in pseudo-rapidity of  $|\eta| < 3$ . The HB covering the region  $|\eta| < 1.3$ , is divided into two-half barrel (HB+ and HB-) sections each composed of 18 identical  $20^\circ$  wedges in  $\phi$ . Each wedge is made of flat brass alloy and steel(only front and back plates) absorber plate. HE covers  $1.3 < \eta < 3.1$  and has plastic scintillation tiles with granularity of  $\Delta\eta \times \Delta\phi = 0.087 \times 0.087$  for  $|\eta| < 1.6$  and  $\Delta\eta \times \Delta\phi = 0.17 \times 0.17$  for  $|\eta| > 1.6$ . The HO is an extension of HB outside the solenoid and thus utilizes the solenoid coil as an additional absorber. It is used to identify the starting shower and to measure the shower energy deposited after HB. The first active layer of the scintillating tiles is situated directly behind the ECAL in order to actively sample low energy showering particles from the support material between the ECAL and HCAL.

The HF occupies a pseudo-rapidity region of  $3 < |\eta| < 5$ . Its purpose is to provide a closer to  $4\pi$  hermetic phase space coverage required for missing transverse energy calculation or MET. MET is the established signal for very weakly interacting particles like neutrino and supersymmetric particles like gravitino which travel through the detector undetected. HF consists of radiation hard quartz fibers embedded in steel absorbers running parallel to the beam axis. The signal from Cherenkov light emitted in the quartz fibers in response to charged particles makes it possible to detect all charge particles in the forward region. The HF calorimeter has long and short fibers for better sampling and to distinguish showers generated by electrons and photons from those generated by hadrons. The choice of quartz fibers is because of its high resistance to the high radiation in the forward detectors and its fast production of light through Cherenkov process.

For  $|\eta| < 1.48$ , the HCAL cells map on to  $5 \times 5$  ECAL crystal arrays to form calorimeter towers projecting outwards from near the nominal interaction point. In each tower, the energy in ECAL and HCAL cells is summed to define the calorimeter energy tower. The energy ratio of an HCAL tower to an ECAL in a calorimeter energy tower can be used to improve photons and electron identification.

### 3.2.3 Muon Chambers

Muons unlike electrons and hadrons do not deposit most of their energy in the calorimeters. They are capable of traveling across the entire CMS detector into the muon chambers. Muons produce tracks which run across the CMS detector starting from the silicon pixel and strip subdetector closest to the IP called the *Tracker* and depositing very little fraction of their energy in the calorimeters unto the muon chambers. The muon chambers use the process of ionization and a 2 T magnetic field from the return iron yokes (bending the tracks of charge particles) to measure the momentum of charged particles. The three different types of muon chambers used by the CMS are: the drift tubes (DT) chambers in the barrel, cathode strip chambers (CSC) in the endcaps and resistive plate chambers (RPC) glued to the DT and CSC chambers. Four layers or stations of DT/RPC and CSC/RPC are embedded in an interleaved style with the iron yoke for track reconstruction and triggering. Figure 3.9 is a longitudinal view of the CMS detector showing the position of the muon stations. The DT and CSC record track segments characterized by the position of the track and the bending angle. This information is used to determine the precise transverse momentum and charge of particles during particle reconstruction. The RPCs(DTs and CSC will also be used after the current detector upgrade) are dedicated L1 trigger chambers used to determine the candidate muon's approximate transverse momentum and proton bunch crossing number. The RPC has a timing resolution of about 3 ns.

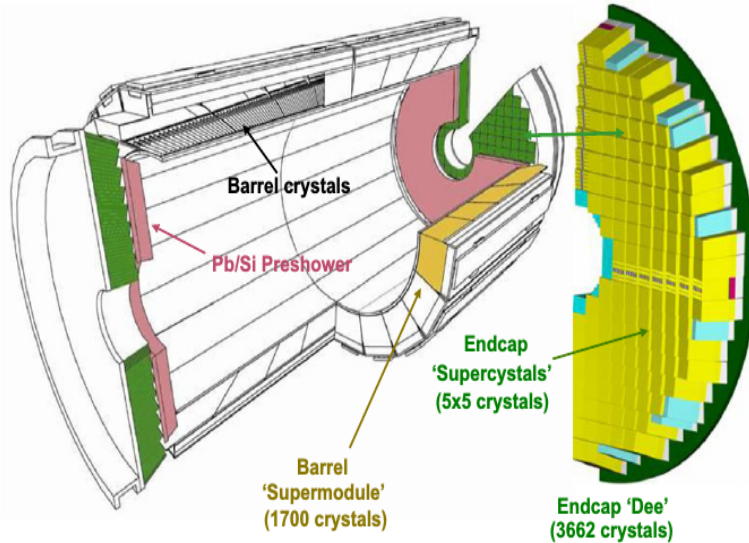


Figure 3.8: Layout of the CMS electromagnetic calorimeter showing the arrangement of crystal modules, supermodules in the barrel with the preshower in front of endcap with supercrystals.

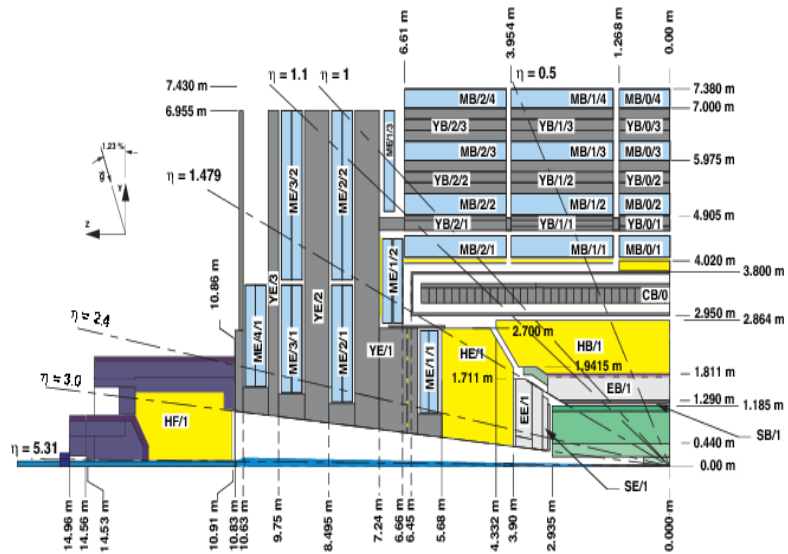


Figure 3.9: Cross section view showing the coverage range of CMS sub-detectors and their longitudinal distance from the IP.

### 3.2.4 Triggering

In CMS, there are a billion interactions including *pile up* (PU) happening each second. This means data from each 25 ns proton-proton collision has to be processed and stored before the next collision happens. Also, since not all these collisions produce interesting physics events, we have to be capable of selecting only interesting physics events produced from proton-proton collisions with sufficient energy. The process of selecting such interesting events is called *triggering*. CMS uses a two level triggering system for selecting interesting events produced with enough energy from collisions. The comprise of the *Level-1* (L1) and *High Level Triggers* (HLT) triggers.

The L1 triggers is a hardware designed electronics system implemented in FPGA and ASIC technology and uses information from the calorimeter, muon trigger and a global trigger board. The global trigger board makes the final decision based on the calorimeter and muon triggers to reject or keep an event for further processing at the HLT trigger. The L1 trigger is responsible for selecting the best 100,000 events/second from the initial 1 billions events/second produced.

The HLT is a software comprised of implemented selection algorithms running on a farm of more than 1000 standard computers. These complex algorithms include instructions like, match tracks to hits from the muon chambers, select energy deposits above a certain threshold in the calorimeters with no tracks for electromagnetic objects, and begins the first step of event selection. Just like the L1 trigger, the HLT uses assimilated and synchronized information from different parts of the CMS detector to create the entire event. By the time this selection process is complete, there are now only 100 events/second with the remaining 99,900 thrown away. Taking an average event size to be 1 Megabyte, in a stable and effective LHC proton collision period of a year or  $10^7$  seconds, CMS produces about a Petabyte of data which is stored and used later for offline physics analysis.

## Chapter 4

# Time Reconstruction and Resolution

### ECAL Time Overview

The ECAL was designed to precisely measure the energy of electrons and photons produced in proton-proton collisions, with a target barrel resolution of 0.5% for photons with energies larger than 50 GeV. In addition to energy measurements, the combination of fast scintillation for PbWO<sub>4</sub> crystals, the electronic pulse shaping and sampling rate of 40 MHz allow for excellent time measurements to be made with ECAL. A pulse shape matching of less than 1% non-linearity by the pulse shaping chip in each channel, ensures a linear and uniform pulse height from among all the channels in the ECAL. The time measured by each channel is reconstructed from 10 discrete samples of the digitized analog pulse height of the electronics, using a time reconstruction algorithm.

#### 4.1 Electromagnetic Calorimeter Readout Electronics

The scintillating light from the PbWO<sub>4</sub> crystals is readout and converted into electric current using Avalanche Photo-Diodes (APD) and Vacuum Photo-Triodes (VPT) in the barrel and endcap detector regions, respectively.

The ECAL electronics readout and control system comprise of the Front End (FE) electronics ( mainly consisting of radiation hard ASIC chips) installed inside the detector

volume at the back of ECAL and the Off Detector (OD) electronics in the upper counting room. the FE electronics is connected to the OD electronics by 100 m radiation hard Gigabit Optical fiber Links (GOL) for transporting the optical data stream.

The FE has a crystal arrangement in matrixes of  $5 \times 5$  crystals called *Trigger Towers* in barrel, which is based on the electronics arrangement and a  $5 \times 5$  mechanical arrangement of crystals called *Super-Crystals* in the endcaps. Each FE board hosts five Very Front End (VFE) boards with each holding five analog channels shown in right schematic diagram of Figure 4.1. Each channel, shown in the left schematic diagram of Figure 4.1, consists of a Multi-Gain Pre-Amplifier (MGPA) and a 12 bit Analog-to-Digital Converted (ADC) used to amplify, shape and digitize the signal coming from the Photo-Diodes.

The MGPA chip uses 3 gain ranges with gain ratios of 1,6 and 12 to span the overall dynamic range of the signal. Equipped with a CR-RC filter with a pulse shaping time of 40 ns and less than 1% of non-linearity, the MGPA ensures a linearity and pulse shape matching across all three ranges which allows for precise pulse shape reconstruction. The readout and precision performance requires a multi range 12-bit ADC chip with a sampling frequency of 40 MHz to digitize the analog pulse signal of the highest unsaturated range into 10 discrete samples, with an electronic noise of about 40 MeV.

The FE board also is also equipped with a Clock and Control Unit (CCU) chip which enables the exchange of control information between the OD and the FE electronics through a Clock and Control link.

The digitized data are stored in pipeline buffers until a Trigger Level 1 (LV1) accept decision is made. At the same time the digitized data are sent to a digital signal processing FERNIX chip which performs Trigger Primitive Generation (TPG) for the LV1 trigger system. The TPs are sent to the Trigger Concentration Card (TCC) on the OD electronics at a rate of 1 word/25 ns. Upon a positive trigger LV1 decision, the data samples corresponding to a single event are transferred to primary event buffers which are eventually merged and sent to the Data Concentration Card (DCC) through Readout links at 800 Mbps. The crystal readout data from the FE board is collected by the OD electronics DCC.

The OD board hosts the DCC, TCC and a Clock and Control System card (CCS). The TCC completes TPG process by combining the TPs generated and transmit them

to the regional Calorimeter Trigger system while the CCS is primarily task with distributing fast timing signals (LHC 40 MHz clock and trigger commands) to the FE and OD electronics and to synchronize their operation. A common clock distribution serving  $5 \times 5$  readout unit of the FE helps minimize channel-to-channel synchronization.

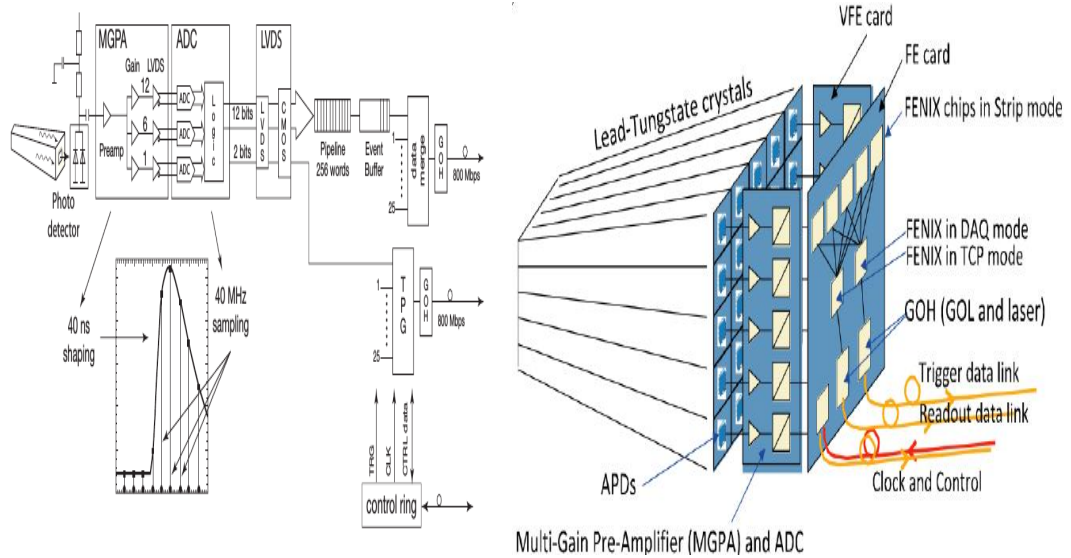


Figure 4.1: Schematic diagram of the CMS ECAL electronics readout for a single channel(Left) and the entire Trigger Tower or Front End (FE) Card(Right).

## 4.2 Time Reconstruction

An analog pulse shape from a single channel is shown in Figure 4.2(a). Overlaying the pulse shape are typical 10 digitized samples in red. The first three samples are taken in the absence of a signal and correspond to the pedestal. The ADC chip responsible for the digitization, has a sampling frequency of 40 MHz, i.e. one sample is made every 25 ns, which is the same rate as the LHC proton-proton bunch collision frequency of one bunch crossing every 25 ns. In addition, the timing phase between each sample and the next is adjusted so that the maximum of the signal pulse shape corresponds to one of the samplings within 1 ns. A time reconstruction algorithm uses these 10 digitized samples to measure the time of a single channel by finding the precise time corresponding to the maximum of the pulse shape,  $T_{\max}$ .

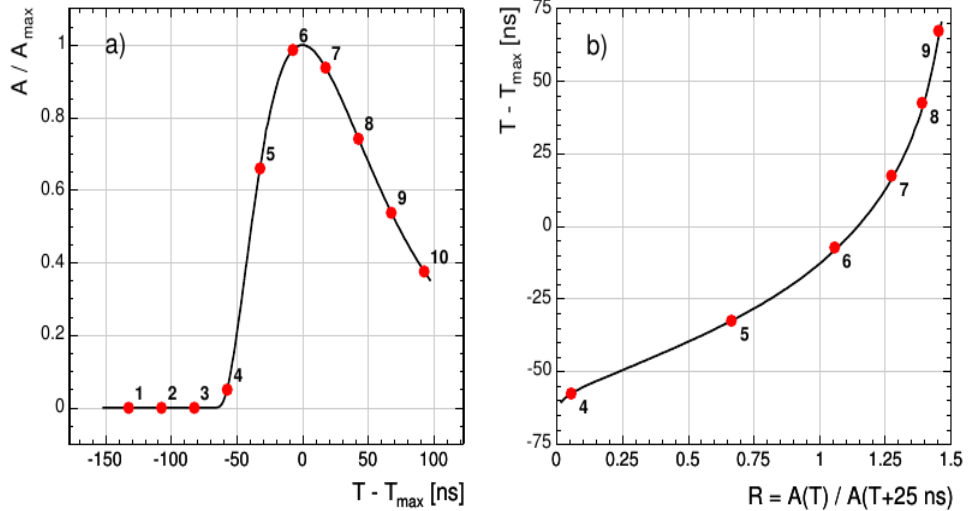


Figure 4.2: (a) A measured ECAL pulse shape for a single channel. (b)  $\mathbf{T} - \mathbf{T}_{\max}$  Vs  $R(T)$  relationship whose inverse is  $T(R)$ . Solid line is pulse shape from test beam while dots are typical 10 discrete samples corresponding to signal from proton-proton collision.

Precise measurement of  $\mathbf{T}_{\max}$  relies on good knowledge of the pulse shape. To find  $\mathbf{T}_{\max}$  using the pulse shape, a ratio algorithm uses the ratio

$$R_i = A(T_i)/A(T_{i+1}), \quad (4.1)$$

where  $T_i$  is the time of the time of the beam crossing that the  $i^{\text{th}}$  pulse height sample is taken. Each pulse height ratio is uniquely determined from the pulse shape as shown in Figure 4.2(b) which shows the the pulse height ratio,  $R_i$ , as a function of the time that the pulse height of the first of a pair of samples is taken relative to the time of the maximum height of the pulse,  $\mathbf{T}_i - \mathbf{T}_{\max}$ . Using the inverse of this function,  $T(R)$ , we can obtained  $\mathbf{T}_{\max} = T_i - T(R_i)$  and the uncertainty,  $\sigma_i$ , for each  $R_i$  point.

The uncertainty on each measurement is a product of the derivative of the function  $T(R)$  and the uncertainty on the value of  $R_i$  which itself depends on three separate uncertainties: the noise fluctuation ( $\sigma_n$ ) of each sample, the uncertainty in the estimation of the pedestal value which is always subtracted from the measured value and the truncation during 12-bit digitization. These uncertainties are uncorrelated and can be added in quadrature,[35].

A more precise value of  $T_{max}$  is obtained by using the ratios  $R_4$  through  $R_7$ . The other ratios are not used for the estimation of  $T_{max}$  because their associated uncertainties are large due to the large slope of the  $T(R)$  function. A weighted average of each  $T_{max}$  and  $\sigma$  obtained from ratios  $R_4$  through  $R_7$  as expressed in Equation 4.2 gives the best estimate of  $T_{max}$  and uncertainty.

$$T_{max} = \frac{\sum \frac{T_{max,i}}{\sigma_i^2}}{\sum \frac{1}{\sigma_i^2}} , \quad \frac{1}{\sigma_T^2} = \sum \frac{1}{\sigma_i^2} \quad (4.2)$$

The sum is from  $i = 4, \dots, 7$ .

## 4.3 ECAL Time Performance from Test Beam

### 4.3.1 ECAL Time Resolution

The intrinsic time resolution of ECAL,  $\sigma(t)$ , measured during test beam, consist of three main contributions which can be summed in quadrature since they are uncorrelated. These three contributions are the noise, stochastic and constant terms. The *Noise* ( $N$ ) term arises from the electronic noise, coherent movement of the baseline and effects overlapping hits some of which come from other soft proton-proton collisions called *pile up* (PU) events. The *Stochastic* term ( $S$ ) is from fluctuations in the number of photons collected during the sample times. Lastly, the *Constant* term ( $C$ ), whose contribution is independent of the energy deposited and arises from variations in the point of shower initiation within the crystal and variations in the pulse shape for each channel. The full expression for time resolution with all three contributions is given in Equation 4.3,

$$\sigma^2(t) = \left( \frac{N}{A/\sigma_n} \right)^2 + \left( \frac{S}{\sqrt{A}} \right)^2 + C^2, \quad (4.3)$$

where  $A$  is the measured amplitude corresponding to the energy deposited and  $\sigma_n$  is the intrinsic noise in the amplitude for individual channel.  $\sigma_n$  has a value of 42 MeV and 140 MeV in the barrel and endcap, respectively.  $N = 33$  ns has been estimated from Monte Carlo (MC) simulation studies. Contribution from the stochastic term, ( $S$ ) is small, with a value of  $S < 7.9$  ns·MeV<sup>1/2</sup>.

To measure the intrinsic time resolution of ECAL and study the pulse shape, H2 and

H4 test beam facilities at CERN were used. Prior to installation at the CMS detector, about 25% of the barrel and endcap crystals were exposed to electron beams with energy between 15 GeV and 250 GeV. The time resolution was obtained from the Gaussian distribution of the difference in time of two crystals sharing energy and belonging to the same electromagnetic shower. Note that the contribution from crystal-to-crystal synchronization does not contribute to the constant term in this study. Neglecting the stochastic term because its contribution is negligible, Equation 4.3 reduces to:

$$\sigma^2(t_1 - t_2) = \left( \frac{N}{A_{eff}/\sigma_n} \right)^2 + 2\bar{C}^2 \quad (4.4)$$

where  $A_{eff} = A_1 A_2 / \sqrt{A_1^2 + A_2^2}$ , while  $t_{1,2}$  and  $A_{1,2}$  are the times and amplitudes of the two crystals.  $\bar{C}$  is their residual constant term contribution. The time resolution is measured from the standard deviation of a Gaussian fit to the time distribution from each slice of  $A_{eff}/\sigma_n$  of the  $A_{eff}/\sigma_n$  distribution. The resulting distribution of  $\sigma(t_1 - t_2)$  of these standard deviations plotted against  $A_{eff}/\sigma_n$  is used to extract the noise and residual constant terms. The result presented in Figure 4.3 gives a noise factor  $N = (35.1 \pm 0.2)$  ns and  $\bar{C} = (20 \pm 4)$  ns obtained from test beam experiment.

The value of the  $N$  in this study agrees with our Monte Carlo estimate to within 6%. Other studies of the timing resolutions using the time difference between two basic clusters of separate electromagnetic shower was used and the results gave similar values of  $N$ .

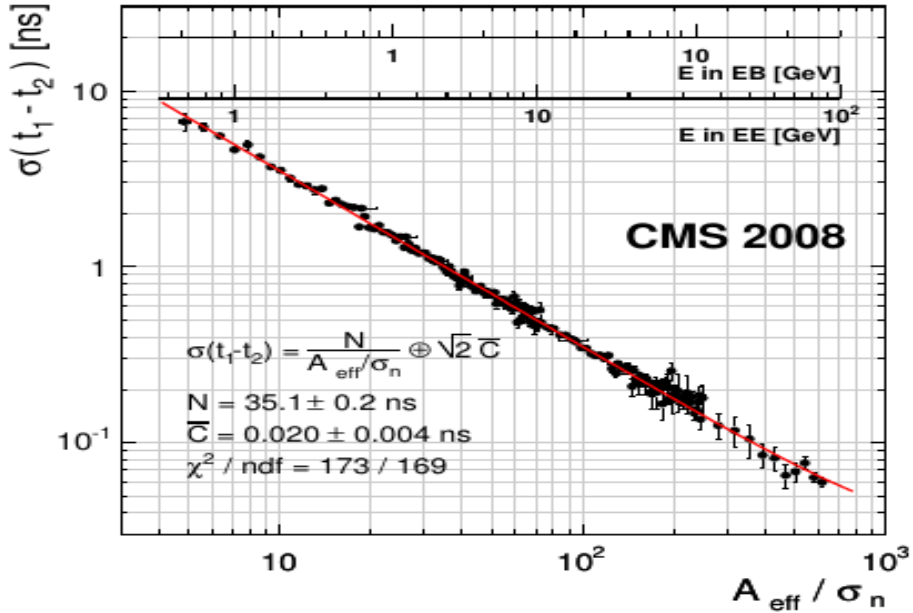


Figure 4.3: Difference in the time measurements as a function of  $A_{\text{eff}}/\sigma_n$  of two crystals sharing an energy and belonging to the same electromagnetic shower obtained during electron testbeam measurements. The single crystal energy scales for barrel (EB) and end-cap (EE) is overlaid. The fitted results give  $N = (35.1 \pm 0.2)$  ns and  $C = (20 \pm 4)$  ns.

An intrinsic time resolution better than 0.1 ns for energy  $E > 20$  GeV in EB is realized from test beam. Knowing that it takes on average 4.3 ns for a photon to reach the ECAL surface produced from proton-proton interaction point, this demonstrates an intrinsic time resolution of 2% for photons with energy  $E > 20$  GeV in the barrel.

#### 4.4 ECAL Time Performance from Collision

Ofcourse, we do not expect the ECAL time resolution in the LHC proton-proton collision environment to be as precised as test beams studies show. Therefore, it is imperative to determine the ECAL time resolution in an LHC environment as knowing the ECAL time resolution in LHC operation can be used for other purposes like eliminating particles such as cosmic rays, beam halo muons, electronic noise and out-of-time proton-proton interactions with broad time distributions. There are factors like clock time variations

over extended time, timing bias with energy and losses in crystal transparency due to radiation which would lead to different pulse shapes which worsen the ECAL time resolution. Thus, a robust crystal time calibration procedure is required if we are to match the intrinsic time resolution realized in test beam studies that we mentioned above. In addition, precise ECAL time during collision can be used in the search for photons with late arrival time produced from the decay of slow moving particles with  $\beta \ll 1$ , photons traveling along a path which significantly deviates from the obvious straight path from the proton interaction point.

#### 4.4.1 Time Calibrations

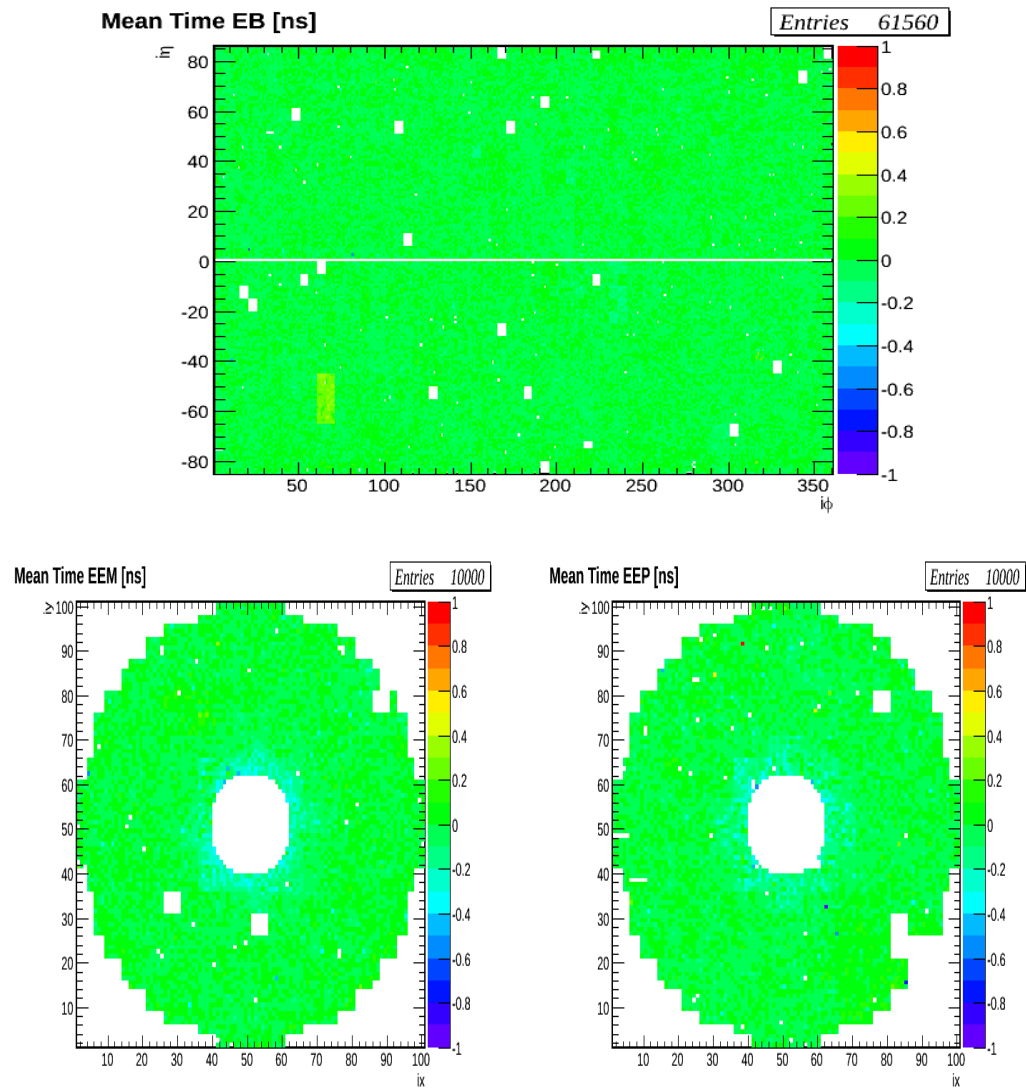
Variations in the crystal time maybe caused by the non-uniform response to electromagnetic showers of each crystal causing difference in pulse shapes or by clock time shifts introduced by interventions during technical shutdowns for machine repairs. These variations can be about 1 to 3 ns on average. To reduce these contributions, we continuously time align all 75,848 PbWO<sub>4</sub> crystals in ECAL by performing crystal *time calibration* once or twice every month. Time calibrating these crystals ensures that there is a uniform response by all the crystals to photons produced from proton-proton collisions, at interaction point, and traveling along a straight path with speeds close to the speed of light to ECAL. It equally guarantees the synchronization of most particles of an event and assigns each event to the correct LHC proton bunch crossing.

The presence of the “ $T_{max}$  Phase”, the difference in pulse shape between each crystal, variation in time of flight by a few nanosecond (ns) and the different intrinsic delays in each channel motivates a time calibration at two separate levels. At the level of the front end electronics (FE) consisting of  $5 \times 5$  crystals, We perform an initial internal time synchronization by adjusting the time measured by each trigger tower in steps of 1.04 ns among all the trigger towers. Determining the trigger tower time constants needed for time aligning these trigger towers takes place during the process of *Hardware Synchronization*. Offline, we assign time constants to each crystal, during hit reconstruction using the CMS reconstruction software during the transition from uncalibrated hits to calibrated hits.

## Offline Time Calibration

The purpose of the offline calibration is to provide time calibration constants for each crystal during event reconstruction. These constants are derived from data recorded during proton-proton collisions and are used to adjust for any clock time shift. A crystal time shift of about 1 ns is caused by the relative time shift between the CMS and the LHC clocks and time shift of about 3 ns to 5 ns is caused by time offsets in the local CMS clock introduced during hardware interventions. The local time offsets is specific only to certain regions of the ECAL detector. The calibration constants for each crystal is the reverse sign of the average time of all the reconstructed energy deposits (rechits) in the crystal. New sets of calibration constants are produced each month throughout the entire LHC run period. Each set of time constants produced has an *interval of validity* (IOV). A total of 17 IOV time constants were produced for the entire LHC run in 2011 and 44 IOV time constants for 2012.

The data sample use for producing the calibration time constants contains mostly electromagnetic particles of mostly loosely triggered photon, electron and hadrons with large electromagnetic shower which travel with nearly the speed of light and largely deposit most of their energy at ECAL. Events of these data samples undergo a rigorous event selection process in order to minimize contamination from events not produced from proton-proton collisions like cosmic muons, beam halos and electronic noise. The produced constants are validated through a full cycle hit reconstruction-time adjustment-hit re-reconstruction procedure of a chosen sub data sample. The validate constants are then used during full event reconstruction. The maps in Figure 4.4, show two dimensional distribution maps of the average time (time calibration constants) for each of the 61,200 crystals in EB and 14648 crystals in EE. The figure shows each crystal average time before (*top 3 plots*) and after (*bottom 3 plots*) calibration. More information about crystal time calibration for the entire LHC Run 1 is found in [36].



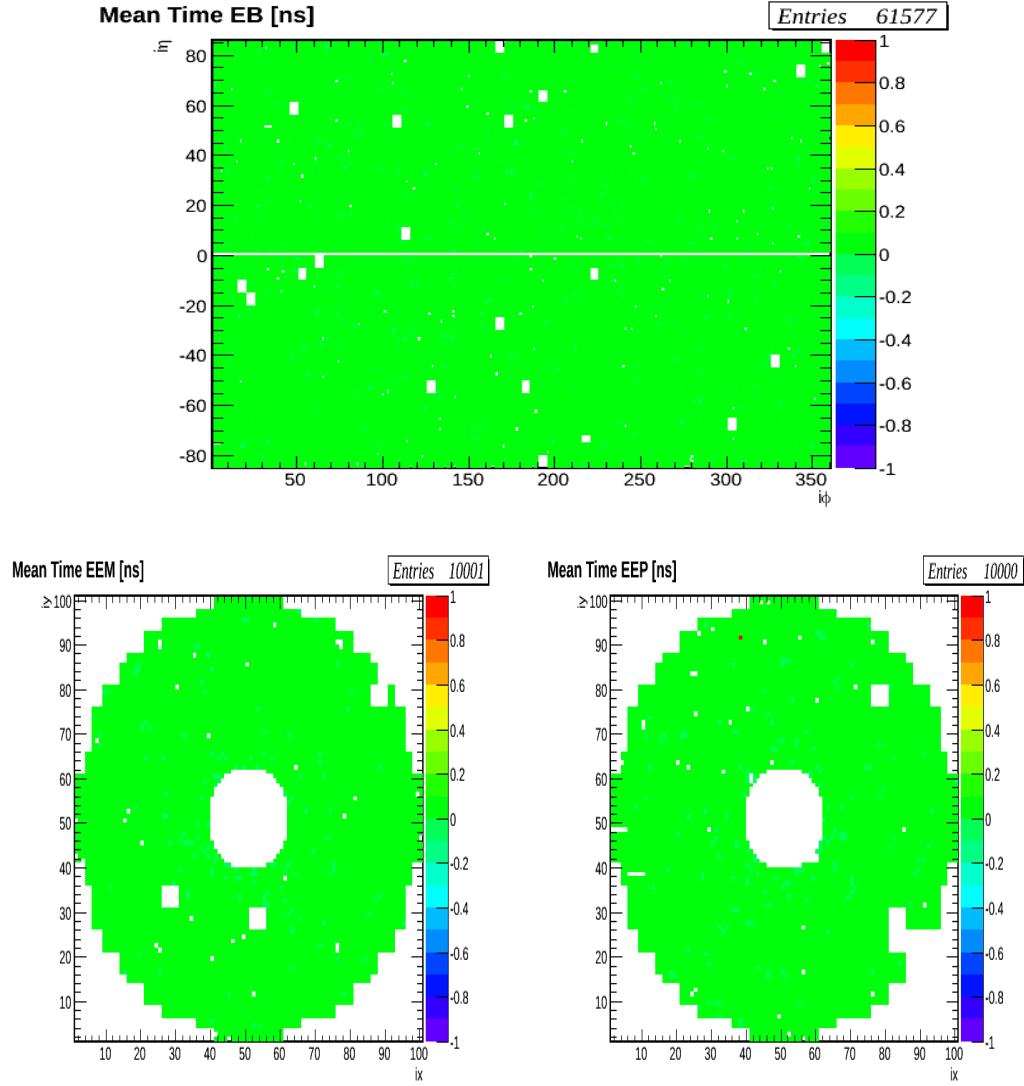


Figure 4.4: *Top 3*: Time calibration maps showing the distribution of mean time for each channel/PbWO<sub>4</sub> crystal in EB (top) and EE (below: EE-(left), EE+(right)) before calibration. *Bottom 3*: Time calibration maps showing the distribution of mean time after calibration. After calibration most crystals have an average time of zero(GREEN).

### Hardware Time Calibration

Time offsets introduced during hardware interventions for ECAL front end electronics repairs are calibrated at the level of trigger towers. Most often the adjustment of the

hardware time latency happen during the process of CMS data recording. These time alignments can be done using either data from proton-proton collision or from laser.

### **Hardware Time Calibration With Collision**

The approach for adjusting hardware time offsets during CMS data recording with ECAL for stable proton-proton collision beams involves interfering with the data recording process in order for the hardware time adjustments to be made. This interference during stable proton beams causes frequent data recording downtimes leading to data lost. Frequent down times is one of the causes for the difference between the luminosity recorded by CMS detector compared to luminosity delivered by the LHC. Even though we can argue that this procedure for adjusting the observed trigger tower time shifts using collision data is self efficient, the large CMS data recording downtime and loss of luminosity makes it less dependable especially during frequent machine interventions. To remedy the situation, a laser based time latency adjustment approach can be used.

### **Hardware Time Calibration With Laser**

The ECAL laser system comprise of two lasers, a 440 nm wavelength (close to peak emission for PbWO<sub>4</sub> crystals) laser for monitoring crystal transparency losses and a 796 nm wavelength laser for monitoring readout electronics chain from photodetectors to the electronics (i.e. APDs to ADCs). Both lasers have a jitter of less than 4 ns and as a result, the time from the lasers is averaged over 600 event pulses. The time for each crystal from the laser is expected to be the same as the time from collision data and is represented as  $T_{\text{MAX}}^{\text{APD}}$ . The laser system is also equipped with a fast acquisition card called MATACQ. The time for each channel recorded using the Matacq is also averaged over 600 event pulse and denoted  $T_{\text{MATACQ}}$ . The difference,  $T_{\text{MAX}}^{\text{APD}} - T_{\text{MATACQ}}$ , of the two times, averaged over the 25 crystals of a Clock and Control Unit (CCU) is used as the time for each CCU,  $t_{\text{CCU}} = \langle T_{\text{MAX}}^{\text{APD}} - T_{\text{MATACQ}} \rangle$ . To obtain the time shift of 25 crystals belonging to the same Front End (FE) electronics, we monitor for change of this time average before ( $t_{\text{CCU}}^B$ ) and after ( $t_{\text{CCU}}^A$ ) hardware intervention during detector maintenance. The time difference,  $\Delta t_{\text{CCU}} = t_{\text{CCU}}^A - t_{\text{CCU}}^B$ , is averaged over all the 25 crystals, i.e.  $\langle t_{\text{CCU}}^A - t_{\text{CCU}}^B \rangle$ , is the time shift, and the time calibration constant for the CCU is of opposite sign so that after correcting, the average time

of the CCU is zero. This is done for all the 68 CCUs in a given supermodule (SM) or front end detector (FED). The global time shift of a given FED is caused by the non-homogeneous laser light distribution on all CCU or trigger towers. Each FED has 1,700 PbWO<sub>4</sub> crystals and we produced laser based time calibration constants for all its crystals. Using laser data, we are able to measure the time shift of each CCU to within 0.2 (0.5) ns EB (EE) in precision. Compared to calibration using collision data, there are no downtime in CMS data recording as we can adjust for any hardware time shift prior to stable proton beams. The full procedure including technical details for performing hardware latency adjustments online using collision data or laser data is well described in [37].

#### 4.4.2 Time Bias

An additional source contributing to poor time measurement arise from energy related time bias. This bias originates from the time reconstruction algorithm. It is expected that the ratio approach for time reconstruction performs efficiently for all ADC counts. However, during data recording in LHC Run 1, it was observed that for high ADC counts produced by very energetic particles, an inherent bias in the time is introduced by the multi-gain pre-amplifier electronics for electromagnetic particles with energy above certain gain transition points. The full conversion of the energy of a particle recorded by a crystal in ADC counts to GeV is expressed as;  $E_i = G \cdot S_i(t) \cdot C_i \cdot A_i$ , where  $A$  is the amplitude from the pulse shape in ADC counts,  $G$  is the ADC-to-GeV conversion factor equal to 0.039(0.063) in EB(EE),  $C_i$  is the inter-calibration coefficients accounting for individual channel response to the electromagnetic shower and  $S_i(t)$  is the correction term obtained from laser accounting for radiation-induced channel response.  $S_i$  changes over time. The first gain transition point (Gain-1) of the multi-gain pre-amplifier occurs at 4096 ADC counts corresponding to 159.744 GeV in EB and 258.048 GeV in EE. The subsequent Gain 6 and 12 transitions occur at energy values of TeV.

The ratio algorithm introduced time bias at gain transition points which need to be adjusted. These adjustments are made on an energy dependent basis during event reconstruction for a particular CMS event reconstruction software (CMSSW) release. Figure 4.5 shows the comparison between two CMS event reconstruction software releases, CMSSW44X, where these time bias corrections have not been made and CMSSW53X,

where the the corrections have been made. Evidently, the average time displayed in both CMSS44X and CMSS53X show the disappearance of the time bias for all particle energy in CMSSW53X after the time bias corrections were made.

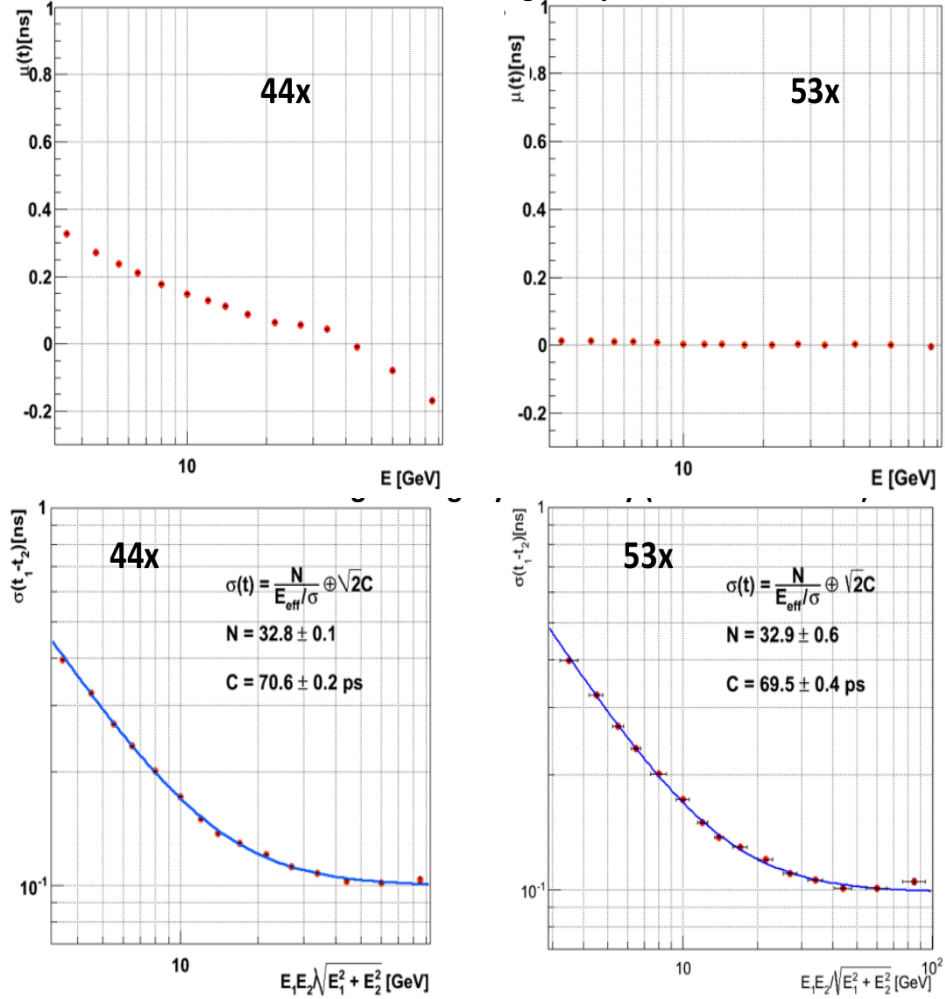


Figure 4.5: Distribution of mean time ( $\mu$ , top row) and time deviation ( $\sigma$ , bottom row) as a function of crystal energy for EB prior (left) and after (right) time bias corrections depending on energy have been applied.

To investigate further for any additional time bias un related to the particle energy, we study how the crystal geometric position in ECAL covering from  $\eta = 0$  to  $\eta = 3.142$ . The results shown in Figure 4.6 show no crystal position or  $\eta$  dependence. However, time bias of the order of 100 ps have been observed. There are efforts to understand

the source of these time bias with speculations that the time bias might be caused by electronics or loss in  $\text{PbWO}_4$  crystal transparency due to radiation.

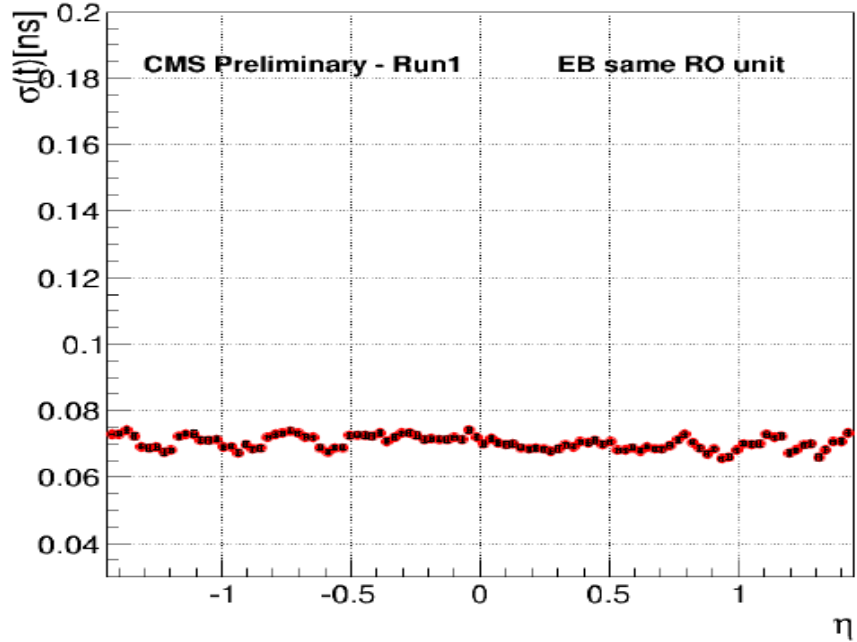


Figure 4.6: Distribution of the time standard deviation ( $\sigma$ ) against crystal geometrical position,  $\eta$ , in the ECAL barrel. Almost flat distribution of  $\sigma$  with  $\eta$ .

#### 4.4.3 ECAL Time Performance With Z Events

We evaluate the precision of ECAL time measurements during proton-proton collisions by studying the time measurement of a well understood physics process; the decay of the  $Z$  boson to an electron pair, i.e.  $Z \rightarrow e^-e^+$ . We use the standard deviation (time resolution),  $\sigma_{eff}$ , of the difference in arrival time of the two electrons to evaluate ECAL time performance. The standard deviation is obtained from the difference in the seed time,  $t_{seed}$ , of the electron electromagnetic shower of each electron after correcting for contributions from the bending of the electron travel path inside CMS magnetic field of 3.8 T. In Figure 4.7, we present the distribution of the time difference,  $t_{electron1} - t_{electron2} = t_{seed1} - t_{seed2}$ , of both electrons adjusted for time of flight corrections and in Figure 4.8, we show the time resolution or  $\sigma_{eff}(t_1 - t_2)$ , obtained from the time distribution of the seed crystal time without correcting for the bending of the electron's

flight path contributions. A time resolution of 232 ps in EB and 384 ps in EE is realized. However, if we remove the contributions from the spread in time,  $\sigma(t_{\text{collision}})$ , due to the finite time it takes for the two proton bunches of length 5.5 cm to collide; which is about  $\sigma(t_{\text{collision}}) = \sigma(t_Z) = 183 \text{ ps}$ , we obtain an improved time resolution of 142 ps in EB and 337 ps in EE. The selection for Z candidate events required that the electrons have a transverse energy bigger than 10 GeV and the reconstructed Z mass is within,  $60 \text{ GeV} < m_{\text{inv}}(e_1, e_2) < 150 \text{ GeV}$  in order to ensure mostly good Z boson candidate events are used.

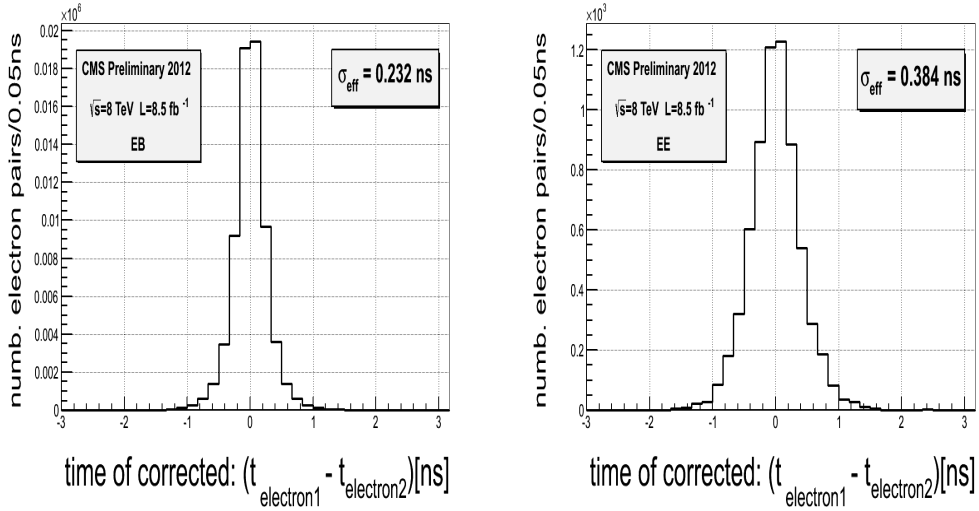


Figure 4.7: Ecal time difference between the two reconstructed electrons in  $Z \rightarrow e^-e^+$  decay. The electron time is the seed (crystal with highest energy deposit) time with additional correction due to the time of flight of the electron in EB and EE

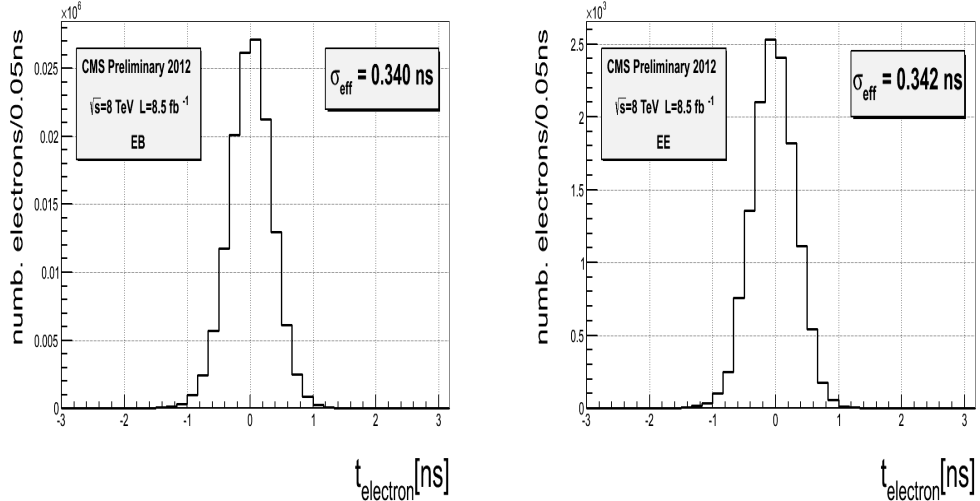


Figure 4.8: Ecal absolute time of a single reconstructed electron in  $Z \rightarrow e^-e^+$  decay. The electron time is the seed (crystal with highest energy deposit) time of the electron in EB and EE

We also investigate the contributions attributed to the readout electronics on the time resolution using events with  $Z \rightarrow e^-e^+$  decay. Figure 4.9(left), shows the time resolution obtained from measuring the electrons arrival time in the case where the seed crystal time of both electrons is read from the crystals belonging to same ReadOut (RO) electronics and compared to the other case where the seed crystal time is read from crystals belonging to two different readout electronics shown in Figure 4.9(right). The Constant term,  $C$ , for the same RO electronics is about 67 ps while that for different RO electronics is 130 ps indicating that electronic readout de-synchronization contributes to the worsening of the time resolution.

Despite, the observed 100 ps bias which seems to be related to readout electronics, we argue that, with a time resolution of  $\sigma(t) \leq 400$  ps, the ECAL subdetector is very reliable for time measurements and can be used in the search for delayed electromagnetic particles produced in the decay of long-lived particles.

The ECAL time resolution for the entire LHC Run 1 of 2011 and 2012, comparing the absolute and single precision time measurements is summarized in table 4.1.

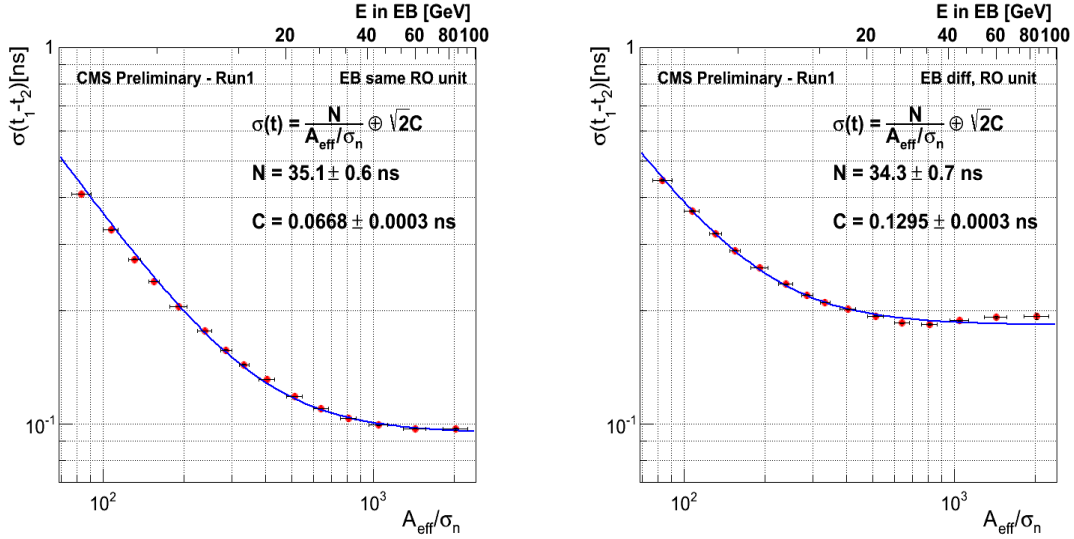


Figure 4.9: Timing resolution from: *left*: Two most energetic crystals in the same readout unit, *right*: Two most energetic crystals belonging to different readout units, as a function of effective amplitude( $A_{\text{eff}} = A_1 A_2 / \sqrt{A_1^2 + A_2^2}$ ) normalized to noise in EB. Both crystals are from reconstructed electrons in  $Z \rightarrow e^- e^+$  events.

### ECAL Timing Resolution

2011	
Absolute Time	Single Precision
$\sigma_{\text{eff}}(t_{\text{seed}})[\text{ps}]$	$\sigma_{\text{eff}}(t_{e1} - t_{e2})/\sqrt{2}[\text{ps}]$
<b>EB</b> 376	190
<b>EE</b> 356	282
2012	
Absolute Time	Single Precision
$\sigma_{\text{eff}}(t_{\text{seed}})[\text{ps}]$	$\sigma_{\text{eff}}(t_{e1} - t_{e2})/\sqrt{2}[\text{ps}]$
<b>EB</b> 340	164
<b>EE</b> 342	272

Table 4.1: ECAL timing resolution absolute time and single precision for 2011 and 2012 of LHC Run 1

# Chapter 5

## Event Reconstruction

### 5.1 Event Reconstruction Overview

An event is comprise of one or more particles produced in a particular proton-proton collision. Event reconstruction is the process of constructing particles and their four momenta using raw data read from the electronics of the different CMS subdetectors. The process begins in each subdetector using a local reconstruction algorithm and eventually extends to all subdetectors. In the calorimeter subdetectors, an energy clustering algorithm is used to produced energy clusters and in the tracker and muon chambers, a combination of tracking algorithms is used to construct particle tracks. By matching selected tracks to energy clusters, particles like photons, electrons, muons, jets and missing transverse energy ( $E_T^{\text{miss}}$ ) are reconstructed.

### 5.2 Supercluster Reconstruction

The clustering algorithm produces a cluster of clusters called *supercluster*, of the energy of an electromagnetic shower. A supercluster is either a  $3 \times 3$  or  $5 \times 5$  crystal energy matrix. About 94% (97%) of the incident photon or electron energy is deposited in this  $3 \times 3$  ( $5 \times 5$ ) matrix of crystals in the  $(\eta, \phi)$  plane in barrel or  $(x, y)$  plane in endcap. The 3.8 T magnetic field and material in front of the calorimeter causes bremsstrahlung electrons and converted photons to deposit their energy in a cluster of crystals spread in  $\phi$ . As a result, clustering algorithms start building superclusters with

a seed crystal(crystal with the maximum energy), continue within a narrow window in  $\eta$  by summing the crystal energies along the  $\phi$  which is the direction of energy spread due to the magnetic field. Figure 5.1 is schematic picture showing the direction of the clustering process in the  $(\eta, \phi)$  plane in barrel and the fraction of electromagnetic energy coverage in a typical supercluster.

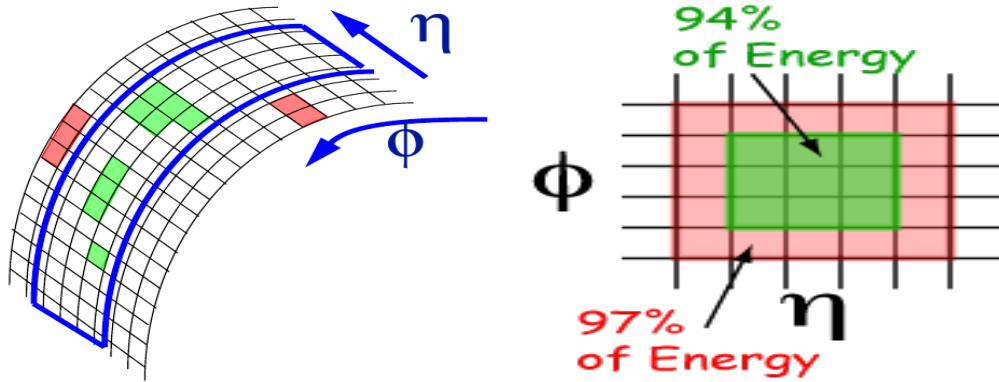


Figure 5.1: Superclustering algorithm direction in the  $(\eta, \phi)$  plane in EB and fraction of electromagnetic shower energy coverage in a crystal energy matrix.

The two major clustering algorithms used in ECAL are the *hybrid* (EB) and *island* (EE) algorithms.

- **Hybrid Supercluster Algorithm:** This algorithm is used for making super clusters in the barrel (EB). It takes advantage of the  $\eta - \phi$  geometry of barrel crystals by taking a fixed 3 or 5 crystals in  $\eta$  and dynamically search and sum separate crystals energy along  $\phi$ . The Hybrid algorithm takes advantage of our knowledge of the lateral shower shape along the  $\eta$  direction. The supercluster consists of basic clusters, usually  $3 \times 3$  crystals matrix.
- **Island Supercluster Algorithm:** This algorithm is used for making clusters in the endcap (EE). It begins by finding the seed crystal of the electromagnetic shower with maximum energy above a certain energy threshold. Using the seed crystal position, adjacent crystals are examined and added to a cluster until a rise in energy where a crystal belonging to another cluster or crystal that has no readout is reached. For each crystal to be added to the cluster, its energy read must be positive, it must not have been assigned to another cluster and the

previous crystal added in the same direction must have a higher energy. These non-overlapping clusters finally forms a “supercluster”.

### 5.3 Track and Vertex Reconstruction

Charge particle track reconstruction in CMS uses many algorithms. All these algorithms use the reconstruction positions (*hits*) during the passage of a charged particle in the silicon detectors, to determine the helix trajectories of charged tracks. These helix trajectory is used to measure the particle’s momentum and direction.

The main algorithm used for track reconstruction of proton-proton collisions is the Combinatorial Track Finder (CTF). The CTF proceeds in three stages: seeding, finding and fitting. During seeding, hits that are compatible with the interaction region above a lower  $p_T$  limit are used as possible candidates of the charge tracks. Pixel hits are the best track seeds. In the more forward region of the tracker detector,  $2 < |\eta| < 2.5$ , pixel and inner strips are used for better track finding. The track finding stage uses the Kalman Filter pattern recognition approach where, starting with the seeded parameters, the track trajectory is extrapolated to neighboring tracker layers and compatible hits are assigned to the track. During the fitting stage, the Kalman Filter algorithm is again applied where each candidate track is fitted using least-squares fitting in two stages. The first stage removes possible bias from the seeding stage while the next stage yields the best estimates of the track parameters at the original vertex. Other algorithms like the *iterative tracking algorithm* which is a general purpose tracking algorithms is used in association with customized CTF tracking algorithm to reconstruct the tracks of non-collisions events like cosmics and beam halo.

Similar to track reconstruction, vertex reconstruction involves two stages of vertex finding and fitting. During vertex finding, many tracks are grouped together into vertex candidates. The vertex finding algorithms used depends on whether it is finding primary or secondary vertex or the reconstruction of an exclusive particle decay. In vertex fitting, the best estimates of the vertex parameter like position, covariance matrix and track parameter constraint as well as the fit quality (chi-square, number of degrees of freedom, track weights) is used to distinguish among a given sets of tracks.

## 5.4 Photon and Electron Reconstruction

Photons are reconstructed from superclusters using the energy contained in a  $5 \times 5$  crystals matrix surrounding the seed crystal. Since photons are neutral, photons are identified as superclusters in ECAL not associated to any tracks or reconstructed positions in the pixel tracker. To improve photon identification, several criteria are used to distinguish true photons from other particles misidentified as photons. The criteria to identify true photons consists of tracker isolation, ECAL isolation, hadron calorimeter isolation, hadronic to electromagnetic ratio and  $R_9$ , which is the ratio of the electromagnetic energy contained in a  $3 \times 3$  matrix to the supercluster energy. The  $R_9$  variable is very useful in separating photons from the decay of  $\pi^0$  with isolated photons since the photons from  $\pi^0$  decay have a lower value of  $R_9$  compared to isolated photons.

Similar to photons, electron candidates are found when a supercluster is associated to a track reconstructed in the silicon tracker detector and in particular, its inner most layers. In electron reconstruction, the seeding approach is either driven by ECAL or by the tracker. The ECAL driven seeding approach is very efficient for electrons with  $p_T > 10 \text{ GeV}/c$ . The track driven seeding approach uses a boosted decision tree to perform a pre-selection of the tracker clusters, in order to reduced fake electrons which are light hadrons. Isolated electrons with low  $p_T$  and non-isolated electrons (electrons embedded in jets) are reconstructed efficiently using the tracker driven seeded approach. When fitting the electron tracks, we must account for the different energy loss mechanisms of the electron compared to other charged particles. Since electrons energy loss is mainly through the non gaussian nature of its bremsstrahlung, the Gaussian Sum Filter algorithm is used to provide a good estimated the track momentum both at the ECAL surface and at the interaction point.

During proton-proton collisions, in addition to events with true photons and electrons, are events produced from low energy proton-proton collisions called *minimum biased events*, events produced from the radiation of the quarks and gluons called *underlying events*, and events from multiple proton-proton interactions called *Pile Up* (PU) events, contributing to the reconstructed photon or electron energy. Additional contributions to this energy comes from poor detector calibration, poor supercluster or track

reconstruction, faulty electronics and crystal transparency loss due to radiation. The true photon or electron energy must be adjusted for these contributions during reconstruction.

An estimate of the energy deposited by an electromagnetic particle in the ECAL,  $E_{e/\gamma}$ , can be approximated using Equation 5.1;

$$E_{e/\gamma} = F_{e/\gamma} \cdot [G \cdot \sum_i S_i(t) \cdot C_i \cdot A_i], \quad (5.1)$$

where  $A_i$  is the signal amplitude in ADC counts,  $C_i$  is the inter-calibration coefficient,  $S_i(t)$  is the time-dependent corrections for response variable, usually obtain from laser,  $G$  is the global scale calibration allowing to go from energy in ADC counts to GeV and  $F_{e/\gamma}$  is the particle energy corrections for geometric, clustering and other effects. The sum is over all the crystals belonging to the photon or electron supercluster. To obtain the true electron or photon energy, energy adjustments which depend on  $\eta$  through  $F_{e/\gamma}$  are applied during supercluster reconstruction to account for detector energy mis-measurements caused by cracks between crystals and electronic noise. In Figure 5.2, we show comparisons between cases where no energy adjustments were made to those where energy adjustments (in the form of crystal inter-calibration and laser monitoring corrections for crystal transparency loss) have been made, through measuring the mass of the Z boson. We see improvements on measuring the Z mass, 91 GeV/cc, after the inter-calibration (IC) and laser monitoring (LM) corrections were made. Figure 5.3, shows the case where adjustments are made during supercluster reconstruction. Once again the Z mass is well reconstructed after introducing these corrections.

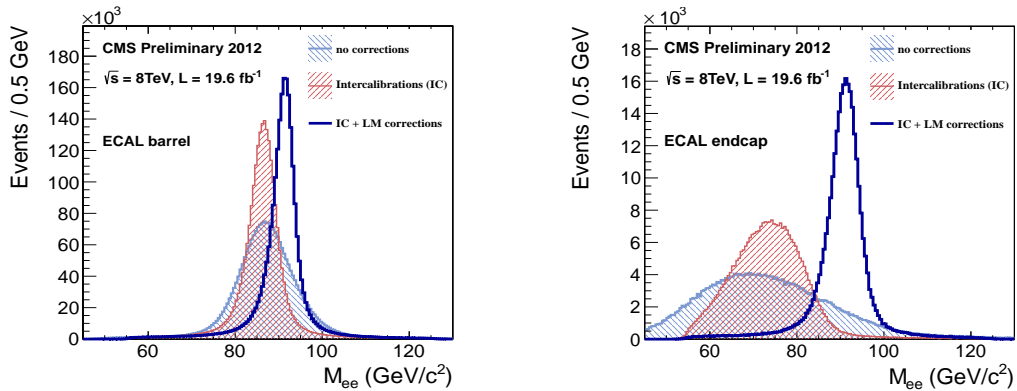


Figure 5.2: Z mass distribution from  $Z \rightarrow e^+e^-$  decay showing improvement in the measurement of the Z mass after performing energy adjustments to account for intrinsic spread in crystal, photo-detector response and time-dependent corrections to compensate for channel response loss for EB (right) and EE (left)

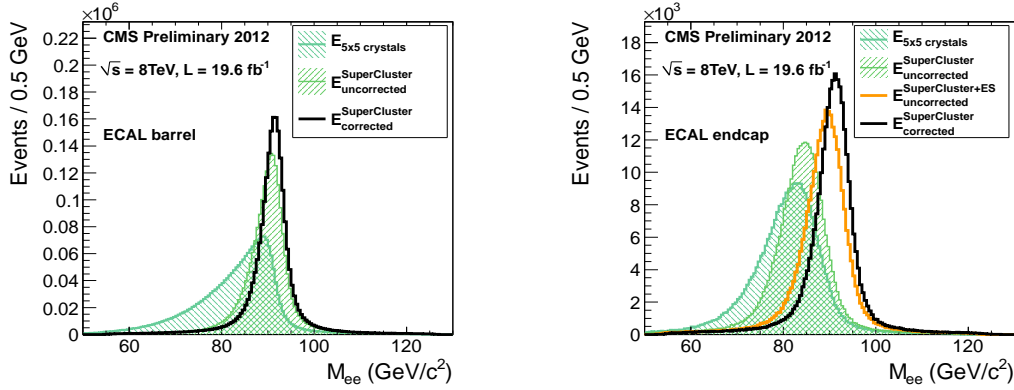


Figure 5.3: Z mass reconstructed using electron superclusters shows improvement in Z mass measurement after applying energy adjustment at superclusters for EB (right) and EE (left).

In Table 5.1, we present a summary of variables constructed using information of the spread of the electromagnetic shower in  $\eta$  and  $\phi$ , the ratio of the energy deposited in HCAL to ECAL, the track  $p_T$  and ECAL  $E_T$ , isolation in ECAL, HCAL and tracker, the ratio of the energy sums over  $3 \times 3$  and  $5 \times 5$  matrices centered on the highest energy crystal of the seed cluster;  $R_9 = E_{3 \times 3}/E_{5 \times 5}$  or  $R_9 = \sum E_9 / \sum E_{\text{Supercluster}}$  and impact parameter,  $d0$ , which is the minimum separation of the electron track computed with respect to the reconstruction vertex and track transverse momentum,  $p_T$ . Photon and electron selection using these variables, applied during electron and photon identification, have been shown to produce very good quality electron and photon candidates with efficiency above 70%.

### Simple Cut Based Electron Photon Identification

ID Variable	Electron	Photon
$H/E$	0.05(EB), 0.10(EE)	0.05
$ \Delta\eta_{in} $	0.005(EB), 0.007(EE)	0.015(EB)
$ \Delta\phi_{in} $	0.09(EB), 0.09(EE)	N/A
$\sigma_{i\eta i\eta}$	0.01(EB), 0.03(EE)	0.011(EB), 0.03(EE)
Pixel Veto	No	Yes
$ d0 (vertex)$	0.02(EB), 0.02(EE)	Veto
$ dZ (vertex)$	0.1(EB), 0.1(EE)	0.02 (cm)(Veto)
$ 1/E - 1/p $	0.05(EB), 0.05(EE)	N/A
PF isolation / $p_T$ (cone dR=0.3)	0.15(EB), 0.10(EE)	N/A
ECAL Isolation	same	$4.2 + 0.006 * E_T^\gamma +$ $0.183 * \rho(\text{EB})$
HCAL Isolation	same	$2.2 + 0.0025 * E_T^\gamma +$ $0.062 * \rho$
TRACK Isolation	same	$2.0 + 0.001 * E_T^\gamma +$ $0.0167 * \rho$
Rho corrected PF photon isolation	N/A	$1.3 + 0.005 * p_T^\gamma(\text{EB})$

Table 5.1: Simple cut-based selection criteria for electron and photon identification.

## 5.5 Muon Reconstruction

Muon tracks are reconstructed using the all-silicon inner tracker (tracker tracks) and the muon system (standalone tracks). The standalone tracks are reconstructed using reconstructed positions (hits) in the muon system consisting of the Drift Tubes (DT) in the barrel ( $|\eta| < 0.9$ ), Cathode Strip Chambers (CSC) in the endcaps ( $1.2 < |\eta| < 2.4$ ) and Resistive Plate Chambers (RPC) in the overlap region ( $0.9 < |\eta| < 1.2$ ). There are two independent muon reconstruction approaches: *Global muon reconstruction (Outside-in)* and *Tracker muon reconstruction (Inside-out)*. For Global muon reconstruction, each standalone-muon track is matched to a tracker track by comparing the parameters of

the two tracks propagated to a common surface. The global muon track is fitted combining hits from the tracker track and standalone-muon track using the Kalman-filter algorithm. For the tracker muon reconstruction, all tracks with  $p_T > 0.5 \text{ GeV}/c$  and total momentum  $p > 2.5 \text{ GeV}/c$  are considered as possible muon candidates and are extrapolated to the muon system taking into consideration the magnetic fields, the average expected energy loss in the calorimeters and multiple Coulomb scattering in the detector material to locally reconstruct segments in the muon system. A combination of different muon algorithms depending on the muon  $p_T$ , provides a robust and efficient muon identification.

Using the beam spot as constraint of the muon's vertex, it is possible to distinguish between muons produced from proton-proton collisions from those produced from cosmic *cosmic muons* and proton beams interacting with the gas in beam pipe and proton dump muon splash events produced 150 m upstream the CMS detector during proton beam dump. The proton beam related muons are referred to as *beam Halo muons*. Figure 5.4 show an illustration of trajectories of different muon sources interacting with the CMS detector.

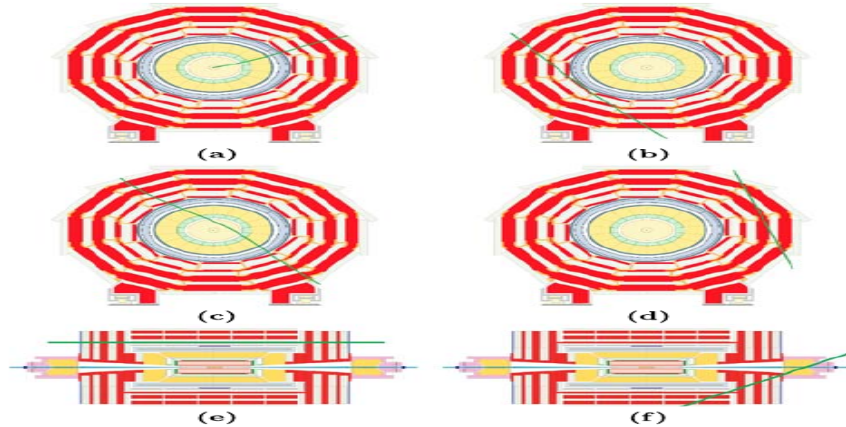


Figure 5.4: Illustration of muons from proton-proton collision, cosmic rays and beam halo. (a) Muons from collision propagating from the center and moving outwards, (b) Cosmic muons traveling through the detector leaving signals in opposite hemispheres of the muon system, (c) Cosmic muons leaving signals in the tracker and opposite hemispheres, (d) cosmic muons entering and leaving the detector without passing through the muon detector layers, (e) beam halo muons penetrating the detector and leaving signals in the endcaps and (f) Cosmic muons entering the detector through the endcap and leaving through the barrel and which can happen in a *vice-versa* manner.

### Particle Flow Algorithm

The *Particle Flow* (PF) algorithm is an algorithm for reconstructing particles combining information from the tracker, ECAL, HCAL and muon chambers of the CMS detector. It uses a combination of different algorithms comprising of calorimeter clustering, tracking and extrapolation to calorimeters, muon identification, electron pre-identification and linking of topological elements, for reconstructing a list of particles which include photons, charge hadrons, neutral hadrons, muons and electrons. The same list of particles is subsequently used to reconstruct composite “particles” like jets,  $E_T^{\text{miss}}$  and taus. The versatility of the PF algorithm is the reason why it was introduced for reconstructing Jets, missing transverse energy ( $E_T^{\text{miss}}$ ) where complete information of the event content from every subdetector is needed. The PF algorithm uses tracks, electron energy seeds, 4-momentum, super cluster energy calibration, bremsstrahlung tracks for electron and photon reconstruction making it extremely efficient at minimizing electron and photon misidentification. For  $E_T^{\text{miss}}$  reconstruction where full reconstruction of all the particles belonging to an event is necessary, the PF algorithm is very reliable.

## 5.6 Jet Reconstruction

A jet is a spray of particles arising from the hadronization of colored particles. Because jets are made of many particles like electrons, photons, hadrons, charged and neutral electromagnetic and hadronic showers, they are best reconstructed using the particle flow algorithm. Jets reconstructed using the PF algorithm are called *Particle Flow Jets*. Using calorimeter towers as input, jets can also be reconstructed using the Anti- $k_T$  clustering algorithm which combines four vectors according to their relative transverse momentum within a standard cone size of  $R = 0.5$  in the  $(\eta, \phi)$  plane. The quality of a reconstructed jet depends on the jet identification selection criteria known as the *JetID*. High quality jets are required to have an electromagnetic energy fraction (EMF)  $> 0.01$ , within the ECAL fiducial region of  $|\eta| < 2.6$ , the number of calorimeter cells containing more than 90% of jet energy ( $N_{jet}^{90}$ ) must be  $> 1$ , the fraction of jet energy in the hottest Hybrid photodetector (HPD) unit in HCAL readout within a jet ( $f_{HPD}$ ) must be  $> 0.98$ , the charge hadron fraction ( $CHF$ )  $> 0.0$  if within  $|\eta| < 2.4$ , the neutral hadron fraction ( $NHF$ )  $< 1.0$ , the charge electromagnetic fraction ( $CEF$ )  $< 1.0$ , and

neutral electromagnetic fraction  $z(NEF) < 1.0$ . These jetId selection requirements have been shown to remove mis-reconstructed jets arising from spurious energy deposition in subdetectors with good efficiency. The jet energy is often mis-measured due to cracks in the detector, non-linear responses in the calorimeters, electronic noise, poor detector calibration and additional energy from PU. Therefore, adjusting the jet energy through *jet energy corrections* (JEC) is often performed guaranteeing a reliable measurement of the jet energy during reconstruction.

## 5.7 Missing Transverse Energy Reconstruction

It is very challenging to detect particles which do not interact with the detector. Such particles include very weakly interacting particles like neutrinos ( $\nu$ ), neutralinos ( $\tilde{\chi}_1^0$ ) and gravitino ( $\tilde{G}$ ). In CMS, the presence of this kind of particles in an event is inferred through a measurable quantity called *missing transverse energy*. Measurable quantities like transverse momentum ( $p_T$ ) and cone size,  $\Delta R = \sqrt{\Delta\eta^2 + \Delta\phi^2}$ , are used to identify and distinguish particles traveling in the transverse plane,  $(x, y)$  or  $(\eta, \phi)$ , from the longitudinal plane, along the  $z$  direction. Employing the conservation of momentum in the transverse plane, we can use the imbalance in transverse momentum required to ensure conservation of total transverse momentum of an event to infer the presence of an undetectable particle traveling in the transverse plane. The amount or quantity of this transverse momentum imbalance or missing transverse momentum is called missing transverse energy (MET) or  $E_T^{\text{miss}}$ . The presence of reconstructed  $E_T^{\text{miss}}$  in an event indicates the presence of very weakly interacting particle(s) which escape the detector undetected.

We define  $E_T^{\text{miss}}$  as the magnitude of the negative vector sum of the uncorrected transverse energy deposit of all the particles in an event.

$$E_T^{\text{miss}} = \left| - \sum_n (E_n \sin \theta_n \cos \theta_n \hat{\mathbf{i}} + E_n \sin \theta_n \sin \theta_n \hat{\mathbf{j}}) \right| = |\not{E}_T^x \hat{\mathbf{i}} + \not{E}_T^y \hat{\mathbf{j}}| \quad (5.2)$$

Where,  $n$  is the sum over all calorimeter energy deposits including energy deposits in towers, reconstructed energies (hits) or generator level particle energies. In order to measure  $E_T^{\text{miss}}$  accurately, a particle detector should be as near hemispherical as possible to

allow for complete measurement of the transverse momentum of all the particles belonging to an event. The CMS detector, provides a near hemicity with its nearly  $4\pi$  solid angle coverage. This near  $4\pi$  solid angle is achieved through the hadronic forward (HF) detector with little space allowing for the passage of the proton beams. Since according to conservation of momentum, the total transverse momentum before and after collision should be the same, by measuring the  $p_T$  of every detectable particle belonging to an event after proton-proton collision, the imbalance in  $p_T$  required to ensure the conservation of transverse momentum in the event, is ascribed to the momentum carried away by undetected particle(s). This idea is used to infer the presence of neutrinos W boson decay to an electron and an anti-electron neutrino;  $W \rightarrow e + \bar{\nu}$ , where the missing transverse momentum is used to infer the presence of the undetectable neutrino.

Since particle interactions involving supersymmetry and other beyond the standard model processes involves large  $E_T^{\text{miss}}$  due to the production of undetectable particle(s) during proton collisions,  $E_T^{\text{miss}}$  is the desirable quantity to use in many particle searches involving the possible production of new very weakly interacting particles. Standard Model particle interactions produces small  $E_T^{\text{miss}}$ . In any particle search which involves the production of new weakly interacting particle, it is imperative to accurately measure  $E_T^{\text{miss}}$ , as some standard model interaction processes like machine induced backgrounds from halo muons, mis-measured energy and mis-reconstructed particles and anomalous signals like spike can lead to large  $E_T^{\text{miss}}$  mimicking the signal for new particle(s).

## 5.8 Anomalous Signals

Anomalous signals are signals read from the electronics called *spikes* with abnormally large energy deposits in the avalanche photodiodes without any scintillation in the PbWO<sub>4</sub> crystals. They are produced when neutrons or charged hadrons like protons, strike directly ionizing the silicon of the photodiode producing an electronic signal in the absence of any crystal scintillation.

Because of no scintillation, they appear much earlier (negative) in ECAL measured arrival time and often populate the earlier time of the reconstructed hit (*rechit*) time distribution. Their energy deposit range from a few GeV to ECAL saturation energy of about 1.7 TeV. Since they do not electromagnetically shower in PbWO<sub>4</sub> crystals,

their electromagnetic energy shower shape is very isolated, with only one or two crystals contributing to the energy cluster. Spikes may also have positive time appearing late or delayed in their arrival time at ECAL populating the tails of the rechit time distribution. The late arrival time is due to the slow propagation of neutrons through the CMS detector.

Numerous test beam, collision data and simulation studies,[42], have been carried out towards understanding the properties of events with spikes and how they can be tagged and removed. These studies, reveal that spikes can be identified and removed using a topological energy variable constructed as  $1 - \frac{E_4}{E_1}$  known as the “*Swiss-Cross*” (SX).  $E_1$  is the energy deposit of the central (highest energy) crystal and  $E_4$  is the sum total of the energy of the neighboring four crystals in an  $(\eta, \phi)$  plane. A selection cut in  $\text{SX} > 0.95$  rejects more than 99% of isolated spikes with transverse energy greater than 10 GeV with very little impact on the efficiency of selecting electromagnetic EM showers. Other topological variables like  $1 - \frac{E_2}{E_6}$  and  $1 - \frac{E_2}{E_9}$ , where  $E_2$  is the sum of the energy of two crystals sharing the energy deposited and  $E_6(E_9)$  is the sum of the neighboring 6(pairs-of)(9) crystals in the  $(\eta, \phi)$  plane are used. The  $1 - \frac{E_2}{E_6}$  variable is used to identify isolated spikes whose energy deposit spread in two adjacent crystals while the  $1 - \frac{E_2}{E_9}$  is used to identify non-isolated spikes i.e. spikes which are found embedded in a supercluster. It has also been shown that applying selection cuts on the rechit time of  $\pm 3$  ns leads to more than 90% efficiency for rejecting spikes. However, in this thesis, we do not require such selection cuts on the rechit time as these rechits include rechits of possible delayed electromagnetic particles with arrival time beyond 3 ns produced during proton-proton collisions.

## Chapter 6

# Search Analysis for Long-Lived Particles

### 6.1 Analysis Strategy

This analysis is about the search for events with at least a single late arrival time photon at the Electromagnetic Calorimeter (ECAL) and large missing transverse energy ( $E_T^{\text{miss}}$ ). It uses a counting method where an excess in the number of events with photon time above a defined ECAL timing threshold, to the expected number of events from background processes, indicates the presence of a new physics phenomena. Such a phenomena is the decay of a massive long-lived neutral particle into a late photon and large  $E_T^{\text{miss}}$  which is not common with standard model interactions.

We expect most of our background events of this search to arise from non-collision rather than proton-proton collision events.

#### Signal and Background Events

We expect a typical signal event of the decay of a massive neutral long-lived particle, to be produced in a proton-proton ( $pp$ ) collision at the LHC and detected with the CMS detector, according to the prediction of a benchmark Gauge Mediating Supersymmetry Breaking (GMSB) model described as the “Snowmass Points and Slope 8” (SPS8).

In this model, the massive long-lived neutral particle is the Next-to-Lightest Supersymmetric Particle (NLSP) which is the lightest neutralino ( $\tilde{\chi}_1^0$ ). The  $\tilde{\chi}_1^0$  decay into a photon ( $\gamma$ ) and the Lightest Supersymmetric Particle (LSP) called the gravitino ( $\tilde{G}$ ),  $\tilde{\chi}_1^0 \rightarrow \gamma + \tilde{G}$ . The  $\tilde{G}$  is undetected because it does not interact with the CMS detector material. Its presence is indirectly inferred by measuring the missing transverse momentum ( $E_T^{\text{miss}}$ ). The photon, because of the long-lived nature of the  $\tilde{\chi}_1^0$ , arrives late at the ECAL compared to photons produced from nominal  $pp$  collisions.

In a LHC collider, the  $\tilde{\chi}_1^0$  can be singly or pair produced in the direct interaction of the quarks/gluons (partons) inside the proton,  $q\bar{q} \rightarrow \tilde{\chi}^\pm \tilde{\chi}_1^0$  or  $q\bar{q} \rightarrow \tilde{\chi}_1^0 \tilde{\chi}_1^0$ , respectively. However, in this analysis, we are interested in cases where the  $\tilde{\chi}_1^0$  is produced indirectly from the cascade decay of heavier supersymmetric particles like gluino ( $\tilde{g}$ ) and squark ( $\tilde{q}$ ),  $gg \rightarrow \tilde{g}\tilde{g} \rightarrow q\bar{q}q\bar{q}\tilde{\chi}_1^0\tilde{\chi}_1^0$  and  $q\bar{q} \rightarrow \tilde{q}\tilde{q} \rightarrow \bar{q}q\tilde{\chi}_1^0\tilde{\chi}_1^0$ , respectively. This is because the gluino/squark production cross-section is largest at a  $pp$  collider like the LHC, and in association with the neutralino decay, the event also contains multiple high- $p_T$  jets which provide an added signal requirement useful for suppressing background events with no jets. Thus, our typical signal event should comprise of at least a single delayed high- $p_T$  photon, large  $E_T^{\text{miss}}$  and multiple high- $p_T$  jets. Finding such an event with the CMS detector will be evidence of a new physics phenomena.

Our background events could be produced from  $pp$  collisions which we call *collision background events* and from non- $pp$  collisions which we call *non-collision background events*, like the so-called beam halo, cosmic muons and spikes. Most of our background events are from non-collision background events with late photons and large  $E_T^{\text{miss}}$ .

Collision background events can mimic the  $\tilde{\chi}_1^0$  decay signal producing late photons and large  $E_T^{\text{miss}}$  in cases where the ECAL time or  $E_T^{\text{miss}}$  is mismeasured or the collision event has real  $E_T^{\text{miss}}$ . For example, multijets and QCD events, inclusive Z+jets/W+jets events, inclusive top-anti-top ( $t\bar{t}$ )+jets events and inclusive ZZ/WW/WZ+jets events can either have true  $E_T^{\text{miss}}$ ; like events with  $Z \rightarrow \nu\bar{\nu}$  and  $W \rightarrow e\bar{\nu}_e$  decays, where the undetected neutrino ( $\nu$ ) leads to true  $E_T^{\text{miss}}$ , or fake  $E_T^{\text{miss}}$  (instrumental  $E_T^{\text{miss}}$ ), where there is no undetected particle pertaining to the event but rather  $E_T^{\text{miss}}$  arising because of poor reconstruction of the energy of particles, as it is with the case for QCD events. The late photon arises when one of the jets or an electron is misidentified as a photon and its ECAL time is misreconstructed. The other jets in the event satisfy the high- $p_T$

multijets requirement.

### 6.1.1 Signal Modeling

We produced simulated high-energy-physics signal events according to the SPS8 benchmark model using general-purpose event generators based on Monte Carlo (MC) methods of numerical computations. The process of event generation starts with the production of *SUSY Les Houches Accord* (SLHA) files using a SUSY software package called **ISASUSY**[51]. These SLHA files contain the masses, interaction couplings, decay widths and all possible decay channels and their Branching Ratio (*BR*) of every supersymmetric particles. Each file also contain the value of the fundamental GMSB model parameters;

$$\left\{ \boldsymbol{\Lambda}, \mathbf{M}_{\text{mess}}, \mathbf{N}_5, \tan(\beta), \text{sgn}(\mu), C_{\text{grav}} \right\} \quad (6.1)$$

spanning all the possible, in terms of particle kinematics, supersymmetric particle production and decay configurations or phase space, as defined by the model, in the production of events. In the SPS8 model, the choice of parameters is such that

$$\text{sgn}(\mu) = 1, \tan(\beta) = 15, \mathbf{N}_5 = 1, \mathbf{M}_{\text{mess}} = 2\boldsymbol{\Lambda}, \quad (6.2)$$

where  $C_{\text{grav}}$  and  $\boldsymbol{\Lambda}$  are not fixed . By varying, respectively,  $C_{\text{grav}}$  and  $\boldsymbol{\Lambda}$ , we can exploit different decay scenarios where the  $\tilde{\chi}_1^0$  has a different lifetime and mass. For a specific choice of  $C_{\text{grav}}$  and  $\boldsymbol{\Lambda}$ , we produce a signal sample where the events have a mean lifetime ( $c\tau$ ) and mass of the  $\tilde{\chi}_1^0$ . A special software package called **HDECAY**, is used to handle the decay of all supersymmetric particles including the  $\tilde{\chi}_1^0$ .

The events are generated according to the physics process, which we described in detail in section 2.3.2, where the  $\tilde{\chi}_1^0$  production and decay to photon and gravitino is through the cascade decay of the gluino/squarks;

$$p + p \rightarrow \tilde{g}\tilde{g}, \tilde{q}\tilde{q} \rightarrow [1 \text{ or } 2 \text{ cascade decays}] \rightarrow 2\tilde{\chi}_1^0 + \text{jets} \rightarrow 2\gamma + 2\tilde{G} + \text{jets}. \quad (6.3)$$

We use **PYTHIA-6** [52] as the MC event generator. It takes as input an SLHA file and generates events of supersymmetric particles, produced at the LHC  $pp$  collider with center of mass energy,  $\sqrt{S} = 8$  TeV. The interaction of these supersymmetric particles with the

CMS detector is simulated using the **GEANT4** [53], particle detector simulation software. A full physics event is reconstructed from energy deposits (hits) in the CMS detector using the CMS event reconstruction Software (CMSSW). To minimize any disagreement between MC and data, we use the same CMSSW release version (**CMSSW\_5\_3\_29**) in the MC event reconstruction with the same detector conditions as the recorded data.

### 6.1.2 Background Modeling

Although our background estimation study is data-driven, however, we also generated a small sample of  $\gamma$ +jet(s) events at leading order cross-section. The  $\gamma$ +jet(s) MC sample is used for studying ECAL time of simulated events.

We did not produce MC samples for background events with W, Z and  $t\bar{t}$  decays because in addition to the fact that their contribution as background events is small, our high- $p_T$  ( $p_T > 80 \text{ GeV}/c$ ) photon requirement will suppress these background events further as most of the electrons from these events which can be misidentified as photons are not high- $p_T$  photons.

We also did not produce MC samples for spikes, cosmic and beam halo muons as simulations of the photon ECAL time is not very reliable especially for those events with large photon ECAL time.

### 6.1.3 Datasets

The data sample used in this analysis was produced during LHC Run 1 in 2012 with proton-proton ( $pp$ ) collisions at the center of mass energy,  $\sqrt{S} = 8 \text{ TeV}$ . We used data equivalent to total integrated luminosity of  $19.1 \text{ fb}^{-1}$  recorded by the CMS detector.

#### Data Samples

Our collision data samples comprise of triggered single photon events from luminosity sections certified as good. In Table 6.1, we present these data samples showing their corresponding integrated luminosity. The *jason* file with the list of certified good luminosity sections is **Cert\_8TeV\_PromptReco\_Collisions12\_JASON.txt**.

Data Sample	Recorded Luminosity [fb <sup>-1</sup> ]
/Run2012B/SinglePhoton/  EXODisplacedPhoton-PromptSkim-v3	5.1
/Run2012C/SinglePhoton/  EXODisplacedPhoton-PromptSkim-v3	6.9
/Run2012D/SinglePhoton/  EXODisplacedPhoton-PromptSkim-v3	7.1
/SingleElectron/Run2012A-22Jan2013-v1/AOD	5.2
/DoubleElectron/Run2012C-22Jan2013-v1/AOD	4.8

Table 6.1: Data samples and their corresponding integrated luminosity totaling 19.1 fb<sup>-1</sup> used in the our delayed photon search analysis

### Monte Carlo Samples

The MC samples were produced with *Summer 2012* prescription of the calibration and alignment status of the CMS detector and pile up conditions at 8 TeV.

The GMSB SPS8 signal samples had 50,000 events for each mean lifetime ( $c\tau$ ) and SUSY breaking scale ( $\Lambda_m$ ) or mass of  $\tilde{\chi}_1^0$  ( $m_{\tilde{\chi}_1^0}$ ). The sample are produced for different  $c\tau$  ranging from 50 cm to 1000 cm for each  $\Lambda$  or  $m_{\tilde{\chi}_1^0}$  point. We vary  $\Lambda$  from 100 TeV to 220 TeV which is equivalent to  $m_{\tilde{\chi}_1^0}$  ranging from 139 GeV/c<sup>2</sup> to 314 GeV/c<sup>2</sup>. Table 6.2 shows a summary of our signal MC samples used in this analysis with the number of events, cross-section and branching ratio for  $\tilde{\chi}_1^0$  production and decay to  $\gamma$  and  $\tilde{G}$  for each SUSY breaking scale.

The  $\gamma$ +jet MC samples were generated for different momentum of the colliding partons and normalized to the 19.1 fb<sup>-1</sup> integrated luminosity. The cross-sections,  $p_T$  of the photon ( $\hat{p}_T$ ) radiated by the colliding parton and the number of events in each sample is summarized in Table 6.3. The  $\hat{p}_T$  range from 50 GeV/c to 800 GeV/c was covered.

$\Lambda$ [TeV]	$c\tau$ (mm)	$\sigma_{LO}$ (pb)	Number of Events	Branching Ratio
100	500-10,000	0.368	50,000	0.9444
120	500-10,000	0.133	50,000	0.9042
140	500-10,000	0.0574	50,000	0.8711
160	500-10,000	0.0277	50,000	0.8464
180	500-10,000	0.0145	50,000	0.8282
220	500-10,000	0.0044	50,000	0.8282

Table 6.2: Signal GMSB SPS8 Monte Carlo samples for different  $\Lambda$  with  $50 \text{ cm} < c\tau < 1000 \text{ cm}$  and Branching Ratios (BR) studied in this analysis

$\hat{p}_T$	$\sigma_{LO}$ (pb)	Number of Events
$50 \sim 80$	3322.3	1995062
$80 \sim 120$	558.3	1992627
$120 \sim 170$	108.0	2000043
$170 \sim 300$	30.1	2000069
$300 \sim 470$	2.1	2000130
$470 \sim 800$	0.212	1975231

Table 6.3: The  $\gamma +$  jets samples studied in this analysis

We checked that the GMSB signal samples were correctly generated by PYTHIA-6, by looking at the number of photons,  $E_T^{\text{miss}}$  and number of jets in each signal event. We also measured the mean lifetime of the  $\tilde{\chi}_1^0$  by performing a fit analysis to the distribution of the  $\tilde{\chi}_1^0$  mean lifetime computed from its transverse distance traveled before decay. This distance is computed using its production and decay vertices. By comparing the computed  $c\tau$  to its theoretical value supposedly used in the event generation, we are able to validate that each signal MC sample.

We also observed that most of the events had at least a single photon (left plot) and at least 2 jets (right plot) shown in the top plots of Figure 6.5. Comparing different signal samples with  $c\tau = 2000 \text{ mm}, 4000 \text{ mm}, 6000 \text{ mm}$  of  $\Lambda = 180 \text{ TeV}$  and a  $\gamma +$  jet with  $120 < \hat{p}_T < 170 \text{ GeV}/c$  sample, we observed that the  $E_T^{\text{miss}}$  (shown in the bottom plot of the same figure) from signal events was larger than the  $E_T^{\text{miss}}$  of events from the

$\gamma +$  jet sample agreeing with our expectation that the  $\gamma +$  jet sample has mostly fake  $E_T^{\text{miss}}$  while signal samples have large  $E_T^{\text{miss}}$  due to the  $\tilde{\chi}_1^0$  decay to gravitino.

These observations gave us confidence that the signal samples were properly generated and indeed most of the signal events had at least one  $\tilde{\chi}_1^0$  which decayed to a photon and gravitino.

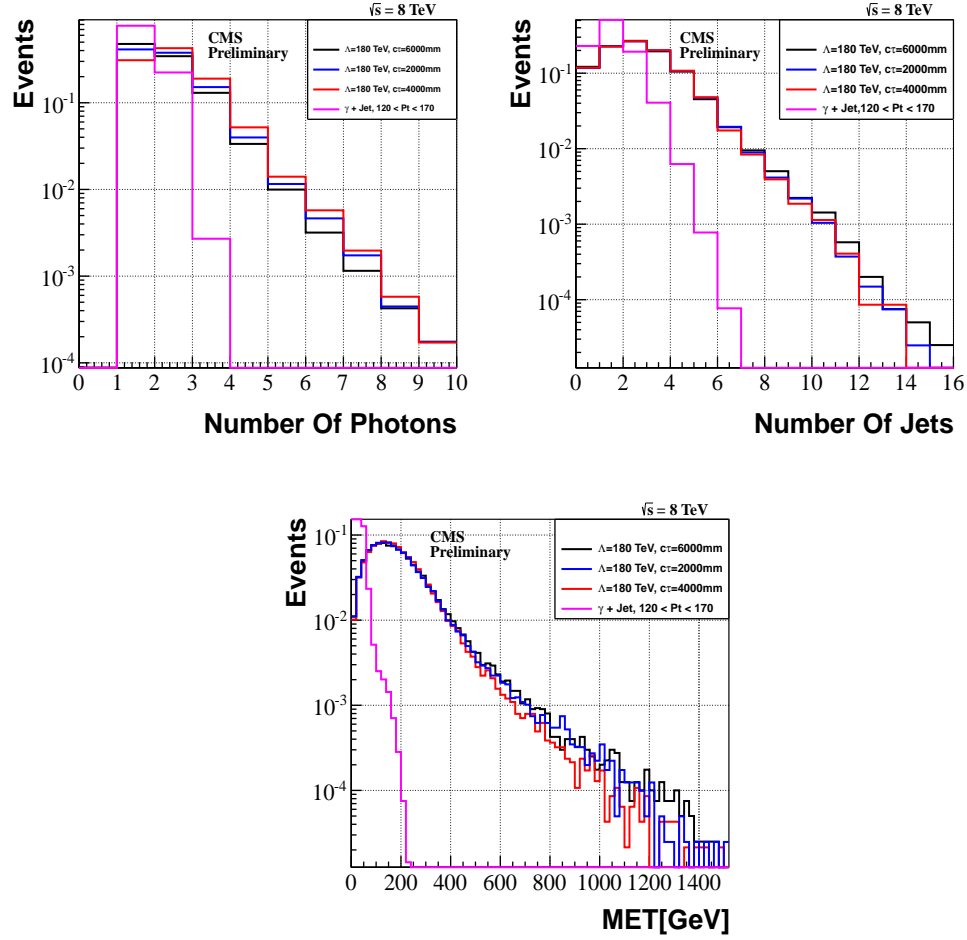


Figure 6.1: Number of photons (top left), Number of jets (top right) and  $E_T^{\text{miss}}$  (bottom) for events with  $\tilde{\chi}_1^0$  decay to  $\gamma$  and  $\tilde{G}$  for different  $c\tau = 2000 \text{ mm}, 4000 \text{ mm}, 6000 \text{ mm}$  points of  $\Lambda = 180 \text{ TeV}$  of the SPS8 model. A  $\gamma + \text{jet}$  with  $120 < p_T < 170 \text{ GeV}/c$  sample shown for comparison with the signal samples.

### 6.1.4 ECAL Time

The presence of spikes, noisy crystals and pile-up events, demand a robust method for measuring the photon arrival time at ECAL and since ECAL time is our main observable for distinguishing background from signal events, such a method must be capable of reducing timing bias which may arise from such anomalous events. As a result, we studied different methods for measuring the photon arrival time at ECAL.

The electromagnetic shower of an electromagnetic particle spreads across several crystals (energy and time measurements from several channels) belonging to the particle's supercluster containing all of the particle's energy. Using the supercluster, the arrival time of an electromagnetic particle can be defined using either the reconstructed time ( $t_{reco}$ ) of a single crystal, the *seed crystal* (crystal with the highest energy deposit), or a weighted average time calculated using the reconstructed time and its uncertainty of each crystal of the supercluster. We write,  $t_{seed}$ , for the seed time and,  $t_{Ave}$ , for the average time defined as

$$t_{Ave} = \frac{\sum_{i=1}^N \frac{t_{reco}^i}{\sigma_i^2}}{\sum_{i=1}^N \frac{1}{\sigma_i^2}}, \quad (6.4)$$

where  $N$  is the total number of crystals of the supercluster,  $t_{reco,i}$  and  $\sigma_i$  are the time and uncertainty on the reconstructed time of each channel, respectively. Figure 6.2 shows a comparison of a photon time measured as the seed time,  $t_{seed}$ , and as the average time,  $t_{Ave}$ . Both distributions have been normalized to total number of events.

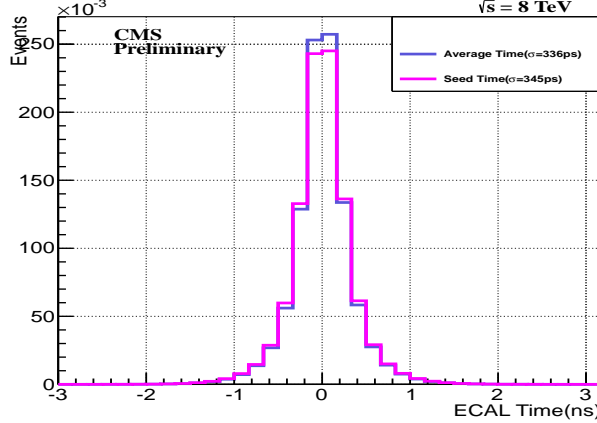


Figure 6.2: Measuring the photon time using either seed time (black) or average time (blue).  $\sigma$  of the Gaussian fit from seed time slightly better average time which is computationally intensive.

The width ( $\sigma$ ) of both Gaussian distributions are similar. We observed  $\sigma = 345$  ps for the seed time compared to  $\sigma = 336$  ps for the average time distributions.

In this analysis, we used the seed time for the photon ECAL time. However we also used the  $\chi^2$  on the photon ECAL time computed using the average time for identifying electromagnetic particles with bad timing. For example, when one or more of the crystals in a supercluster is poorly time calibrated or embedded with a spike, the photon time from the weighted average time measurement can be very biased which is a good reason to reject such a supercluster.

The  $\chi^2$  on the photon ECAL time calculated as

$$\chi^2 = \sum_{i=0}^N \frac{(t_{reco}^i - t_{Ave})^2}{\sigma_i^2} \quad (6.5)$$

where,  $N$  is the number of crystals in the photon supercluster,  $t_{reco}^i$  and  $\sigma_i$  are the time and uncertainty on the reconstructed time for each crystal and  $t_{Ave}$  is the mean time defined in Equation 6.4, is a reliable quantity to legitimized the photon time and to distinguish fake photons (jets misidentified as photons) and spikes from true photons. Figure 6.3 shows the profile of the pulse shape (left) of an identified spike with that of a

true photon. A distribution of the normalized  $\chi^2$  against the ECAL time is also shown in the right plot of the same figure. Photons with a signal pulse shape profile as that of spikes are associated with large values of  $\chi^2$  and usually have negative ECAL time.

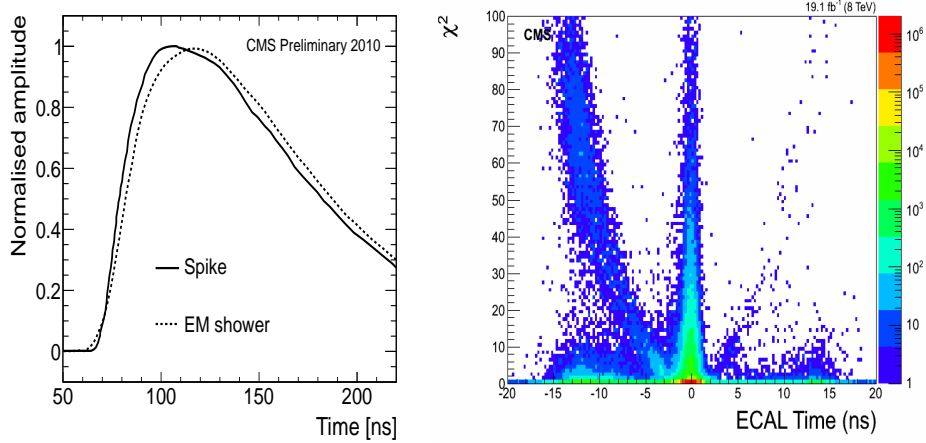


Figure 6.3: Pulse shape profile(left) showing a spike (solid line) and a true EM shower (dashed line) from data. The  $\chi^2$  against ECAL time distribution(right) shows spikes misidentified as photons with very large  $\chi^2$  and negative ECAL time. The region of  $\chi^2 > 4$  is mostly dominated by spikes events.

From the  $\chi^2$  Vs ECAL time plot (right plot of Figure 6.3), we observe that most of the photons have ECAL time around zero but also many of the photons with large ECAL time have large normalized  $\chi^2$  values which is expected where the time measurements by non-seeded crystals is inconsistent with the time measurement of the seed crystal. We also observed that, a cut in  $\chi^2 < 4$ , can reduce with 99.2% efficiency, photon contributions from spikes and misidentified jets where a neutron embedded in the jet hitting directly the photo-detectors produces a spike.

### Simulated ECAL Time

It is challenging to properly simulate ECAL time for MC events so that it captures the conditions of the ECAL detector during data recording. As a result, the time from MC events does not entirely represent the status of ECAL time in data, in terms of mean time and time resolution. We extract the adjustments for MC event time needed to match the mean time and timing resolution of data using a MC  $\gamma$ +jet samples of selected 1

or 2-jets events. Only events with isolated in-time,  $t_\gamma < 2$  ns, with  $p_T > 80$  GeV are selected. We perform the adjustment by shifting the mean time and smearing the timing resolution by an additional Gaussian convolution on the photon time of MC events so as to match the mean time and time resolution of data. The photon ECAL time from data and MC  $\gamma$ +jet samples both shown in Figure 6.4; where we compare before (left plot) and after (right plot) the adjustment on MC ECAL time was made, agree quite well.

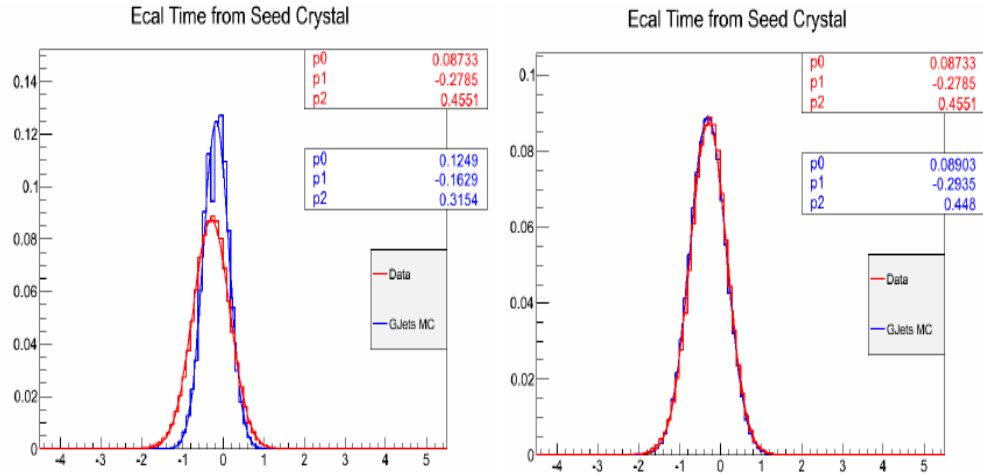


Figure 6.4: ECAL time distributions of in-time photons from MC  $\gamma$ + jets (blue) and data (red) samples before (left) and after (right) we adjusted the photon time from MC.

### Neutralino Measured Lifetime

The distance traveled, in the CMS detector, by the  $\tilde{\chi}_1^0$  before it decays, mentioned previously section 2.3.2, is given as

$$L = \left( c\tau_{\tilde{\chi}_1^0} \right) \cdot (\gamma\beta) = \left( c\tau_{\tilde{\chi}_1^0} \right) \cdot \left( \frac{p}{m_{\tilde{\chi}_1^0}} \right). \quad (6.6)$$

This distance depends on the momentum ( $p$ ) and mean lifetime ( $c\tau_{\tilde{\chi}_1^0}$ ) of the  $\tilde{\chi}_1^0$ . Large values of  $c\tau_{\tilde{\chi}_1^0}$  means, this distance is large and if larger than the ECAL radius, can be interpreted as the  $\tilde{\chi}_1^0$  traveled outside the ECAL volume before it decayed, making detecting the delayed photon no longer possible. On the other hand, small values of

$c\tau_{\tilde{\chi}_1^0} < 10$  cm means the  $\tilde{\chi}_1^0$  decayed early and the photon is not late enough such that its detection using ECAL time measurements alone is not reliable. High- $p$  values means the  $\tilde{\chi}_1^0$  is boosted and could travel out of the ECAL before it decay, making the photon again undetectable. On the other hand, low- $p$  values means the  $\tilde{\chi}_1^0$  is less boosted and traveling slow enough for its decay to happen inside the ECAL volume and the photon delayed arriving at ECAL. In Figure 6.5, we show a distribution of the momentum of the  $\tilde{\chi}_1^0$  in the transverse ( $x - y$ ) plane (transverse momentum ( $p_T^{\tilde{\chi}_1^0}$ )), the  $\tilde{\chi}_1^0$  transverse distance traveled before it decay, the transverse momentum of the photon ( $p_T^\gamma$ ) and photon's estimated time ( $T_\gamma$ ) using only generator level information. These distributions are for different  $\Lambda$  and  $c\tau_{\tilde{\chi}_1^0}$  points of the SPS8 model. We observed that, the  $p_T^{\tilde{\chi}_1^0}$  increases with increase values of  $\Lambda$ , from  $\Lambda = 100$  TeV to 220 TeV, which agrees with our expectation. As  $\Lambda$  increases along with the masses of the gluino/squark and  $\tilde{\chi}_1^0$ , the  $p_T^{\tilde{\chi}_1^0}$  also increases since a massive gluino/squark decay into the  $\tilde{\chi}_1^0$ . In the same way, increasing the mass of  $\tilde{\chi}_1^0$  ( $m_{\tilde{\chi}_1^0}$ ) through increasing  $\Lambda$ , leads to increase in the photon  $p_T$ . For a given value of  $\Lambda = 180$  TeV, which means  $p_T^{\tilde{\chi}_1^0}$  is fixed, the transverse distance traveled by the  $\tilde{\chi}_1^0$  before decay (shown in the top right plot of Figure 6.5) and photon time (shown in the bottom right plot of the same figure) increased with increasing value of  $\tilde{\chi}_1^0$  mean lifetime,  $c\tau = 50$  cm to 600 cm in the same way, qualitatively. These observations support our expectation that the photon is delayed primarily because of the long lifetime of the  $\tilde{\chi}_1^0$ . However, one can argue that this is not entirely true and we will exploit this further in a detailed study of the source of delayed photons in the next section.

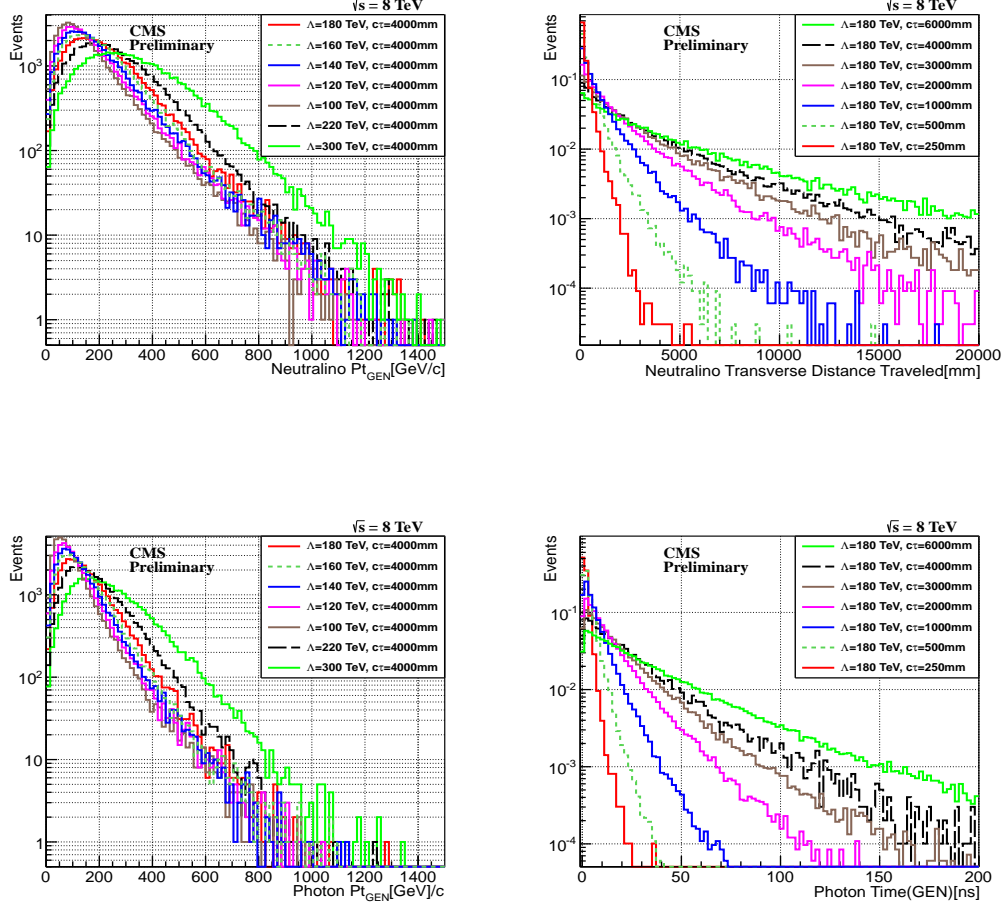


Figure 6.5: Neutralino transverse momentum ( $p_T^{\tilde{\chi}_1^0}$ ) distribution (top left) and transverse distance traveled (top right). Transverse momentum (bottom left) and time (bottom right) of photon from neutralino decay for different  $\Lambda$  and  $c\tau$  points in GMSB SPS8 model.

### Source of Delayed Photons

The photon from the decay of  $\tilde{\chi}_1^0$  can arrive late at ECAL for either one of the following reasons: first, because the  $\tilde{\chi}_1^0$  is traveling slow i.e. with boost,  $\beta = \frac{p_{\tilde{\chi}_1^0}}{m_{\tilde{\chi}_1^0}} \ll 1$ , and second, because the  $\tilde{\chi}_1^0$  was produced with significant boost such that the photon traveled to ECAL through a non-direct flight path from the nominal  $pp$  interaction point. We distinguish between these two sources of delayed photons by estimating the photon

arrival time at ECAL in each scenario using the distance traveled by  $\tilde{\chi}_1^0$  before decay and the distance traveled by the photon from the decay point to the point of detection at ECAL. Figure 6.6 (left) is a schematic representation showing how we estimate the photon arrival time at ECAL in each of the possible travel flight path representing the different source of delayed photons. The estimated photon arrival ECAL time in each scenario is given as follows:

- For slow moving neutralinos:  $\Delta t_1 = (L1/c\beta) - (L1/c)$
- For non-direct traveled flight path:  $\Delta t_2 = (L1 + L2 - L3)/c$
- ECAL measured time =  $\Delta t_1 + \Delta t_2$

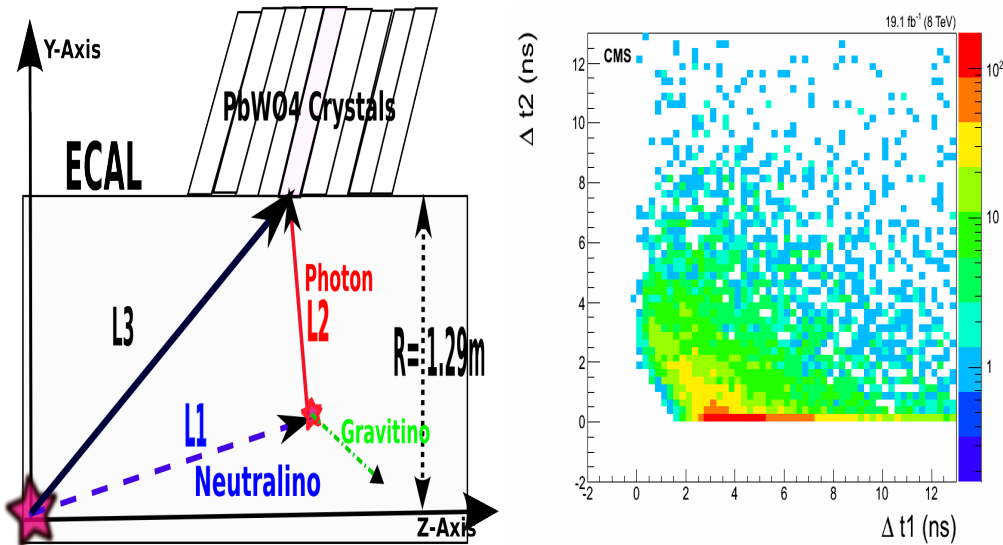


Figure 6.6: Schematic diagram showing  $\tilde{\chi}_1^0 \rightarrow \gamma + \tilde{G}$  decay topology within the ECAL volume of the CMS detector (Left). The estimated photon arrival time at ECAL from the decay of  $\tilde{\chi}_1^0$  in the SPS8 model with  $m_{\tilde{\chi}_1^0} = 256 \text{ GeV}/c^2$  and  $c\tau = 600 \text{ cm}$  (Right).

The  $\tilde{\chi}_1^0$  is traveling with velocity,  $v = c\beta$ , where  $c$  is the speed of light in vacuum. The distribution of the estimated photon ECAL arrival times  $\Delta t_1$  and  $\Delta t_2$ , is plotted shown in Figure 6.6(right), where the color intensity represents the photon population. We observed that most of the late arrival time photons are from the decay of slow moving  $\tilde{\chi}_1^0$  compared to those from non-direct flight path to ECAL. This proves that a good

number of  $\tilde{\chi}_1^0$  produced with low momentum such that the ratio  $\frac{p_{\tilde{\chi}_1^0}}{m_{\tilde{\chi}_1^0}} \ll 1$  produced most of our detectable delayed photons, using ECAL time measurements. While  $\tilde{\chi}_1^0$  with very long lifetimes ( $c\tau$ ) produced with high momentum will very likely escape the ECAL without detection unless their decay happens within the ECAL volume such that the delayed photon arrives at the ECAL in a non-direct flight path.

### Satellite Bunch Time

We observed (see Figure 6.7) a 2.5 ns discrete pattern in the photon ECAL time of events, produced in  $pp$  collisions, with photon  $p_T > 50 \text{ GeV}/c$  and belonging to the barrel and endcaps.

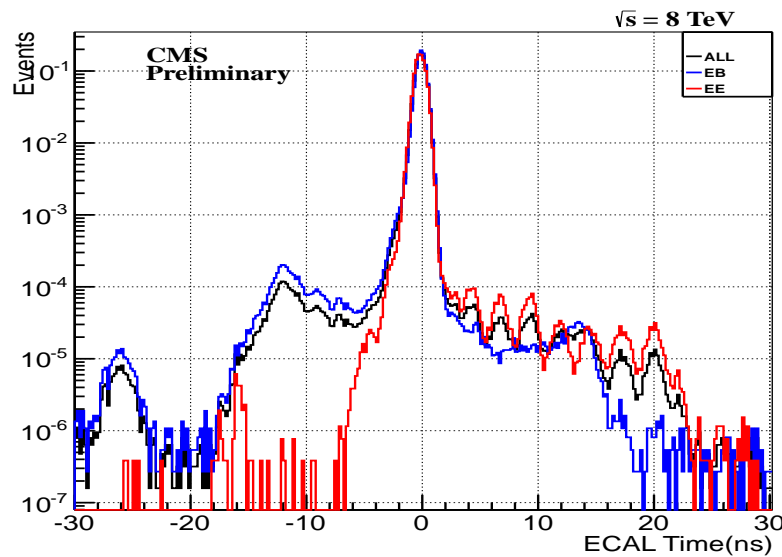


Figure 6.7: ECAL timing distribution of photons in barrel (EB), endcap (EE) and all of ECAL (ALL ECAL) with  $p_T > 50 \text{ GeV}$  from data. A 2.5 ns delay timing structure is observed in endcaps.

Most of the photons with this signature belong to the endcap ( $1.47 < \eta < 3.0$ ) and the rest in the barrel ( $|\eta| < 1.47$ ). Photons with this signature are produced from collisions of protons in *Ghost/Satellite* bunches, described in section 3.1.4, with either the main proton bunch or other *Ghost/Satellite* bunches. These events are considered

background events to our delayed photon signal because they produced photons from collisions with large ECAL time. It is challenging to reject these background events. We estimate their contribution using the ratio of the number of protons in ghost to main proton bunches taken from the proton population in the RF cavity of the LHC proton filling profile. From this ratio, we conclude that one in every 100,000 photons from  $pp$  collisions, observed in ECAL particularly the endcaps, is from ghosts bunch collisions. Their limited presence in the barrel is because very few of these photons are produced with high enough transverse momentum,  $p_T$ , to travel to the barrel and survive the  $50\text{ GeV}/c$  requirement.

Our observation of this phenomenon together with the sub-par ECAL time resolution in the endcaps compared to the barrel, means, this analysis only uses photons belonging to the barrel.

We estimate, the contribution of these events to our delayed photon background in the signal using an control sample of events with electromagnetic particles of moderate  $p_T$  range in the barrel like events with  $Z \rightarrow e^+e^-$  decay. The details of this study and the results obtained is discussed in the collision background estimation section of this analysis.

### $E_T^{\text{miss}}$ Adjustments

During energy clustering in the formation of superclusters used for event reconstruction by the particle flow (PF) algorithm, “out-of-time” energy deposits in ECAL are excluded. The reason is because the algorithm avoids energy deposits from particles not produced from the main proton-proton bunch collisions like cosmic muons and machine induced backgrounds which are normally out-of-time. As a result of the exclusion, the out-of-time photon  $E_T$  is not included in the calculation of missing transverse energy or  $\cancel{E}_T$  (from now on, we will be using for convenience,  $\cancel{E}_T$  instead of  $E_T^{\text{miss}}$  as the symbol for missing transverse energy) of the event. This exclusion introduces some differences in the calculation of  $\cancel{E}_T$  for in-time ( $|t_\gamma| < 3.0\text{ ns}$ ) and out-of-time photon events.

Because energy deposits from events with out-of-time photons could be from a possible signal event, and we are searching for events with large arrival time photons, we correct for this exclusion by adding back the out-of-time photon’s  $E_T$  vector to the particle flow reconstructed  $\cancel{E}_T$  (PF-MET) vector for events with out of time photons. We introduced

an additional missing transverse energy variable defined as  $\vec{E}_T^{\gamma} = \vec{E}_T + \vec{E}_T$ , and use it in our final event selection to avoid any bias in our event selection, particularly for events with out-of-time photons.

## 6.2 Event Selection

Our event selection happens in two stages. The first stage is online at the HLT trigger level where only triggered single photon events are selected and the second stage happens offline where the full signal event selection requirement is applied.

The full event selection criteria offline is designed to select signal events with event topology comprising of at least a single photon, multiple jets and large  $E_T$ . The cascade decay of gluino or squark to other quarks/gluons along with the  $\tilde{\chi}_1^0$ , is the reason for the multiple jets requirement and the at least a single photon and large  $E_T$  requirement is if at least one of the pair of  $\tilde{\chi}_1^0$  decay to a photon and gravitino. The large  $E_T$  requirement is useful for eliminating  $\gamma+$ jets and QCD events whose  $E_T$  is *fake*  $E_T$ , present because of poor energy reconstruction while the multijets requirement helps to reduce background events not produced from nominal  $pp$  collisions like cosmic muons, beam halo muons and spikes, which usually produce out-of-time photons. The multiple jets requirement also helps to reduce ElectroWeak (EWK) background events from  $pp$  collisions which are events with the decay of  $W \rightarrow e + \nu$  and  $t\bar{t}$ , where the top ( $t$ ) decays to a  $b$  quark and a  $W$  100% of the time. These events can produce fake photons (misidentified electron as a photon) and real  $E_T$  arising from the presence of the neutrino ( $\nu$ ). However, the high- $p_T$  photon requirement in our photon selection certainly reduce the contribution from EWK background events.

In order to reduce another source of collision background events which are events with fake photons from multijets and QCD events, where a jet is misidentified as a photon, we require high- $p_T$  jets of very good quality since jets from multijet QCD events are not of very good quality as a lot of other particles like electrons or muons can be found embedded in these jets.

An important part of our photon selection requirement is that we accept only photons in the barrel ( $|\eta_\gamma| < 1.479$ ) region of ECAL in order to reduce out-of-time photon background contribution from ghost/satellite bunch collisions. Another out-of-time photon

background source is from events with spikes, we reject some of these events at the HLT trigger level using electromagnetic shower shape related quantities like  $S_{Minor}$  and  $S_{Major}$ .

### 6.2.1 Trigger Selection

In our online event selection, we select only events passing our online higher level trigger (HLT). The HLT trigger used for our event selection during  $pp$  collisions at  $\sqrt{S} = 8$  TeV for this analysis is `HLT_DisplacedPhoton65_CaloIdVL_IsoL_PFMET25`, which is seeded by level 1 trigger; `HLT_L1SingleEG12`. This trigger was developed primarily to study delayed photons and to avoid bias in the event selection towards any particular signal model, the trigger only requires that an accepted event contains at least a single photon with a  $p_T$  of at least  $65\text{ GeV}/c$  and  $\cancel{E}_T$  above  $25\text{ GeV}$ . The minor axis of the photon electromagnetic shower must not be spread across many crystals in  $\phi$  implemented as  $0.1 < S_{Minor} < 0.4$ . The trigger efficiency and turn-on (efficiency becomes nearly 100%) curve for selecting events with delayed photon candidates is studied for the photon  $p_T$  and event  $\cancel{E}_T$ . In order to avoid any correlation between the photon and  $\cancel{E}_T$ , the efficiency for each variable is studied separately using another trigger `HLT_Photon50_CaloIdVL_IsoL`. The photon candidates used in this photon efficiency study must pass our offline photon selection criteria shown in table 6.4. The HLT photon selection efficiency for  $p_T$  is defined as the fraction of offline reconstructed photons to those triggered by `HLT_IsoPhoton50` trigger within  $\Delta R < 0.5$ . Similarly, the  $\cancel{E}_T$  HLT efficiency is defined as the fraction of events containing at least a jet and  $\cancel{E}_T$  more than the HLT required  $\cancel{E}_T$  of  $25\text{ GeV}$ . The results of the trigger efficiency measurements are shown in Figure 6.8 against photon  $p_T$  and  $\cancel{E}_T$ . This HLT event selection efficiency study indicates that the event selection efficiency is 100% for events with photon  $p_T > 80\text{ GeV}/c$  and  $\cancel{E}_T > 60\text{ GeV}$ . These efficiency studies use the `HLT_Photon50_CaloIdVL_IsoL` trigger which has no  $\cancel{E}_T$  and jet multiplicity requirement for the denominator and the `HLT_DisplacedPhoton65_CaloIdVL_IsoL_PFMET25` for the numerator. A `SinglePhoton` data sample is used to verify these efficiency study while the GMSB SPS8 and  $\gamma + \text{jets}$  samples are used to derive any correction factors between data and MC events.

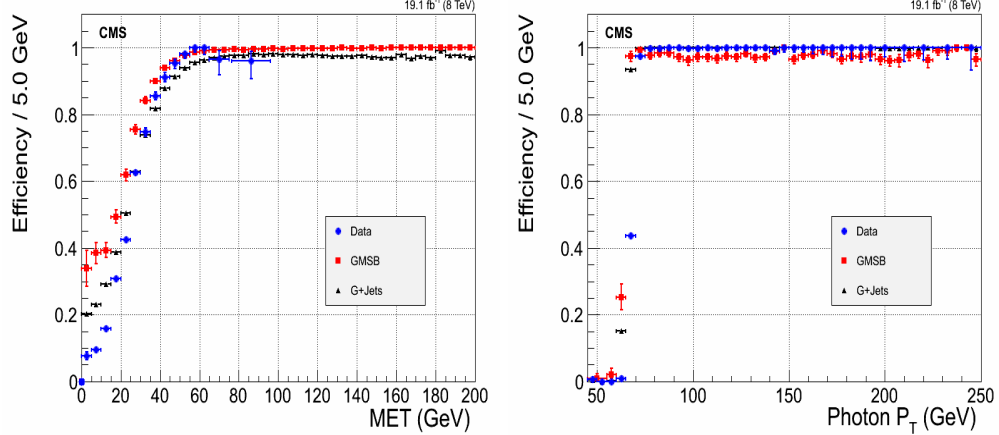


Figure 6.8: Our HLT trigger efficiency turn-on curves for photon  $p_T$  (right) and event  $\cancel{E}_T$  (left). The  $\gamma$ +jets samples require photon  $p_T > 170$  GeV/c.

### 6.2.2 Offline Selection

In addition to the HLT selection, we apply an offline event selection on the photon, jets and  $\cancel{E}_T$  of these events.

The leading photon of an event must have a  $p_T$  greater than 80 GeV/c and the sub-leading photon candidates of the same event must have  $p_T > 45$  GeV/c. Because the Particle Flow (PF) algorithm does not consider out-of-time isolated photon energy deposits, we do not use the PF photon isolation criteria but rather a *simple cut-based* isolation requirement where we request that there should be no tracks near the selected photon within a range in  $\Delta R(\gamma, \text{track}) < 0.6$ . Tracker, ECAL and HCAL isolation based on the photon  $p_T$  and  $E_T$ , must be within the accepted range required by the simple cut-based approach given in Table 6.4. The ratio of the photon energy deposit in HCAL to ECAL must be less than 5% to avoid misidentifying high fraction electromagnetic and neutral component jets as photons and the photon shower shape along the minor axis ( $S_{\text{Minor}}$ ) must be within 0.12 and 0.38 to avoid selecting spikes as photons. To prevent double counting jets with high electromagnetic energy component as photons with other photons, the photon must be isolated from any other particle in a cone size of  $\Delta R(\gamma, \text{Other particle}) < 0.4$ . We only selected photons belonging to the barrel (EB) region i.e.  $|\eta_\gamma| < 1.479$  since we observed many out-of-time photon candidates from ghost/satellite bunch collisions belong to the endcap (EE) shown in Figure 6.7 of a

photon ECAL time comparison between photon candidates belonging to EB and EE. Our photon selection requirement is summarized in Table 6.4.

For jets, we select jets reconstructed with the PF algorithm based on the CMS standard good quality jet identification selection criteria presented in Table 6.5. We require the leading jet in the event to have a  $p_T$  of at least 35 GeV/c.

As for Missing Transverse Energy (MET) selection requirement, with inspiration from our trigger event selection efficiency plot in MET in Figure 6.8, we observed that a missing energy of at least 60 GeV for  $\cancel{E}_T$  and  $\cancel{E}_T^{\gamma}$  is enough to suppress  $\gamma$ +jets and QCD events with fake missing transverse energy.

<b>Photon Selection Criteria</b>	
<b>Criteria</b>	<b>Requirement</b>
Event leading photon must have $p_T(\gamma^1)$	$> 80$ GeV
Other photons in event must have $p_T(\gamma^{2,3,\dots})$	$> 45$ GeV
$ \eta_\gamma $ , (Barrel Only),	$< 3.0$ ( $< 1.5$ )
$S_{Minor}$	$0.12 \leq S_{Minor} \leq 0.38$
$H/E$	$< 0.05$
$\Delta R(\gamma, track)$	$> 0.6$
HCAL Iso, ECAL Iso, Track Iso	$< 4.0, < 4.5, < 0.2$
Photon Isolation cone size $\Delta R(\gamma, Other\ particle)$	$< 0.4$
Topological Spike cuts	$1 - E_6/E_2 < 0.98, 1 - E_4/E_1 < 0.98$

Table 6.4: The photon identification and selection criteria used in this analysis

Jet PF identification selection criteria	
Criteria	Requirement
Jet $p_T$	$> 35 \text{ GeV}$
Number of Jet constituents	$> 1$
Charge EM energy fraction (CEF)	$> 0.99$
Neutral Hadron energy fraction (NHF)	$< 0.99$
Neutral EM energy fraction (NEF)	$< 0.99$
If $ \eta $ of jet is $> 2.4$ , Charge Hadron energy fraction (CHF)	$> 0$
If $ \eta $ of jet is $> 2.4$ , Charge multiplicity (NCH)	$> 0$
$\Delta R(\gamma, \text{jet}) = \sqrt{(\phi_\gamma - \phi_{\text{jet}})^2 + (\eta_\gamma - \eta_{\text{jet}})^2}$	$> 0.3$
$E_T$ , $\cancel{E}_T$	$> 60 \text{ GeV}$

Table 6.5: The Jet ID and MET selection used in this analysis

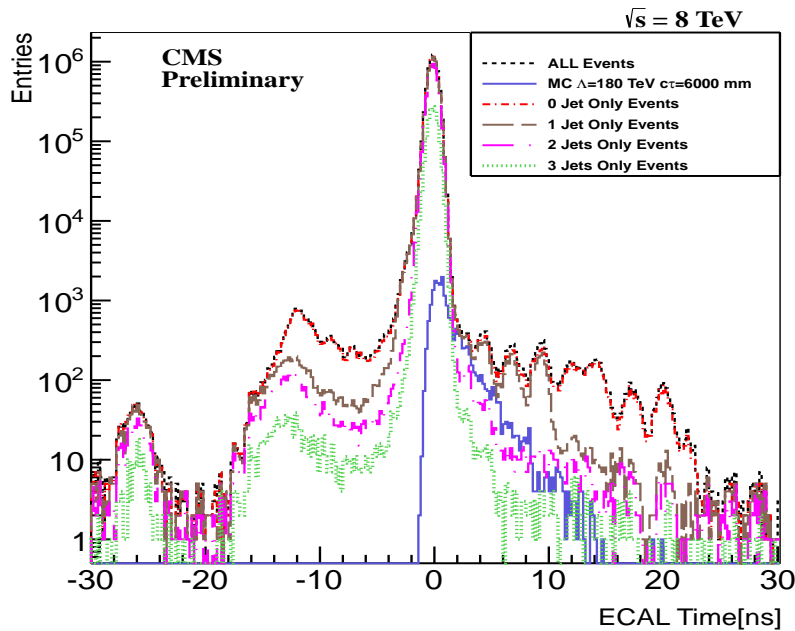


Figure 6.9: Comparing ECAL time distribution of events with different jet multiplicity from small sample of data and a single GMSB  $\Lambda = 180 \text{ TeV}$  and  $c\tau = 6000 \text{ mm}$  sample. Accepted photons must have  $p_T > 60 \text{ GeV}$ .

In summary, our signal events should have event topology comprise of  $\geq 1 \gamma + \geq 2 \text{ jets} + \cancel{E}_T > 60 \text{ GeV} + \cancel{E}_T^{\gamma} > 60 \text{ GeV}$  and we use a control sample made of events with zero and one jet background study since these events dominate our background sample shown in Figure 6.9.

### 6.3 Background Estimation

Most of our background events with out-of-time photons are non-collision events produced from many different sources. In order to qualify and quantify the different sources, we compare in-time ( $|t_\gamma| < 1 \text{ ns}$ ) photon candidates to out-of-time ( $t_\gamma < -3 \text{ ns}$  and  $t_\gamma > 2 \text{ ns}$ ) photon candidates. By also comparing photon candidates of events with different number of jets, we were able to uncover the different background sources and better quantify their contribution. In Figure 6.10, we present scatter plots of the photon's ECAL time against  $\eta$  (left) and against  $\phi$  (right) for events with photon  $p_T < 60 \text{ GeV}$ , belonging to both the barrel and endcap regions and event  $\cancel{E}_T > 25 \text{ GeV}$ .

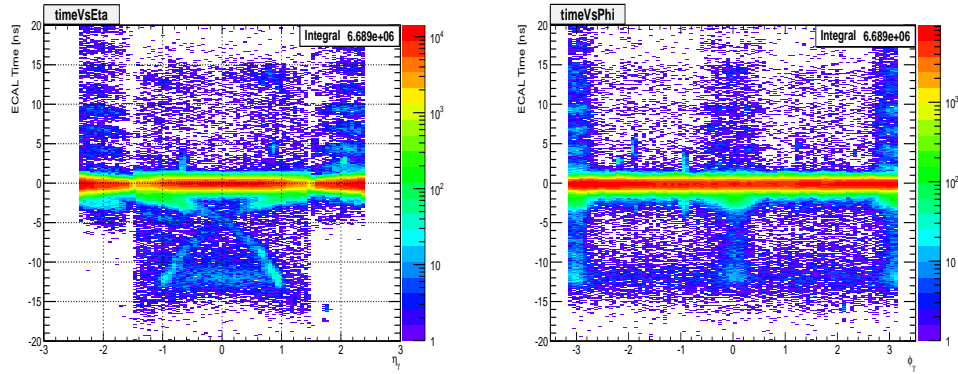


Figure 6.10: ECAL time against  $\eta$  (left) and ECAL time against  $\phi$  (right) for photons with  $p_T > 60 \text{ GeV}$  from data.

From these plots, we observe that, although most of the photons arrive with ECAL time about zero, a good number of photons are out-of-time and from very different sources, for example, the cross-like feature seen in the plot on the left, is particular to photons with earlier ECAL time while the step-like pattern in ECAL time extends to all out-of-time photons but is more prominent to photons which belong to the endcap

regions ( $1.479 < \eta_\gamma < 3$ ) and have late ECAL time. The high concentration of out-of-time photons at  $\phi = 0 \pm \pi$  on the right plot indicate a unique source of non-collision events which is not random. We conclude that the possible sources of background photon candidates with out-of-time can be split into photons from beam halo muons, because of the cross-like feature and high population at  $\pi = 0 \pm \pi$ , cosmic muons, due to the random distribution of out-of-time photons throughout ECAL and spikes, due to the high concentration of photons with ECAL time of about -12.5 ns. The step-like feature can be attributed to photons arising from ghost/satellite bunch collisions while a small contribution of out-of-time photons is from QCD and electroweak events. To reduce the contamination of possible signal out-of-time photons from spikes which contribute the most to events with out-of-time photons particularly with ECAL time around  $t_\gamma \approx -12$  ns, we restrict our event selection to photons with ECAL time  $2.0 < t_\gamma < 13.0$  ns and  $-10.0 < t_\gamma < -3$  ns, making our search restricted to signal events with photon ECAL time between  $2.0 < t_\gamma < 13.0$  ns.

For our background estimation study, we split the background events into two categories: Collision and Non-Collision events. We first identify and reject photon candidates from beam halo, cosmic muons and spikes and then estimate the residual non-collision and collision background photon candidates using the **ABCD** background estimation technique.

### 6.3.1 Collision Background

#### QCD Photons

Events from satellite/ghost proton bunches described in section 3.1.4, produce out-of-time photons which can be present in the barrel. Because these photons are produced from collisions just like QCD events, we refer to these photons as QCD photons. It is challenging to define a strategy for rejecting this background events. Our approach, after rejecting non-collsion events, is to estimate their contribution to signal using the ABCD background estimation method. We also perform a separate background estimation using a control sample of Z events, and show that background contributions from events with QCD photon candidates from satellite/ghost is almost negligible.

### 6.3.2 Non-Collision Background

#### Halo Photons

Protons in the main and sometimes ghost/satellite bunches can, through inelastic scattering with residual gas molecules like H<sub>2</sub> and CO<sub>2</sub> in beam pipe, produce pions which later decay into muons called *Beam Halo* muons, traveling with energy of about a few TeV. These energetic muons radiate energetic photons called *Halo photons* in the calorimeter through a process called *bremsstrahlung*. It is also possible that beam halo muons can be produced when protons scatter off Tertiary Collimators (TCT), due to proton beam deflection by the magnets, just before entering the CMS detector. The halo muons can travel nearly parallel to the main proton bunch but often stir away from the nominal orbit in the transverse direction spreading mostly in the horizontal plane, with respect to the CMS detector coordinates, due to betatron oscillations. Despite beam cleaning, a sizable population of beam halo muons remains eventually producing energetic photons in the calorimeters. A scatter plot of the photon ECAL time against  $\phi$  shown earlier in the right plot of Figure 6.10, show that most of these beam halo muons enter the ECAL in the horizontal plane at  $\phi = 0, \pm\pi$ . The rate of halo photons in the general proton *Beam-Induced Background* (BIB) events depend on the beam current and the operational conditions of the LHC like the machine optics, collimator settings, residual gas densities and RF cavity filling scheme.

The halo muons before entry into ECAL, produce hits which can be reconstructed into muon tracks using segments in the Cathode Strip Chambers (CSC) Endcap muon detectors. The reconstructed hits in the CSC segments can be associated with a halo photon supercluster in ECAL within some narrow opening angle in  $\phi$ . The geometry of ECAL allows most of the halo muons in the endcaps but also enough in the barrel. The resulting halo photons are usually out-of-time compared to photons produced directly from nominal  $pp$  collisions and most of them have earlier arrival time in cases where the beam halo muons arrive at the ECAL crystals before  $pp$  collisions occur at the interaction point. This arrival time can be estimated from the unique flight path of the beam halo muons with respect to the arrival time of photons from  $pp$  collisions as

$$t_{\text{ECAL}}^{\text{expected}} = -1/c \left( \pm Z_{\text{cluster}} + \sqrt{Z_{\text{cluster}}^2 + R_{\text{cluster}}^2} \right), \quad (6.7)$$

where  $Z_{\text{cluster}}$  is the point where the halo muon hits ECAL or longitudinal distance along  $z$ -axis of the halo photon supercluster position from the nominal interaction point,  $R$  is the radial distance of the supercluster from the beam line which is the radius of ECAL equal to 1.29 m and  $c$  is the speed of light in vacuum. The estimated halo muon ECAL arrival time can be re-arrange to become

$$t_{\text{ECAL}}^{\text{expected}} = -\frac{R}{2c} \exp^{(-\eta)} \quad (6.8)$$

showing the explicit dependence on  $\eta$ , for the beam halo muon entry point in ECAL. Comparing this estimated time shown in Figure 6.11 as the two red lines, with observation from data for the 2-dimensional plot of ECAL time *vs*  $\eta$  of photon candidates, show a nice agreement especially for earlier arrival time photon candidates.

By matching halo muon hit positions in CSC segments to photon supercluster positions in the ECAL calorimeter in  $\phi$ , since halo muons spread mostly in the horizontal plane or azimuthal ( $\phi$ ) direction, we are able to match halo muons to their corresponding halo photons. We use the quantity,  $\Delta\phi(\text{CSC Seg}, \gamma)$ , which is the difference in  $\phi$  between the CSC segment and the photon supercluster position in ECAL, to express this matching. A plot of  $\Delta\phi(\text{CSC Seg}, \gamma)$  for in-time and out-of-time photons is shown in the left plot of Figure 6.11. We see that out-of-time photons have small  $\Delta\phi(\text{CSC Seg}, \gamma)$  confirming that some out-of-time photons are produced by beam halo muons.

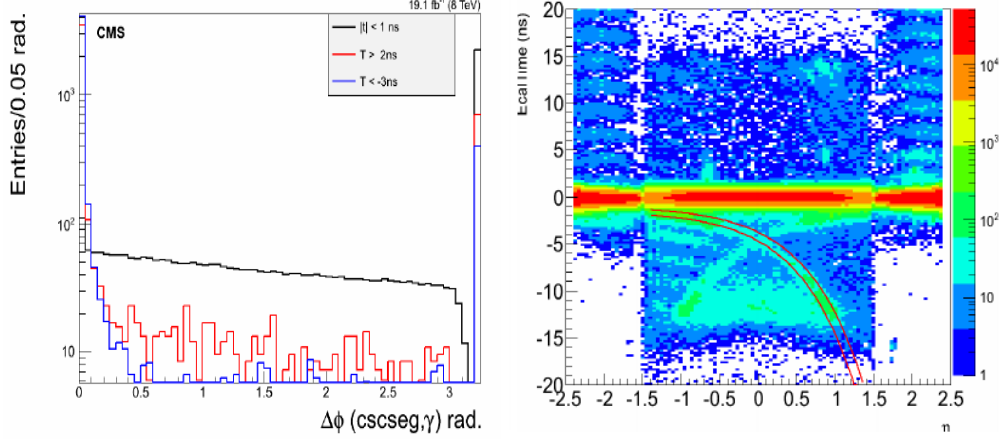


Figure 6.11: (Left) ECAL time  $V.s$   $\Delta\phi(\text{CSC Seg}, \gamma)$  for in time(black) and out-of-time(red and blue) photons. (Right)Photon ECAL time  $V.s$   $\eta$ , expected halo photon time is shown as two red lines.

To estimate the performance of using  $\Delta\phi(\text{CSC Seg}, \gamma)$  for tagging events with halo photons, we use a halo photon candidate sample of selected events with photons in the endcaps where we expect mostly halo photon candidates and with  $\phi_\gamma$  around  $\phi = 0, \pm\pi$ . We were able to tag with  $\Delta\phi(\text{CSC Seg}, \gamma) < 0.05$ , a good number of photon candidates as halo photons in the endcaps shown in the Figure 6.12 comparing halo photons in the endcaps to tagged halo photons in the endcaps.

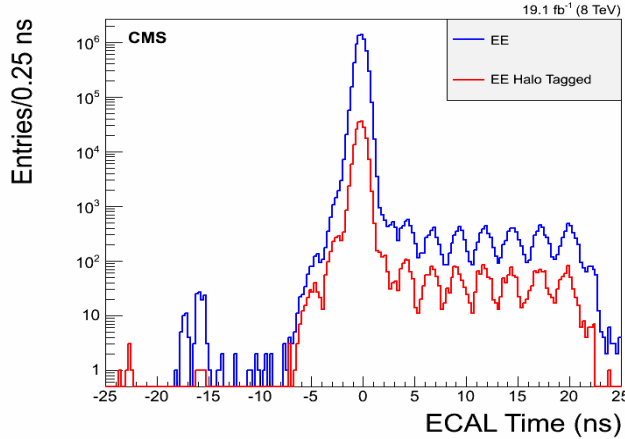


Figure 6.12: Using  $\Delta\phi(\text{CSC Seg}, \gamma) < 0.05$  to tag photons with  $\phi_\gamma = 0, \pm\pi$  in the endcaps. A good portion of endcap photon candidates are tagged.

## Cosmic Photons

Cosmic muons produced in cosmic rays, like beam halo muons, with sufficient energy will radiate (bremsstrahlung) photons in ECAL. We refer to these photons as *Cosmic Photons*. Unlike halo muons, cosmic muons can arrive at ECAL from any direction at any time. We expect cosmic photons in the barrel produced from cosmic muons, to have hits in the Drift Tubes (DT) segments found in the muon barrel behind the calorimeters. Using DT segments and photon supercluster  $\eta - \phi$  position in ECAL, we can match cosmic muon hits in DT segments to ECAL photon superclusters within a narrow window in  $\Delta\eta$  and  $\Delta\phi$ . The DT position used in the calculation of  $\Delta\eta$  and  $\Delta\phi$  is a projection of the muon trajectory using the direction of the DT segment to the outer surface of ECAL because of the large space between the muon barrel and the ECAL. The two dimensional distribution for  $\Delta\eta(\text{DT Seg}, \gamma)$  and  $\Delta\phi(\text{DT Seg}, \gamma)$  of this matching, for events with out-of-time photons;  $t_\gamma > 2$  ns and  $t_\gamma < -3$  ns, is shown in the right plot of Figure 6.13. We compared to  $\Delta\eta(\text{DT Seg}, \gamma)$  and  $\Delta\phi(\text{DT Seg}, \gamma)$  distribution for in-time ( $|t_\gamma| < 1$  ns), shown in the left plot, still in the same figure, we observed that most out-of-time photons have a small  $\Delta\eta$  and  $\Delta\phi$ . Comparing the  $\Delta\eta$  and  $\Delta\phi$  2-dimensional distributions of these out-of-time photons to photons from a pure cosmic muons sample (data taken when no proton-proton collisions is happening), shown in Figure 6.14, we found a similar small  $\Delta\eta$  and  $\Delta\phi$  occupancy for the true cosmic muons sample. We conclude that small  $\Delta\eta(\text{DT Seg}, \gamma)$  and  $\Delta\phi(\text{DT Seg}, \gamma)$  can be used to tag and reject events with cosmic photons.

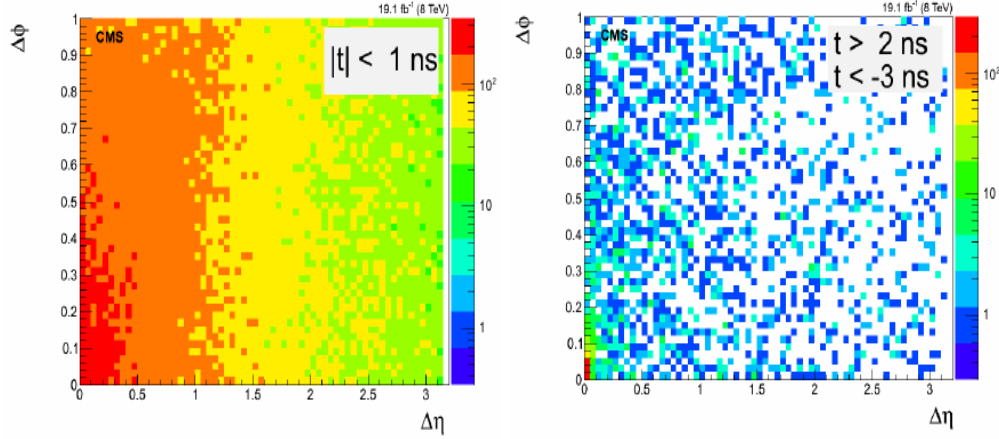


Figure 6.13: Scatter plot showing  $\Delta\eta(\text{DT Seg}, \gamma)$  against  $\Delta\phi(\text{DT Seg}, \gamma)$  for out-of-time ( $t_\gamma > 2$  ns and  $t_\gamma < -3$  ns) photons (right) compared to in-time ( $|t_\gamma| < 1$  ns) photons (left). Cosmic photon candidates have small  $\Delta\eta$  and  $\Delta\phi$ .

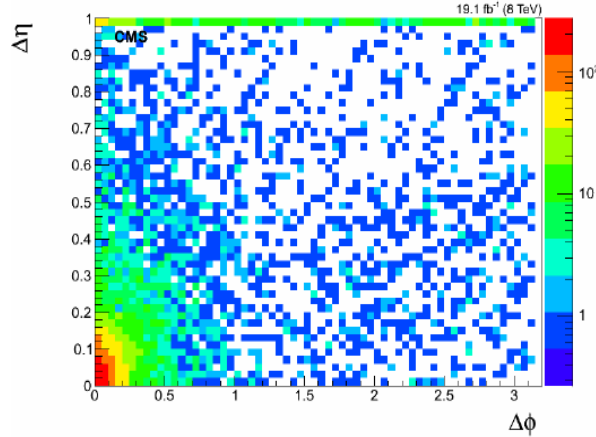


Figure 6.14: Scatter plot of  $\Delta\eta(\text{DT Seg}, \gamma)$  against  $\Delta\phi(\text{DT Seg}, \gamma)$  for photons from pure cosmic muon data. Small  $\Delta\eta$  and  $\Delta\phi$  are cosmic photons.

### Anomalous Photons: Spikes

Neutrons and charge hadrons can at times deposit their energy directly to the APDs instead of going through the crystal scintillation process. Such signals read from the APDs are *anomalous* and referred to as *spikes*. Spikes produced from  $pp$  collisions and satisfying photon selection requirement can easily be identified as photons. A spike supercluster consists of very few crystals; most often one or two crystals. Spikes can also overlap with real photons and found embedded in a real photon supercluster or

buried inside of jets. Such embedded spikes are challenging to identify. By looking at the signal pulse height, the pulse shape for a spike signal appear different from a signal form an electromagnetic particle. Because of this difference in pulse shape profile, the reconstructed ECAL time for spikes usually have large calculated  $\chi^2$  values.

The arrival time of spikes is much earlier (negative), usually about  $t \approx -12.0$  ns than for photons produced in nominal  $pp$  collisions depositing their energy in the APD through crystal scintillation. This is because of the absence of the scintillation process which takes on average 10 ns. The few crystals containing the spike cluster energy deposits make it possible for spikes to be identified using a energy topological selection quantity,  $1 - \frac{E_4}{E_1}$ , also know as *swiss-cross* variable. By looking at a distribution shown in right plot of Figure 6.15, of the swiss-cross for in-time and for events from a spike sample (events with photon with time  $t = -12$  ns), we observed that most spikes have about 98% of their energy deposited in a single crystal.

Using the number of crystals in a photon supercluster and comparing the number of crystals in in-time photons to halo photons and spike candidate photons (photons with  $1 - \frac{E_4}{E_1} > 0.98$ ) shown in the left plot of Figure 6.15, we observed that most spikes including spikes embedded in electromagnetic candidates have less than 7 crystals in their supercluster. A combination of the swiss-cross, number of crystals in supercluster, calculated  $\chi^2$  from ECAL time,  $S_{Major}$  and  $S_{Minor}$  (both  $S_{Major}$  and  $S_{Minor}$  describe the shape of the electromagnetic shower) is useful for identifying and rejecting events with spikes.

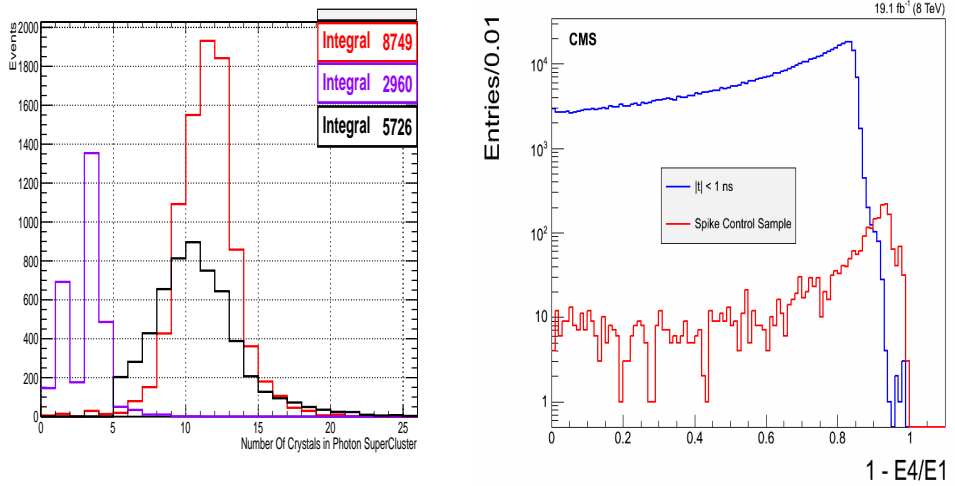


Figure 6.15: *Number of crystals* in photon supercluster plot (Left) for in-time photon candidates (black), spike photon candidates (magenta) and halo photon candidates (red). The spike photon candidates are selected with an energy swiss-cross variable ( $1 - E_4/E_1$ ) (right) shown comparing in-time photons ( $|t_\gamma| < 1.0$ ) to spike candidate sample selected with  $S_{\text{Minor}}$  and  $S_{\text{Major}}$  variables.

### 6.3.3 Event Vetoing, Performance and Fake Rates

Using the quantities studied for tagging events with halo, cosmic and spike photons, we tag and veto non-collision background events as follows:

- An event with a halo photon is tagged and vetoed if a CSC segment for  $|\eta| > 1.6$  is found within 0.05 radian of the azimuthal angle with the photon supercluster, i.e. a photon found within  $\Delta\phi(\text{CSC Seg}, \gamma) < 0.05$  is vetoed. We found that we are able to veto events with a halo photon with 91% efficiency and 3% mis-tag rate using this photon selection requirement.
- An event with cosmic photon is tagged and vetoed with 75.5% efficiency and 1.4% mis-tag rate if the photon can be matched to a DT segment within  $\Delta\eta(\text{DT Seg}, \gamma) < 0.1$  and  $\Delta\phi(\text{DT Seg}, \gamma) < 0.1$ .
- An event with spike is vetoed if the photon has ECAL time  $\chi^2 > 4$ , Number of crystals  $< 7$ ,  $1 - E_4/E_1 > 0.98$ ,  $S_{\text{Major}} < 0.6$  and  $S_{\text{Minor}} < 0.17$  with only 0.4% mis-tag rate.

Presented in Table 6.6, is a summary for the mis-tag rates of the different non-collision background sources.

Background Source	Fake Rate(%)
<i>Halo Photons</i>	$\approx 3$
<i>Cosmic Photons</i>	$\approx 1.4$
<i>Spikes</i>	$\approx 0.4$

Table 6.6: Fake rates for different non-collision vetoing.

The result of the event tagging is shown in Figure 6.16. We observe that the majority of non-collision background events are events with a halo photon. Very few late arrival time photons are produced from spikes. There is also some significant contribution from cosmic photons. The most interesting observation is the residual out-of-time background (in red) which could not be tagged.

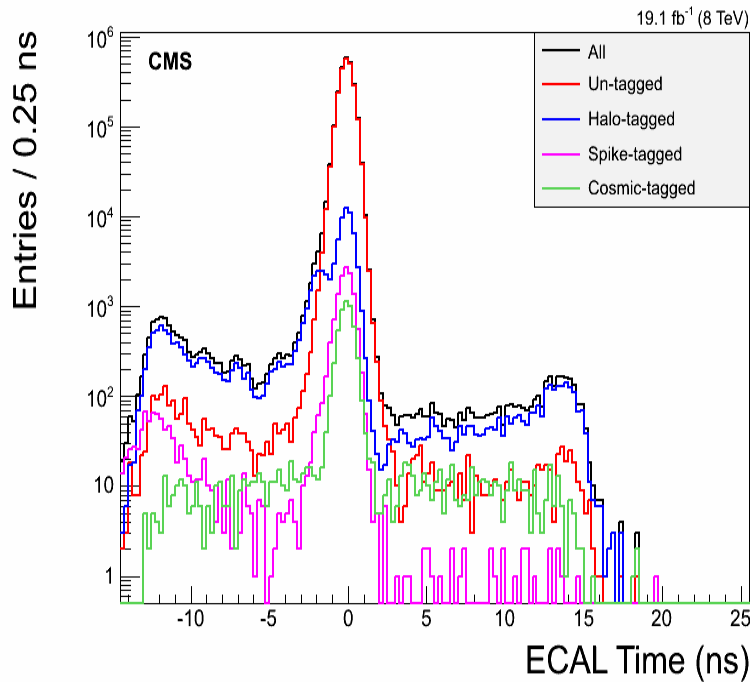


Figure 6.16: ECAL photon time for a data sample of 0 and 1-jet events showing our tagging performance for non-collision background events.

These residual untagged events comprise of some non-collision events, since the tagging and vetoing are not 100% efficient, events with QCD photons from ghost/satellite

collisions and events with  $W \rightarrow e\bar{\nu}_e$  decay with the fake photon passing the photon selection requirement. In order to quantify our estimates of these different sources contributing to the untagged background events, we use control samples defined with  $\cancel{E}_T^{\gamma}$  and  $\cancel{E}_T$ .

We expect signal events, because of the undetected gravitino from the neutralino decay, to have large  $\cancel{E}_T^{\gamma}$  and  $\cancel{E}_T$ , by large, we mean above 60 GeV, and events with  $W \rightarrow e\bar{\nu}_e$  decay to equally have large  $\cancel{E}_T^{\gamma}$  and  $\cancel{E}_T$  because of the undetected neutrino. The non-collision (cosmic, halo, spike) and collision (ghost/sattelite or QCD) background events can be categorized into high- $p_T$  and low- $p_T$  events. For high- $p_T$  non-collision events, we expect these events to have large  $\cancel{E}_T$ , due to the exclusion of the energy deposits from the out-of-time photons in the missing transverse energy reconstruction, and small  $\cancel{E}_T^{\gamma}$  when the large transverse energy contribution from the energy deposits of the out-of-time photons is re-introduced, while for low- $p_T$  non-collision events, we expect these events to have both  $\cancel{E}_T^{\gamma}$  and  $\cancel{E}_T$  small, since the out-of-time photon transverse energy, which was excluded, was in the first place small. For high- $p_T$  out-of-time collision events which usually have small missing transverse energy, we expect their  $\cancel{E}_T$  to be small and after re-introducing the energy deposits from out-of-time high- $p_T$  photons, we expect their  $\cancel{E}_T^{\gamma}$  to be large, while, using the same argument made for low- $p_T$  non-collision events, we expect low- $p_T$  collision events to have both small  $\cancel{E}_T^{\gamma}$  and  $\cancel{E}_T$ . A summary of our expectations for  $\cancel{E}_T^{\gamma}$  and  $\cancel{E}_T$  for the different expected background events sources with possible contribution to the residual untagged events with out-of-time photon is presented in Table 6.7.

Event Sample	$\cancel{E}_T$	$\cancel{E}_T^{\gamma}$
Signal Events	Large	Large
$W \rightarrow e\bar{\nu}_e$ Events	Large	Large
High- $p_T$ Non-Collision(Mostly Beam Halo) Events	Large	Small
Low- $p_T$ Non-Collision Events	Small	Small
High- $p_T$ Collision(QCD/Ghost) Events	Small	Large
Low- $p_T$ Collision Events	Small	Small

Table 6.7: Summary of missing transverse expectation for events with out-of-time photons.

Using control samples defined using  $\cancel{E}_T$  and  $\cancel{E}_T^\gamma$  for events with in-time ( $|t_\gamma| < 2.0$  ns) photons, events with photon time,  $t_\gamma > 3.0$  ns and  $t_\gamma < -3.0$  ns, where each control sample is defined purposely to enhance the contribution of either collision or non-collision background events to that control sample while simultaneously suppressing contributions from the other, we perform a background estimation in the signal control sample ( $t_\gamma > 3.0$  ns,  $\cancel{E}_T^\gamma > 60$  GeV and  $\cancel{E}_T > 60$  GeV) using the so-called ABCD background estimation method. We verify that the background estimation method is performing as expected using a data sample of zero and one jet events.

### 6.3.4 Background Estimation with ABDC Method

Since we expect most of our background events to come from non-collision events, we estimate the number of events we expect from non-collision events in the signal control sample using the ABCD technique. We also estimate the possible contamination, we expect from collision events, to the control samples used in the ABCD method.

#### 1. Non-Collision Background Estimation:

To estimate the number of background events from non-collision, we define Control Samples (CS), labeled as ABCD, in photon ECAL time and  $\cancel{E}_T^\gamma$  for selected events with  $\cancel{E}_T > 60$  GeV. Events with  $\cancel{E}_T > 60$  GeV define a CS where the contribution from collision (QCD) background events is suppressed, since most collision background events have small  $\cancel{E}_T$ , as we saw in Table 6.7. The control samples; A and B, shown in Table 6.8, are events with, respectively,  $\cancel{E}_T^\gamma < 60$  GeV and  $\cancel{E}_T^\gamma > 60$  GeV and photon ECAL time,  $-10.0 < t_\gamma < -3.0$  ns, and CS C have events with  $\cancel{E}_T^\gamma < 60$  GeV and photon ECAL time,  $3.0 < t_\gamma < 13.0$  ns.

Non-Collision	$\cancel{E}_T^\gamma < 60$ GeV	$\cancel{E}_T^\gamma > 60$ GeV
$3.0 < t_\gamma < 13.0$ ns.	C	D
$-10.0 < t_\gamma < -3.0$ ns	A	B

Table 6.8: ABCD Control Samples (CSs) definitions used for estimating non-collision background events in the signal CS D. Events must satisfy the  $\cancel{E}_T > 60$  GeV selection requirement.

Using these control samples for the ABCD method, and with the assumption that

$\frac{N_D}{N_C} = \frac{N_B}{N_A}$ , the number of non-collision background events with out-of-time photons expected in the signal CS D is given as

$$N_D^{non-col} = \left( \frac{N_B}{N_A} \right) \cdot N_C, \quad (6.9)$$

where  $N_B$ ,  $N_A$  and  $N_C$  are the number of events observed in B, A and C control samples in that order and  $N_D^{non-col}$  is the number of non-collision background events we expect in the signal CS D.

## 2. Collision Background Estimation:

We estimate the number of collision background events contaminating CSs defined in Table 6.8, by once again using the ABCD technique with the Control Samples (CSs) used defined in photon ECAL time and  $\cancel{E}_T$  for selected events with  $\cancel{E}_T^{\gamma} > 60 \text{ GeV}$ . We are interested in the contamination from collision background events to CS B and D of Table 6.8, since these are the CSs where we expect events with large missing transverse energy (see Table 6.7). Most collisions events have photons with in-time ( $|t_{\gamma}| < 2 \text{ ns}$ ), therefore, we use CSs defined with in-time photons to estimate the number of possible collision events with out-of-time photons contributing to CSs B and D. The CSs used for the new ABCD method to perform the collision background estimation are labeled as  $A'$   $B'$   $C'$   $D'$  and defined as shown in Table 6.9.

Collision	$\cancel{E}_T < 60 \text{ GeV}$	$\cancel{E}_T > 60 \text{ GeV}$
$3.0 < t_{\gamma} < 13.0 \text{ ns.}$	$C'$	$D'$
$-2.0 < t_{\gamma} < 2.0 \text{ ns}$	$I'$	$I$
$-10.0 < t_{\gamma} < -3.0 \text{ ns}$	$A'$	$B'$

Table 6.9:  $A'$   $B'$   $C'$   $D'$  and  $I$   $I'$  Control Samples (CSs) used for estimating collision background events contamination to CSs B and D. Events here must satisfy  $\cancel{E}_T^{\gamma} > 60 \text{ GeV}$  selection requirements.

The number of collisions events contributing to the CS B,  $N_B^{col}$ , is estimated as

$$N_B^{col} = N_{B'} = \left( \frac{I}{I'} \right) \cdot N_{A'}, \quad (6.10)$$

while the number of events contributing to the CS D,  $N_D^{col}$ , is estimated as

$$N_D^{col} = N_{D'} = \left( \frac{I}{I'} \right) \cdot N_{C'}, \quad (6.11)$$

where the general assumption is that  $\frac{N_{B'}}{N_{A'}} = \frac{N_I}{N_{I'}}$  and  $\frac{N_{D'}}{N_{C'}} = \frac{N_I}{N_{I'}}$ , with each  $N_i$  being the number of events in each CS  $i = A', B', C', D', I, I'$ .

### 3. Combined Background Estimation:

Now that we have estimates for both collision and non-collision event contributions, we can estimate the total number of background events expected in the signal CS D (Events with  $E_T > 60$  GeV,  $E_T^{\gamma} > 60$  GeV and  $3.0 < t_{\gamma} < 13.0$  ns), as

$$N_D^{Total} = \left( \frac{N_B - N_B^{col}}{N_A} \right) \cdot N_C + N_D^{col} = N_D^{non-col} + N_D^{col} \quad (6.12)$$

where  $N_D^{Total} = N_D^{non-col} + N_D^{col}$  is the total background events estimated in our signal CS D coming from non-collision and collision background events.

### Background Estimation Technique Validation

We performed a validity test of our background estimation method using a data sample of 0 and 1-jet events, where we do not expect any signal events. A statistical agreement in the number of expected background events obtained using our background estimation method and the number of events observed in our signal CS D, will indicate provide a positive affirmation that the method. The accepted 0 and 1-jet events used must pass the same event selection requirements as potential signal events described in Tables 6.4 and 6.5. The event yields in each control sample including the tagging of beam-halo, cosmic and spike events is shown in Table 6.10.

Control Sample	Yield	Beam Halo	Cosmic	Spike
A	852	5075	237	65
B	39	300	17	1
C	359	1508	368	9
D	10	22	30	0
<i>A'</i>	8	1	1	0
<i>C'</i>	2	0	0	0
<i>I</i>	35464	-	-	-
<i>I'</i>	1446522	-	-	-
<i>B'</i>	-	-	-	-
<i>D'</i>	-	-	-	-

Table 6.10: Event yields used in validity test for the ABCD background estimation method using 0 and 1-jet events sample. Beam halo/cosmic/spikes yields are obtained from tagged events. Events must pass photon, jet and  $E_T^{\text{miss}}$  selection requirements.

Using the event yields in Table 6.10 for each CS, and Equations 6.10, 6.11 and 6.12, we obtain the following estimates for the expected number of events in signal CS D as

$$\begin{aligned}
 N_B^{col} &= \frac{35464}{1446522} \times 8 = 0.20^{+0.08}_{-0.06} \\
 N_D^{col} &= \frac{35464}{1446522} \times 2 = 0.05^{+0.05}_{-0.02} \\
 N_D^{Total} &= \left( \frac{39 - 0.20}{852} \times 359 \right) + 0.05 = 16.40^{+3.04}_{-2.63}.
 \end{aligned}$$

The uncertainty are statistical uncertainties based on the event statistics in each CS. Our expected number of background events in signal CS D is  $16.40^{+3.04}_{-2.63}$  which is, within the statistical uncertainties, agreeable with the 10 events we observed satisfying all our event selection requirements and belonging to the CS D. This give us confidence that our method is working and should be used in our background estimation method for potential signal events from data sample.

### 6.3.5 Background Estimation Cross Check

Another method for estimating background events with out-of-time photons from collision, which we did, is using  $Z \rightarrow e^+e^-$  events. Since we expect most of the events with electron candidates from  $Z$  decay to be in-time due to the prompt nature of the decay of  $Z$  bosons, we use events with electron candidates from a **SingleElectron** and **DoubleElectron** data samples of 2012, where we expect the contributions from non-collision events to be very small, to do the estimation. These events are selected such that out-of-time energy deposits in ECAL from electron candidates are accepted. The background events with out-of-time energy deposits are mostly events produced from the Drell-Yan process, where electron candidates can be matched randomly to produce a di-electron mass close to the mass of  $Z$  and poorly reconstructed out-of-time energy deposits in ECAL. To further reduce any out-of-time contribution from beam halo and cosmic events, which can occur simultaneously with true  $pp$  collision events, we require that events with  $Z$  candidates must satisfy the following event selection requirements: the two electron candidates of the  $Z$  boson must each have a  $p_T > 30\text{ GeV}/c$ , di-electron mass,  $|m_{e^+e^-} - 91| > 61\text{ GeV}/cc$ , and both electrons must be in the barrel, i.e.  $|\eta_{e^-}| < 1.479$  and  $|\eta_{e^+}| < 1.479$ .

From these selected  $Z$  candidate events, we define a signal event sample where the  $Z$  candidates have a well defined di-electron mass between  $76 < |m_{e^+e^-}| < 100\text{ GeV}/c^2$  and a background or sideband event sample where the di-electron mass is either between  $50\text{ GeV}/c^2 < m_{e^+e^-} < 76\text{ GeV}/c^2$  or  $100\text{ GeV}/c^2 < m_{e^+e^-} < 130\text{ GeV}/c^2$ .

The electron ECAL arrival time is taken to be the seed crystal time adjusted to account for the electron time of flight. The seed crystal must satisfy the recommended crystal (reconstructed hit) cleaning criteria which requires that the seed crystal is not a spike, is not noisy and has been properly time calibrated. A scatter plot of the arrival ECAL time against  $\eta$  (top plots) and  $\phi$  (bottom plots) of the electron candidate of  $Z$  is shown in Figure 6.17. A clear difference in the scatter distributions of events is seen comparing events from the **Single/DoubleElectron** data sample (plots on the right) which do not have the familiar beam halo features (the X-shape and increase event population around  $\phi = 0, \pm\pi$ ) to events from **SinglePhoton** data sample (plots on the left). This confirms our expectation that the candidate  $Z$  event sample is free from contamination from non-collision events and thus a good sample for estimating

out-of-time event contributions from collisions.

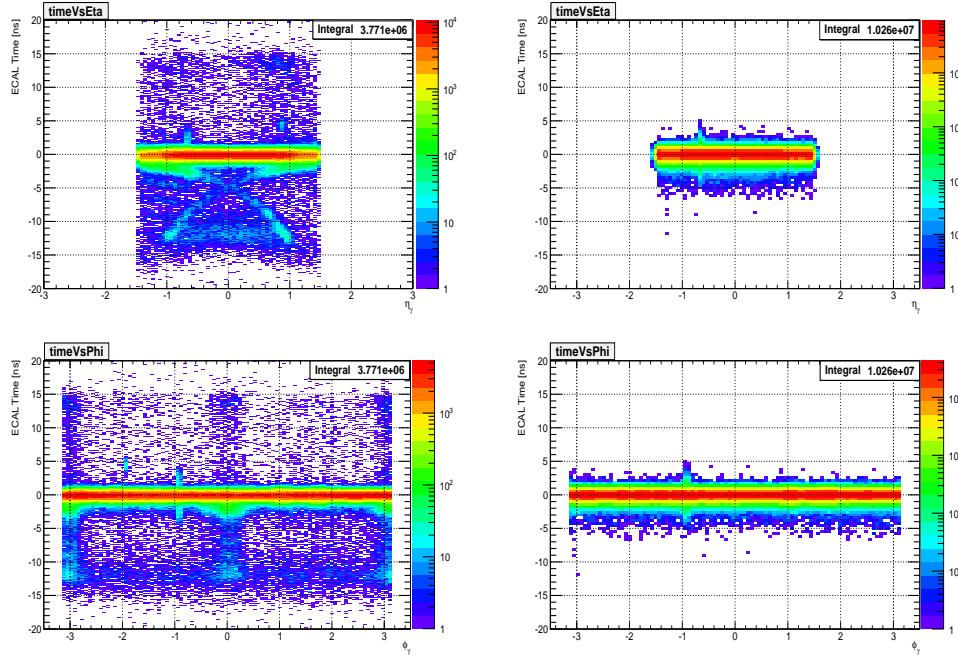


Figure 6.17: ECAL time  $Vs \eta$  (top plots) and  $Vs \phi$  (bottom plots) for photon candidates from SinglePhoton dataset (left) compared to electron candidates from the DoubleElectron dataset (right). All photons or electron candidates are in barrel subdetector. Most of the photons with  $\phi = 0, \pm\pi$  are halo photons which are not observed in the Z boson candidate sample.

The di-electron mass (left plots) and electron arrival time (right plots) of both electron candidates of the Z boson for signal (blue) and sideband (red) events is shown in Figure 6.18. The out-of-time background contribution to the true Z events sample is estimated using a *sideband subtraction method* described as follows:

- We fit the di-electron candidate mass distribution of the sideband control sample with a polynomial function (see top plots of Figure 6.19) to extract the background template.
- Using the background template, we obtain a scale factor as

$$\text{Scale Factor} = \frac{N}{M_1 + M_2}, \quad (6.13)$$

shown in the bottom plot of Figure 6.19, which we used to determine the correct contribution of the background events to the signal event sample.

- After scaling the electrons arrival ECAL time distribution (red distribution on the bottom right plot in Figure 6.18) of the sideband control sample using the extracted scale factor, we subtract the scaled time distribution from the time distribution (blue distribution of right plot in Figure 6.18) of Z electron candidates from the signal sample. The resulting ECAL time distribution, shown in Figure 6.20 is the time distribution from true Z events. This ECAL time distribution is used to estimate the number of events with out-of-time electromagnetic particles from collision.
- The ratio of the total number of events with the electron ECAL time,  $t > 3$  ns, to those with electron ECAL time,  $|t| < 2$  ns, i.e.  $N_{t>3\text{ ns}}/N_{|t|<2.0\text{ ns}}$ , gives an estimate of the fraction of out-of-time background events from collision.

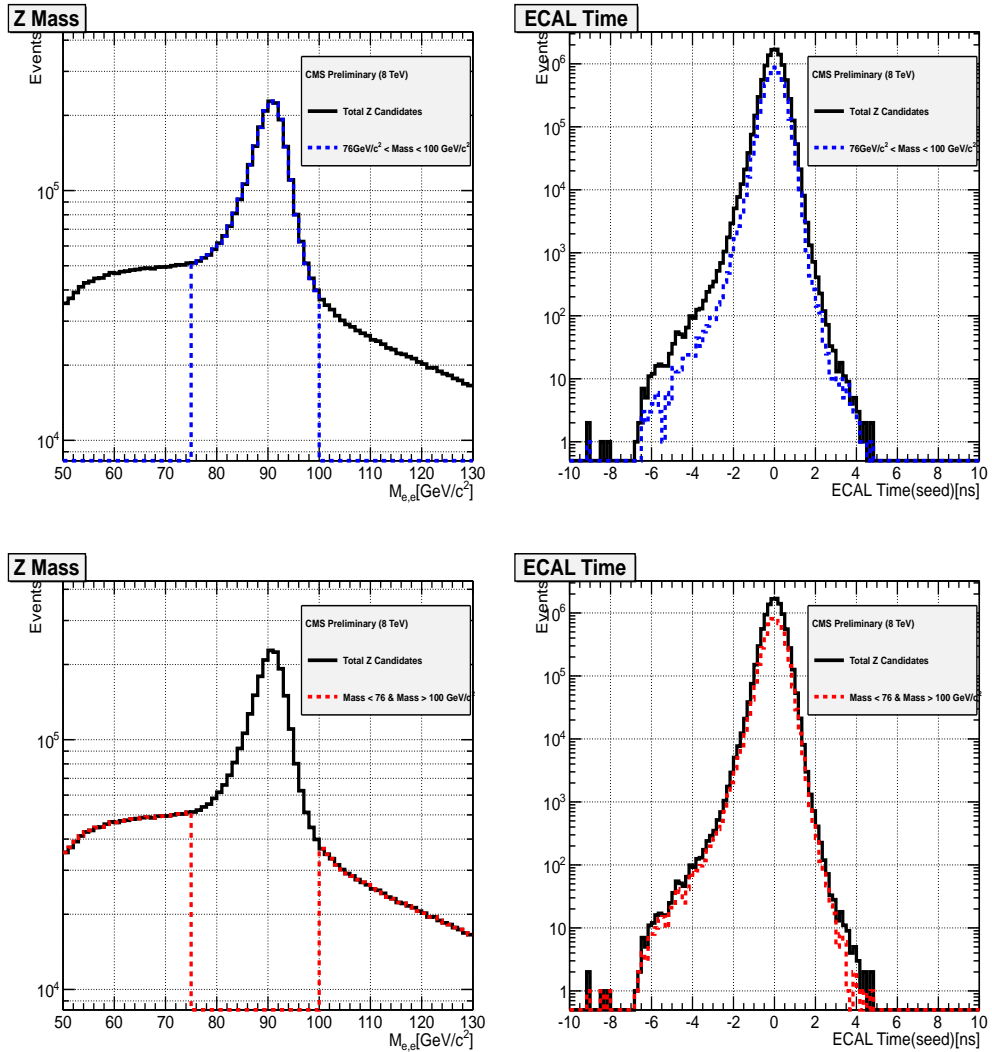


Figure 6.18: Di-electron mass distribution (left) and the time (right) of the two electron candidates for the signal  $76 < m_{e+e-} < 100 \text{ GeV}/c^2$  Z boson sample and for sideband sample ( $50 < m_{e+e-} < 76 \text{ GeV}/c^2$  and  $100 < m_{e+e-} < 130 \text{ GeV}/c^2$ ). Events are from the Single/DoubleElectron data sample.

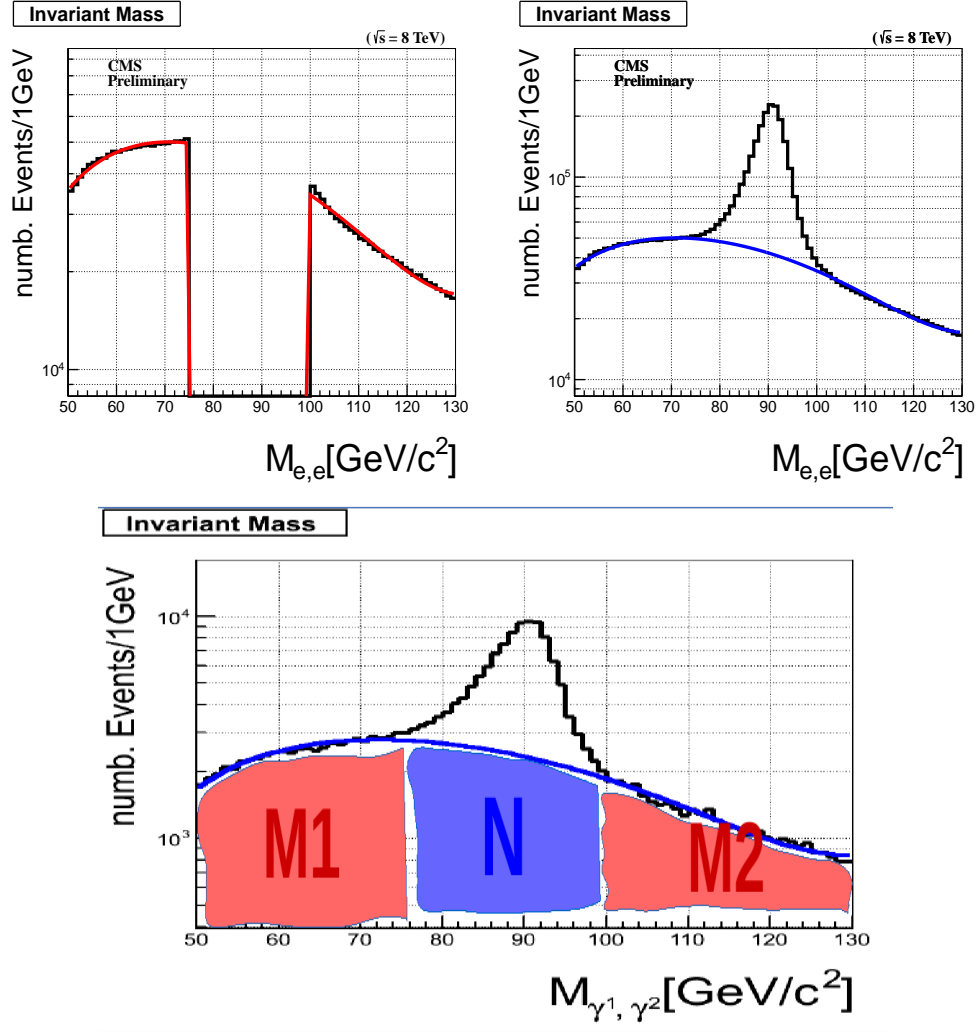


Figure 6.19: *Top:* Polynomial fit (red & blue lines) of the di-electron invariant mass of candidate Z events for the sideband control sample (left) only and all Z events (right). *Bottom:* Fitting the total Z event sample with template extracted from fitting the sideband CS to extract the scale factor use for estimating the background event contribution in true Z signal events sample.

The estimated ratio for out-of-time events to in-time collision events for the final time distribution of signal electron candidates after the normalized sideband subtraction, shown in Figure 6.20 is about,  $N_{t>3 \text{ ns}}/N_{|t|<2.0 \text{ ns}} = 1.29^{+0.374}_{-0.325} \times 10^{-5}$ .

To obtain an estimate of the number of background events from collisions in the signal control sample D,  $N_D^{col}$ , of the  $\tilde{\chi}_1^0$  decay, we multiply this estimated ratio to the

total number of in-time events (CS *I*), shown in Table 6.12, passing our final signal event selections requirements, which is 28282. This gives  $N_D^{col} = 0.366_{-0.092}^{+0.106}$  events. Comparing this to the value obtained with the ABCD method, which is  $\frac{28283}{1446522} = 0.0391_{-0.047}^{+0.039}$  events, we find that the two methods of estimating the number of background events from collision are not exactly equal.

We cannot interpret this inequality as a disagreement between both methods for estimating the number of background events from collision. On the contrary, this non-agreement can be explained. We have not applied any  $E_T^{\text{miss}}$  selection requirements for the Z candidate events selection. A simple cut in missing transverse energy,  $E_T^{\text{miss}} > 60 \text{ GeV}$ , could further reduce the estimated ratio,  $N_{|t|>3 \text{ ns}}/N_{|t|<2.0 \text{ ns}}$ , to a very smaller number than what we got. In fact, the smallness of this ratio confirms our speculation that indeed the contribution from collision events with out-of-time electromagnetic particles to our background events is almost negligible (less than a single event) such that the uncertainties on the ratio of out-of-time to in-time events used in our ABCD collision background estimation is irrelevant. This means, the number  $N_D^{col} = 0.366_{-0.092}^{+0.106}$ , can be used for our estimated number of background events from collision and our final results will not change by a lot.

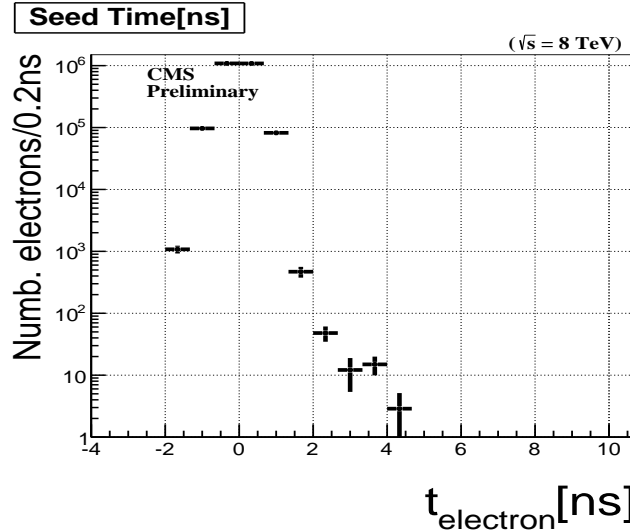


Figure 6.20: ECAL time distribution of genuine Z bosons after background contribution is subtracted.

## 6.4 Systematic Studies

Our event selection comprise of the following selection cuts: photon  $p_T$  greater than  $80\text{ GeV}/c$ , jet  $p_T$  greater than  $35\text{ GeV}/c$  and missing energy greater than  $60\text{ GeV}$ . The same selection requirements applied to our MC signal event sample should guarantee a good event selection efficiency. Any difference in the photon  $p_T$ , jet  $p_T$  and missing transverse energy between MC and data, will be a source of systematic uncertainties on the efficiency of selecting signal events. These uncertainties can come from quantities like jet energy scale (JES), jet energy resolution (JER), electron-photon energy scale, instrumentation related and missed or energy deposits not clustered during missing transverse energy reconstruction, photon ECAL arrival time bias and ECAL time resolution. The different sources of uncertainties considered in this analysis is presented in Table 6.11. We obtain these uncertainties by varying the nominal values of each quantity, while keeping the others fixed, by  $1\sigma$  deviation and counting the number of events passing our event selection requirements. Our largest uncertainty is from ECAL timing bias on the absolute reference time (zero ns) of the ECAL timing used for measuring the photon arrival time. This has the largest impact on our analysis since our analysis is based on counting the number of events with photon ECAL time above 3 ns. The next largest uncertainties are from energy deposits not clustered. This affects the photon energy scale, missing energy scale, jet energy scale and resolution.

The uncertainty on the photon energy scale in the barrel was estimated to be 4.0% based on measuring the photon energy of events with  $Z \rightarrow \mu\mu\gamma$  decay, where the muon radiates a photon in a process known as the final-state radiation (FSR)[55].

The uncertainty on the  $E_T^{\text{miss}}$  resolution uses a conservative estimate from  $E_T^{\text{miss}}$  measurements in QCD events [56].

The uncertainty on the ECAL time resolution was obtained by comparing the mean time of photons of events from  $\gamma +$  jet MC sample to events from data with photon ECAL time,  $|t_\gamma| < 2\text{ ns}$ . The difference is found to be of the order of 200 ps per event. The systematic uncertainty on luminosity measurement has the recommended value of 2.2% provided by CMS and LHC luminosity measurements while the uncertainty from parton density functions (PDF) is evaluated using the re-weighting technique which uses the Master Equation of CTEQ65 model set described in [57].

Another important source of systematic is in the selection of the background control samples and our background estimation and individual systematic in the tagging and mistagging of non-collision background and estimating background contributions from collisions. We combined these separate uncertainty contributions into a single background estimation uncertainty referred here as our background estimation uncertain. However, since our background estimation is data-driven, most of the uncertainties arising due to systematic can be neglected (less than 1% impact) as they cancel out. This is our largest source of uncertainty in our analysis which we estimate to vary it upward by 223% and downward by 51% as a statistical uncertainty in the ABCD background estimation method. The large background statistical uncertainty is due to very low event statistics. However, despite the large background estimation uncertainty, the signal selection uncertainties are the most significant uncertainties which impact our final results. These uncertainties are used as nuisance parameters in the calculation of the upper limit on observed signal cross-section ( $\sigma_{UL}$ ).

Source	Uncertainty(%)
ECAL absolute time (0.0 ns)	< 10.0%
ECAL time resolution (0.5 ns)	< 5.0%
Unclustered energy deposits	< 9.0%
Photon energy scale	< 4.0%
Jet energy scale (JES)	< 9.0%
Jet energy resolution (JER)	< 9.0%
$E_T^{\text{miss}}$ resolution	< 2.8%
PDF uncertainty	< 1.70%
Background estimation uncertainty	51.0% to 223%
Luminosity (4.5%)	< 2.2%

Table 6.11: Summary of systematic uncertainties for signal efficiency and background estimation in this analysis and applied to our final results.

## 6.5 Results

After running our analysis on the SinglePhoton data samples requiring events with at least 2 jets, at least one photon with ECAL time  $3.0 < t_\gamma < 13.0$  ns,  $\cancel{E}_T > 60$  GeV, and  $\cancel{E}_T > 60$  GeV, we observed a single event passing all our event selection requirements as a signal event. This event has one photon and two jets. The photon has a transverse momentum of  $224$  GeV/c and an ECAL time of 12.17 ns.

Our final expected number of background events estimated is  $0.093^{+0.301}_{-0.047}$ . This number was computed as

$$\begin{aligned} N_B^{col} &= \frac{28283}{605496} \times 3 = 0.140^{+0.108}_{-0.061} \\ N_D^{col} &= \frac{28283}{605496} \times 2 = 0.093^{+0.093}_{-0.047} \\ N_D^{Total} &= \left( \frac{1 - 0.14}{3} \times 0 \right) + 0.093 = 0.093^{+0.301}_{-0.047}. \end{aligned}$$

using the event yields and background events vetoed presented in Table 6.12.

Control Sample	Yield	Beam Halo	Cosmic	Spike
D	1	0	0	0
C	0	2	1	0
B	1	1	1	1
A	3	6	0	0
<i>A'</i>	2	0	0	0
<i>C'</i>	4	0	0	0
<i>I</i>	28283	-	-	-
<i>I'</i>	669013	-	-	-

Table 6.12: Event yields used in our final background estimation for signal candidate events with at least a single photon and at least 2 jets,  $\cancel{E}_T > 60$  GeV, and  $\cancel{E}_T > 60$  GeV.

With no significant excess over expected number of background events, we find upper limits on the number of event counts at 95% confidence limit using the statistical CLs limit finding method.

## Chapter 7

# Statistical Analysis

### 7.1 Limit Computation

The upper limit calculation procedure used in this analysis is the CLs technique. We fed carefully estimated amounts of background and signal with systematic to obtain the limit. The variable for which the 95% upper limit is set unlike previous experiments is based entirely on the neutralino proper decay length,  $c\tau_{\tilde{\chi}_1^0}$ .

The method we used in our upper limit calculation is by first performing a Hypothesis test and then use the result of this test to derived our confidence intervals. We do the following:

- We define a NULL hypothesis ( $H_0$ ) and the Alternate hypothesis ( $H_1$ ). If we had several other hypothesis, we will defined them also.
- Select a Test statistics ( $t(x)$ ), where  $x$  is the data.
- Select a corresponding test statistics calculator.
- Use the result of the hypothesis test to compute the interval by inverting the result of the hypothesis test.

First, we describe the acceptable technique in experimental high energy physics for computing *p-values* used in any search and discovery experiment.

### 7.1.1 CLs Technique

The  $CL_s$  technique [58] is attributed as the standard technique or framework for computing the confidence or exclusion intervals in a search and discovery experiment. It has been shown to work during the search for the Higgs boson at LEP and recently in the discovery of the scalar boson in 2012, by both CMS and ATLAS experiments with the mass of this boson being:  $m_H = 125.36 \pm 0.37(\text{stat.Unc}) \pm 0.18(\text{syst.Unc})$ .

This method has been implemented in a unique statistical software package called *HiggsCombine* with the goal of providing direct access to a variety of robust statistical methods with optimised performance for computing limits or confidence intervals. *HiggsCombine* [60] is the official standard tool recommended by the CMS statistical committee and CMS Higgs group for calculating limits in any CMS search and discovery analysis. It takes as input estimates on the number or distribution of signal and background and the observed number or distribution from data and produces an upper limit in the production cross section of a given physics process for a given value of a parameter of interest (POI). *Higgscombine* tool has the advantage in that, it allows for the possibility to use several different statistical methods of calculating the upper limit. This way, one can make comparison and simple checks for any inconsistency. In this analysis, we used an Asymptotic [61] and HybridNew (a hybrid of Frequentist and Bayesian methods),[60], to calculate our observed upper limits. The purpose of the using the  $CL_s$  method is to compute reliable upper limits in a search scenario when the observed signal is very small compared to the background. In the  $CL_s$  technique, one uses not the p-value ( $CL_{s+b}$ ) but rather divide this by  $CL_b$  (which is 1 minus the p-value for background only hypothesis). The reason for this is to define a conditional probability conditioned to the scenario of observing only background or background only hypothesis. The  $CL_s$  is formally defined as:

$$CL_s = \frac{CL_{s+b}}{CL_b} = \frac{p_{s+b}}{1 - p_b} \quad (7.1)$$

where  $s + b$  means signal and background.

### 7.1.2 Statistical Test Formalism

The Neyman-Pearson Theorem states that the likelihood ratio gives the most powerful hypothesis test. Therefore, we construct our test statistics  $t_\mu$  as a function of the observed data, as a likelihood ratio. In a search analysis, one defines the null hypothesis  $H_0$  describing only known processes, or the background only which is to be tested against an alternate hypothesis  $H_1$  defined as a background and signal. However in the computation of upper limits:

- $H_0$  being the NULL hypothesis includes the background and signal ( $s + b$ ) while
- $H_1$  being the ALTERNATE hypothesis includes only the background ( $b$ ).

Using these, two hypothesis we quantify the level of agreement between our observed data with either of the hypothesis by computing a  $p$ -value ( $p$ -value if the probability under the assumption of a given hypothesis, of finding data of equal or greater incompatibility with the predictions of the given hypothesis). A given hypothesis is then regarded as being excluded if its  $p$ -value is observed below a given threshold. In particle physics, this threshold value for the  $p$ -value is 0.05 corresponding to 95% of confidence level (CL). The CMS accepted method of computing upper upper limit is based on mix of frequentist-hybrid significance test using the profilelikelihood ratio as a test statistics (HybridNew method). The parameter of interests in in our case the rate (cross section) of signal process as well as *nuissance parameters* as systematics for the background and signal models. This parametrized systematics effects results, as is always the case, to loss in sensitivity.

In this search experiment, for each event in the signal, we measured the timing of the photon as our observable. We use this value to construct a histogram  $\mathbf{n} = (n_1, \dots, n_N)$ . The expectation value for each value of  $n_i$  can be written as:

$$E[n_i] = \mu s_i + b_i \quad (7.2)$$

where  $\mu$  is the parameter which determines the signal strength, when  $\mu = 0$  means background-only and when  $\mu = 1$  then we have the signal and background hypothesis.

The the mean number of entries in the  $i$ th bin from signal and background are given as:

$$s_i = s_{tot} \int_{bin,i} f_s(t; \theta_s) \quad b_i = b_{tot} \int_{bin,i} f_b(t; \theta_b) \quad (7.3)$$

with the functions  $f_s(t; \theta_s)$  and  $f_b(t; \theta_b)$  being the probability density functions (Pdfs) of the variable  $t$  for the signal and background events and  $\theta_s$  and  $\theta_b$  representing the parameters which characterise the shapes of the pdfs.  $s_{tot}$  and  $b_{tot}$  represents the total mean numbers of signals and backgrounds while the integrals represent the probabilities for an event to be found in bin  $i$ .  $\theta = (\theta_s, \theta_b, b_{tot})$  denote all nuisance parameters (systematic uncertainties) while  $s_{tot}$  is the signal normalization is fixed to the value predicted by the nominal signal model.

The likelihood function is the product of the Poisson probabilities for all bins:

$$\mathcal{L}(\mu, \theta) = \prod_{r=1}^N \frac{(\mu s_r + b_r)^{n_r}}{n_r!} e^{-(\mu s_r + b_r)} \cdot \mathcal{G}(\theta) \quad (7.4)$$

where  $\mathcal{G}(\theta)$  is a discrete (Poisson) distribution of the nuisance parameters. This distribution can be different for different nuisance parameter.

Using the likelihood function, the profilelikelihood ratio is then defined as:

$$\lambda(\mu) = \frac{\mathcal{L}(\mu, \hat{\theta})}{\mathcal{L}(\hat{\mu}, \hat{\theta})} \quad (7.5)$$

Here  $\hat{\theta}$  is the the value of  $\theta$  that maximizes  $\mathcal{L}$  for a specified  $\mu$ , thus, it is referred to as the *conditional maximum-likelihood estimator* (CMLE) of  $\theta$  (given as a function of  $\mu$ ). While  $\mathcal{L}(\hat{\mu}, \hat{\theta})$  is the maximized (unconditional) likelihood function with  $\hat{\mu}$  and  $\hat{\theta}$  being its *maximum likelihood* (ML) estimators. The nuisance parameters broadens the profilelikelihood as a function of  $\mu$  relative to what is expected if their values where fixed and this reflects in the loss of sensitivity or information about  $\mu$  due to the systematic uncertainties.

### 7.1.3 Test Statistics and $p$ -values

The above expression for  $\lambda(\mu)$  shows that  $0 \leq \lambda \leq 1$ , where  $\lambda$  close to 1 indicates a very good agreement between the data and hypothesis value of  $\mu$ . The test statistics to be used for our statistical test is defined as:

$$t_\mu = -2 \ln \lambda(\mu) \quad (7.6)$$

It is important to note that the test statistics approach to any statistical test is favourable because just by looking at the values of the test statistics, higher values corresponds to increasing incompatibility between the data and the value of  $\mu$  which is from the signal hypothesis. This incompatibility or disagreement between the data and a given hypothesis is quantified by calculating the probability or  $p$ -value as:

$$CL_{s+b} = p_u = \int_{t_{\mu,obs}}^{\infty} f(t_\mu|\mu) dt_\mu \quad (7.7)$$

where,  $t_{\mu,obs}$  is the value of the test statistics  $t_\mu$  obtained from the data and  $f(t_\mu|\mu)$  is a pdf constructed from  $t_\mu$  depending on the signal strength  $\mu$ . The set of values for  $\mu$  that are rejected because their  $p$ -value is below a specified threshold value  $\alpha$  lying on either sides of those not rejected gives a two sided confidence interval of  $\mu$  and if just on one side of the ones not rejected gives an upper limit on the rejected values of  $\mu$ .

In the background only scenario i.e  $\mu = 0$ , the test statistics is defined as:

$$q_\mu = \begin{cases} -2 \ln \lambda(0), & \hat{\mu} \geq 0 \\ 0, & \hat{\mu} \leq 0 \end{cases}$$

where  $\lambda(0)$  is the profilelikelihood ratio for  $\mu = 0$  defined in 7.5. and again to quantify the disagreement between the background-only hypothesis ( $\mu = 0$ ) and the data is given by the  $p$ -value as:

$$CL_b = p_0 = \int_{q_{0,obs}}^{\infty} f(q_0|0) dq_0 \quad (7.8)$$

where  $f(q_0|0)$  denotes the pdf if the test statistics  $q_0$  under the background-only ( $\mu = 0$ ) hypothesis. Figure 7.1 shows a sampling distributions of the test statistics and how the

*p*-values can be extracted from these distributions.

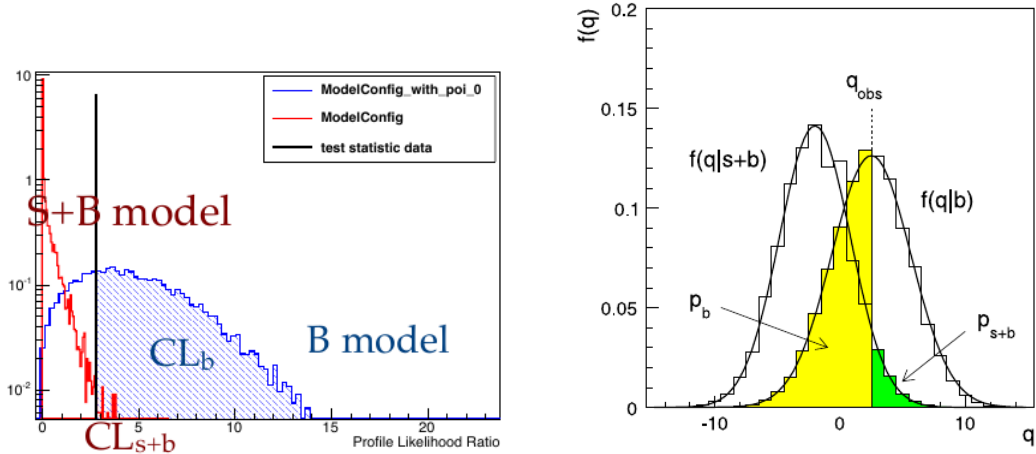


Figure 7.1: Sampling distributions for  $f(t_\mu|\mu)$  showing how one extracts the  $p$ -values. left: is the using a analytic of the Asymptotic method and right: is from the HybridNew method.

In addition to the  $p$ -value, for expressing the disagreement between the data and a given hypothesis, the Higgscombine tool also provides a quantity known as the *significance* ( $\mathcal{Z}$ ).  $\mathcal{Z}$  and the  $p$ -value have a very non-linear relation. Once can defined that relation using a two-sided fluctuation if a Gaussian variable  $\sigma$ , with  $5\sigma$  significance corresponding to a  $p$ -value of  $p = 5.7 \times 10^{-7}$  to denote a discovery. Since, we have not observed any significant excess of events over our standard model background, we will not mention a lot about significance in this thesis, but rather talk about  $p$ -values as they are indispensable in computing limits.

The important question is always, how does one obtain an expression or a distribution of the test statistics and  $f(t_\mu|\mu)$  from the likelihood function? To answer this question, the HiggsCombine tool was developed which consist of various ways of both analytically (e.g the Asymptotic statistical method [61]) or through numerical integration or Monte Carlo computation ( e.g the HybridNew statistical method) obtain the test statistics and  $f(t_\mu|\mu)$ . We have shown the limit computation results of both methods as used in this analysis. As an example, the pdf  $f(q_\mu|\mu)$  of the test statistics ( $q_\mu$ ) obtained though the **Asymptotic** statistical method as given in [61] is:

$$f(t_\mu|\mu') = \Phi\left(\frac{\mu - \mu'}{\sigma}\right)\delta(t_\mu) + \frac{1}{2}\frac{1}{\sqrt{2\pi}}\frac{1}{t_\mu}\exp\left[-\frac{1}{2}\left(\sqrt{t_\mu} - \frac{\mu - \mu'}{\sigma}\right)^2\right] \quad (7.9)$$

where result to a half-chi-square distribution when  $\mu = \mu'$ .

In subtle point worth mentioning is that in the HybridNew approach, systematics uncertainties are taken into account through the Bayesian prior density  $\pi(\theta)$ , and the distribution of the test statistics is computed under the assumption if the Bayesian model of average given as:

$$f(q) = \int f(q|\theta)\pi(\theta)d\theta$$

and the prior pdf  $\pi(\theta)$  is obtained from some measurements characterised by a given likelihood function  $\mathcal{L}_\theta(\theta)$  which is then used to find the prior using Bayes' Theorem. Unlike other cases where systematic uncertainties are taking as being part of the data and incorporated directly through  $\mathcal{G}(\theta)$  as shown in equation 7.4. Nevertheless, they arrive at the same result.

In summary, the hypothesis test is performed using a given statistical method on each value of a chosen parameter of interest (POI)(usually denoted  $\mu$ ). The  $p$ -value if obtained from the sampling distribution of the test statistics being used. Can either obtain this test statistics analytically or through Monte Carlo computation and numerical integration. By plotting the p-value as a function of the POI, we obtain the p-value curve (in this case the  $CL_s = \frac{CL_{s+b}}{CL_b}$ ). The value of  $\mu$  which has a p-value  $\alpha$  ( e.g 0.05) is the upper limit (for 1-dimensional limits,2-dimensional limits gives lower and upper limits) of  $1 - \alpha$  confidence interval (e.g 95%).

## combined result

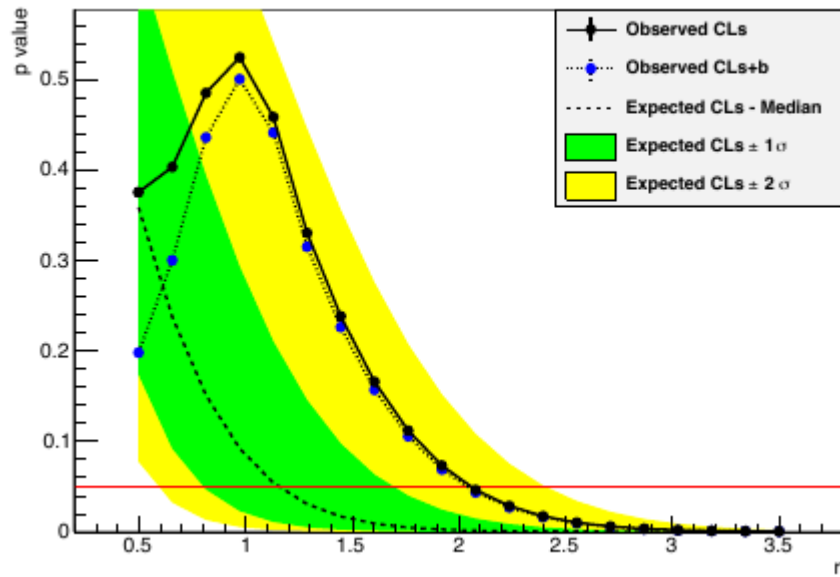


Figure 7.2: Distribution of  $p$ -values showing how upper limit on  $\mu$  is extracted for a given threshold probability.

## Chapter 8

# Limit Interpretation

Using the  $CL_s$  technique, the HiggsCombine tool produces an upper limit along with the expected limit at different quantiles as the signal strength computed which is a ratio of Number of Signal events over the Number of Expected signal events i.e

$$r = \frac{N^{Obs}}{N_{expect}} \quad (8.1)$$

and using the equation as given in chapter 3 on the cross-section  $\sigma = \frac{N}{\varepsilon \cdot A \cdot \mathcal{L}}$  and hence the observed cross-section upper limit is given as:

$$\sigma_{UL}^{Obs} = \frac{r \cdot N^{expect}}{\varepsilon \cdot A \cdot \mathcal{L}} \quad (8.2)$$

where  $\mathcal{L}$  is the integrated luminosity ( $19 \text{ fb}^{-1}$ ) and  $\varepsilon$  and  $A$  are the signal selection efficiency and Acceptance respectively. In addition to the observed limits (Solid black line), the uncertainties on the expected limits at 68%/16% ( $\pm 1\sigma$ ) and at 98%/2.5% ( $\pm 2\sigma$ ) provide the **GREEN** and **YELLOW** respectively, the error from the median (50%) expected limits (dashed red line) shown in figure 8.2.

### 8.1 Signal Efficiency and Acceptance

After our final selection on MC signal sample, the number of signal events passing our selection requirements for different neutralino lifetime and same mass,  $\Lambda = 180 \text{ TeV}$ , is

given in table 8.1. We use these numbers and those for other neutralino lifetimes and masses to compute our exclusion limits.

SPS8 GMSB Signal	Number of Events
GMSB(SPS8) ( $\Lambda = 180$ TeV, $c\tau = 250$ mm)	0.2096
GMSB(SPS8) ( $\Lambda = 180$ TeV, $c\tau = 500$ mm)	4.5423
GMSB(SPS8) ( $\Lambda = 180$ TeV, $c\tau = 1000$ mm)	6.3646
GMSB(SPS8) ( $\Lambda = 180$ TeV, $c\tau = 2000$ mm)	6.3968
GMSB(SPS8) ( $\Lambda = 180$ TeV, $c\tau = 4000$ mm)	6.1442
GMSB(SPS8) ( $\Lambda = 180$ TeV, $c\tau = 6000$ mm)	4.6498
GMSB(SPS8) ( $\Lambda = 180$ TeV, $c\tau = 12000$ mm)	2.918

Table 8.1: Final number for  $\Lambda = 180$  TeV GMSB SPS8 MC signal events events passing our selection cuts.

The efficiency times acceptance ( $\varepsilon \times A$ ) combined as one is seen the figure 8.1.

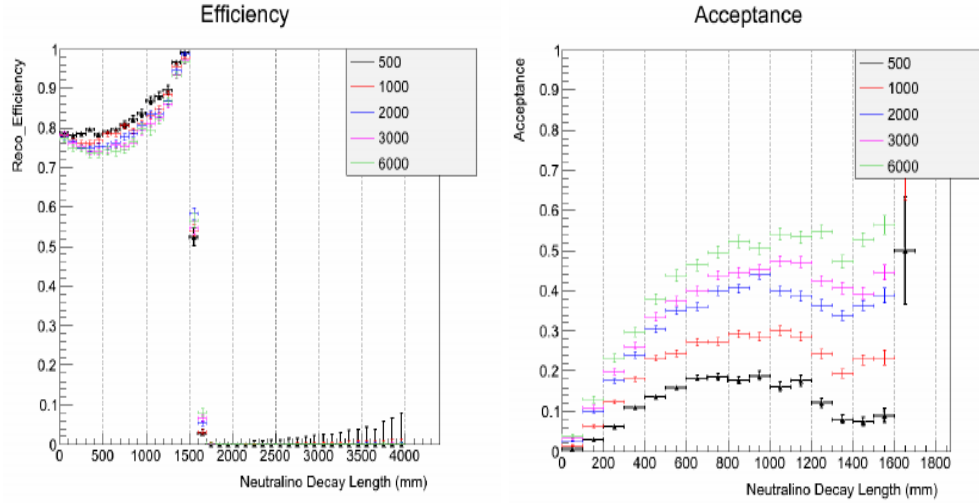


Figure 8.1: The reconstruction and selection efficiency (left)  $\times$  Acceptance ( $t > 3$  ns) (right) against transverse decay length in laboratory frame for different  $c\tau$  points.

The  $\frac{N_{expect}}{\mathcal{L}}$  defines the expected signal cross section which is obtained from a given signal model. In our scenario, our choice of signal model we want to produce exclusion limits on the possible production and decay of a long-lived particle described by this signal model is GMSB. Thus the interpretation of our search analysis is given within the context of any GMSB model with a long-live neutral particle decaying to a photon and gravitino. Such a model is the minimal GMSB or the SPS8 model and the general GMSB model. However, the results provided are based on interpretation within the context of the SPS8 model. In GMSB, the neutralino  $\tilde{\chi}_1^0$  is the NLSP and decays to the gravitino  $\tilde{G}$  the LSP (as a result of R-parity conservation) in association with a very energetic photon  $\gamma$ . Because of the smallness in mass difference between the  $\tilde{\chi}_1^0$  and the  $\tilde{G}$  as well as the coupling, the  $\tilde{\chi}_1^0$  decay to  $\tilde{G}$  is delayed and as a result, the photon emitted can arrive late in the calorimeter crystals. Measuring the arrival time of the photon on ECAL crystals, we can extract important parameters of theory of GMSB.

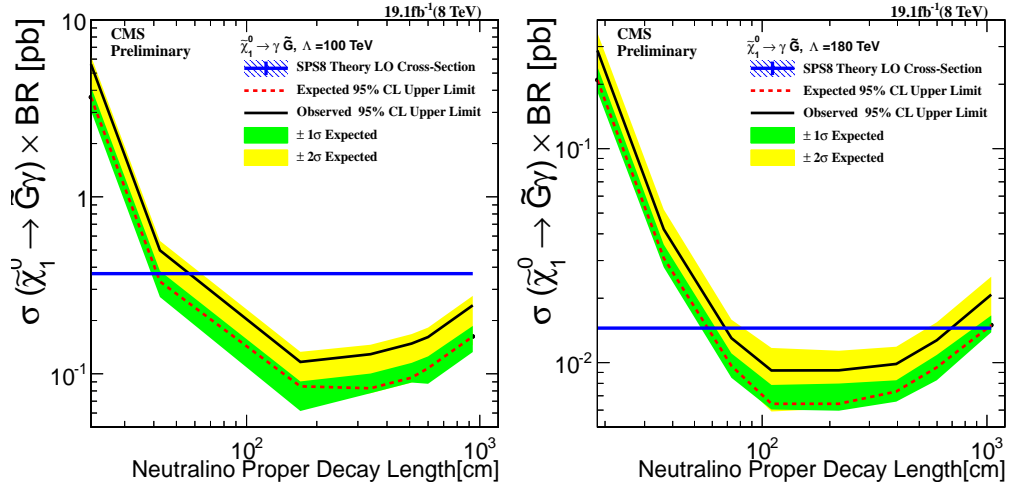


Figure 8.2: Neutralino production cross section against proper delay length upper limit interpretation in SPS8 model. (Left)  $\Lambda = 100 \text{ TeV}$ , (Right)(left)  $\Lambda = 180 \text{ TeV}$

In the SPS8 model, the parameter space for long-live neutralinos is governed by  $\Lambda_m - c\tau$  2-dimensional parameter space. For each  $\Lambda_m$  point, we have a fixed neutralino mass with different proper lifetimes  $c\tau$ . We have obtained limits for  $\Lambda_m$  ranging from 100 TeV

to 180 TeV corresponding to lightest neutralino mass  $m_{\tilde{\chi}_1^0}$  between 90 to 255  $GeV/c^2$  and proper lifetime  $c\tau$  ranging from 250 to 12000 mm corresponding to  $\tau_{\tilde{\chi}_1^0}$  from 0.8 ns to 40 ns.

For a given value of  $\Lambda_m = 180$  TeV, we have a lightest neutralino production cross section times branching ratio plot shown in figure 8.2, showing that the ECAL detector is sensitive to lightest neutralinos of mass  $m_{\tilde{\chi}_1^0} = 255$   $GeV/c^2$  and life time upto 30 ns and we are 95% confident that we have not missed any neutralino whose mass is  $m_{\tilde{\chi}_1^0} = 255$   $GeV/c^2$  and lifetime is  $\tau \leq 30$  ns.

For a given lifetime of  $\tau = 20$  ns, we can also obtain upper limits on the production cross section times branching ratio when compared against their theoretically expected values for a lightest neutralino with mass ranging from  $m_{\tilde{\chi}_1^0} = 90$   $GeV/c^2$  to  $m_{\tilde{\chi}_1^0} = 255$   $GeV/c^2$ . The observed upper limit on this cross section is  $\sigma_{\tilde{\chi}_1^0}^{UP} \geq XX$  pb with proper lifetime of  $\tau = 30$  ns.

Using both the mass and proper lifetime of the lightest neutralino, we present possible 2-dimensional limits simultaneously on  $m_{\tilde{\chi}_1^0}$  or  $\Lambda_m$  and  $c\tau$  or  $\tau$  in the SPS8 model, comparing this with the result of previous experiments. This is shown in Figure 8.3.

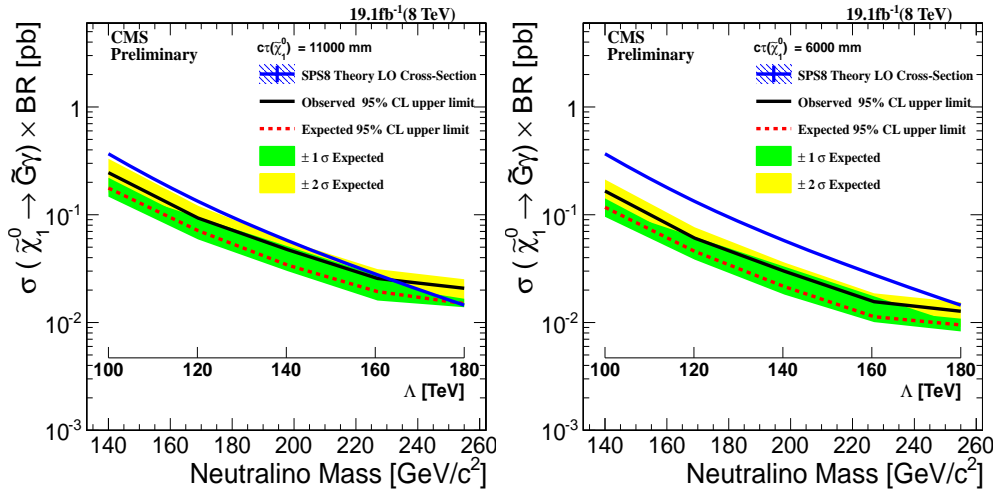


Figure 8.3: Neutralino production cross section against neutralino mass upper limit at 95% confidence levels interpretation in SPS8 model.(Left)  $C\tau = 11000$  mm, (Right)  $C\tau = 6000$  mm

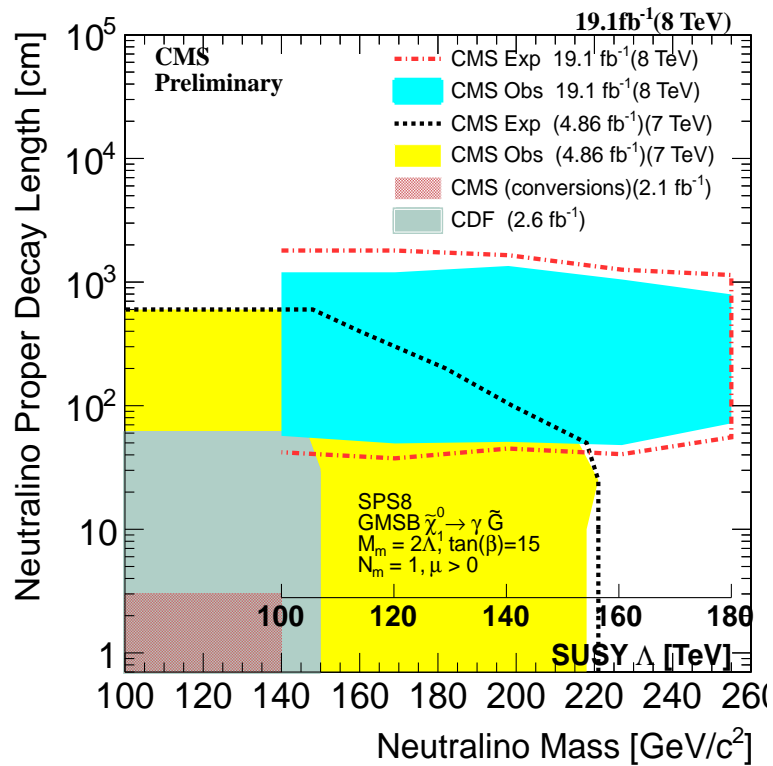


Figure 8.4: Neutralino two dimensional exclusion limit of neutralino mass ( $\Lambda$ ) against proper delay length upper limit interpretation in SPS8 model in the decay  $\tilde{\chi}_1^0 \rightarrow \gamma + \tilde{G}$  with limits from previous experiments shown.

# Chapter 9

## Conclusion

We have performed a search analysis for NMLLP decaying to photons using the time of arrival of the photon as measured by the ECAL sub detector of the CMS detector. Haven fail to find any significant signal of delayed photons over the standard model background, we interpreted our results in SUSY models with NMLLP like SPS8 of minimal GBSM or general GMSB models. We showed that, neutralinos whose production and decay mechanism is described in the SPS8 mGMSB model, with  $m_{\tilde{\chi}_1^0} \leq 235 \text{ GeV}/c^2$  and  $\tau_{\tilde{\chi}_1^0} \leq 35 \text{ ns}$  are ruled out of existence at 95% confidence level using the 2012 8 TeV LHC dataset. This corresponds to an upper limit of  $\sigma_{\tilde{\chi}_1^0}^{UP} \geq 0.02 \text{ pb}$  on the production cross section times branching ratio in a hadron collider. In addition, we mention some of the limitations in this particular analysis from a detector point of view and how in future studies can be improved. We hope that in the future, with increase in center of mass energy of the LHC collider as well as luminosity and an improve in timing resolution beyond what is already very reliable, we will surely find a new fundamental particle whose dynamics cannot be described by the already very successful standard model of particle physics.

# Bibliography

- [1] N. Jarosik et al. (WMAP), *Astrophys. J. Suppl.* **192**, 14 (2011); Overview: K.A. Olive et al.(PDG), *Chin.Phys.C***38**,090001(2014).
- [2] M. Kuhlen, M Vogelsberger, R. Angulo, *Phys.Dark Univ.***1**,50(2012).
- [3] Ellis John, Olive Keith A. (2010). “Supersymmetric Dark Matter Candidates”. arXiv:1001.3651 [astro-ph]
- [4] Laura Covi “Gravitino Dark Matter confronts LHC” *Journal of Physics: Conference Series* 485 (2014) 012002
- [5] J.Ellis, J.Hagelin, D. Nanopoulos, K.A. Olive and M. Srednicki; *Nucl. Phys.* B238 (1984) 453; H. Goldberg, *Phys. Rev. Lett* 50 (1983) 1419; J. Ellis, T. Falk, G. Ganis, K.A. Olive and M. Srednicki, *Phys. Lett. B* 510 (2001) 236, arXiv: hep-ph/0102098.
- [6] B.Allanach et al,arXiv:hep-ph/0202233v1;
- [7] “*Observation of a new boson at a mass of 125 GeV with the CMS experiment at LHC*”, *Phys. Lett. B* 716 (2012) 30-61
- [8] Steven Weinberg, “A Model of Leptons”, *Phys. Rev. Lett.* 19, 12641266 (1967)
- [9] “Observation of a Charged Charmoniumlike Structure in  $e^-e^+ \rightarrow \pi^+\pi^-J/\psi$  at  $\sqrt{S} = 4.26\text{GeV}$ ” M. Ablikim et al. *Phys. Rev. Lett.* 110, 252001 (2013), “Study of  $e^-e^+ \rightarrow \pi^+\pi^-J/\psi$  and Observation of a Charged Charmoniumlike State at Belle”, Z. Q. Liu et al. *Phys. Rev. Lett.* 110, 252002 (2013);

- [10] Peter W. Higgs “Broken symmetries and the masses of gauge bosons”, *Phys.Rev.Lett.* 13.508, 19 October, 1964;
- [11] Haag,Rudolf; Sohnius, Martin; opuszaski, Jan T. “All possible generators of supersymmetries of the S-matrix”, *Nuclear Physics B* 88: 257274 (1975);
- [12] S.Mathin, arXiv:hep-ph/9709356;
- [13] Howard Baer, Xerxes Tata “Weak Scale Supersymmetry: From Superfields to Scattering Events”
- [14] S. Ambrosanio 1 , Graham D. Kribs 2 , and Stephen P. Martin hep-ph/9703211 arXiv:hep-ph/9703211v2.
- [15] G.F. Giudice and R. Rattazzi “ Theories with Gauge-Mediated Supersymmetry Breaking” arXiv:hep-ph/9801271v2
- [16] J.Dann et al.(LEPSUSY Working Group), Internal note LEPSUSYWG/97-04(1997), P. Janot, talk at the EPS Conference, Jerusalem, 1997.
- [17] CDF Collaboration, “Search for Supersymmetry with Gauge-Mediated Breaking in Diphoton Events with Missing Transverse Energy at CDFII “, *Phys. Rev. Lett.*
- [18] ATLAS Collaboration “Search for Diphoton Events with Large Missing Transverse Momentum in  $1 fb^{-1}$  of 7TeV Proton-Proton Collision Data with the ATLAS Detector”, arXiv:1111.4116v1, 17th Nov 2011.
- [19] CMS Draft Analysis, “Search for Long-Lived Particles using Displaced Photons in  $PP$  Collision at  $\sqrt{S} = 7TeV$  ”, CMS AN AN-11-081 104(2010)011801,
- [20] ATLAS Collaboration, J. High Energy Phys. 1212, 124 (2012), arXiv:1210.4457 [hep-ex]
- [21] The LHC Machine, Lyndon Evans and Philip Bryant *Jinst*,
- [22] CMS Collaboration, “CMS Physics: Technical design report, Volume 1” CERN-LHCC-2006-001
- [23] The CERN Brochure 2009-003-Eng

- [24] CMS Collaboration, “The CMS experiment at the CERN LHC”, JINST 0803:S08004, 2008.
- [25] CMS uses a right-handed coordinate system, with the origin at the nominal interaction point, the  $x$ -axis pointing to the center of the LHC, the  $y$ -axis pointing up (perpendicular to the LHC plane), and the  $z$ -axis along the counterclockwise-beam direction. The polar angle,  $\theta$ , is measured from the positive  $z$ -axis and the azimuthal angle,  $\phi$ , is measured in the  $x$ - $y$  plane.  $\eta = -\ln \tan(\theta/2)$ . The transverse energy and momentum are defined as  $E_T = E \sin \theta$  and  $p_T = p \sin \theta$  where  $E$  is the energy measured in the tracking system.  $E_T^{\text{miss}} = | - \sum_i E_T^i \vec{n}_i |$  where  $\vec{n}_i$  is a unit vector that points from the interaction vertex to the transverse plane.
- [26] “Timing Distribution at the LHC”, B.G. Taylor Colmar, 9-13 September 2002
- [27] “An FPGA based multiprocessing CPU for Beam Synchronous Timing in CERNs SPS and LHC”. *Proceedings of ICAL EPICS 2003, Gyeongju, Korea ICAL EPICS 2003*
- [28] “Timing and Synchronization in the LHC Experiments”, Varela, J. Krakv, 11-15 September 2000.
- [29] <http://ttc.web.cern.ch/TTC/intro.html>
- [30] “Study of the LHC ghost charge and satellite bunches for luminosity calibration.”, CERN-ATS-Note-2012-029 PERF
- [31] “LHC bunch current normalisation for the April-May 2010 luminosity calibration measurements.”, CERN-ATS-Note-2011-004 PERF
- [32] CMS Collaboration, “The electromagnetic calorimeter. Technical design report”,. CERN-LHCC-97-33
- [33] Bo Lofstedt, “The digital readout system for the CMS electromagnetic Calorimeter”, *Nucl. Inst. Methods in Physics Research*, A 453 (2000) 433-439
- [34] CMS Electromagnetic Calorimeter Collaboration, “Energy resolution of the barrel of the CMS Electromagnetic Calorimeter”, JINST 2(2007)P04004.

- [35] CMS Collaboration, “Time Reconstruction and Performance of the CMS Crystal Electromagnetic Calorimeter”, CFT-09-006, 2009.
- [36] <https://twiki.cern.ch/twiki/bin/viewauth/CMS/ECALDPGTimeCalibration>
- [37] <https://twiki.cern.ch/twiki/bin/viewauth/CMS/ECALDPGHwTimeCalibration>
- [38] CMS Collaboration, “The CMS ECAL performance With examples”, JINST 9 C02008, 2014.
- [39] CMS-DP-2014/011: “*ECAL Timing Performance Run1*”
- [40] <https://twiki.cern.ch/twiki/bin/view/CMSPublic/EcalDPGResultsCMSDP2014011>
- [41] <https://twiki.cern.ch/twiki/bin/view/CMSPublic/EcalDPGResultsCMSDP2014012>
- [42] “Characterization and treatment of anomalous signals in the CMS Electromagnetic Calorimeter” CMS AN AN-10-357
- [43] “ Mitigation of Anomalous APD signals in the CMS ECAL”, 2013, *JINST 8 C03020*, W.Bialas and D.A. Petyt
- [44] CMS Collaboration, “CMS trigger and data taking in 2010 ”, *CMS CR-2011/051*.
- [45] CMS Collaboration, “Reconstruction of the signal amplitude of the CMS electromagnetic Calorimeter”, Eur.Phys.J. C46S1(2006)23-35.
- [46] D.del Re et al “An algorithm for the determination of the flight path of long-lived particles decaying into photons” CMS AN -2010/212.
- [47] CMS Collaboration, “Particle-Flow Event Reconstruction in CMS and Performance for Jets, taus and  $\cancel{E}_T$ ”, CMS Physics Analysis Summary CMS-PAS-PFT-09-001(2009).
- [48] CMS Collaboration, Missing Transverse Energy Performance in Minimum-Bias and Jet Events from Proton-Proton Collisions at  $\sqrt{s} = 7$  TeV , CMS Physics Analysis Summary CMS-PAS-JME-10-004 (2010).
- [49] MET JINST (arXiv:1106.5048)

- [50] CMS Collaboration, “Missing transverse energy performance of the CMS detector”; arXiv:1106.5048v1
- [51] ISAJET 7.84 F.E. Paige, S.D. Protopopescu, H. Baer and X. Tata, <http://www.nhn.ou.edu/~isajet/>
- [52] T. Sjstrand, S. Mrenna, and P. Skands, PYTHIA 6.4 physics and manual, JHEP 05 (2006) 026, doi:10.1088/1126-6708/2006/05/026, arXiv:hep-ph/0603175
- [53] GEANT4 Collaboration, GEANT4a simulation toolkit, Nucl. Instrum. Meth. A 506(2003) 250, doi:10.1016/S0168-9002(03)01368-8.
- [54] CMS Collaboration, “Determination of Jet Energy Scale in CMS with pp collisions at  $\sqrt{S} = 8$  TeV”, *JME-10-010(2012)*
- [55] “<https://twiki.cern.ch/twiki/bin/viewauth/CMS/EGamma2012>.”
- [56] CMS Collaboration, “Search for ADD Extra-dimensions with Photon + MET signature”, *AN-11-319(2011)*
- [57] “Parton distributions for the LHC” Eur.Phys.J C63(2009) 189-285 or arXiv:0901.0002
- [58] “Presentation of search results: the CLs technique”, *A. L. Read 2002 J. Phys. G: Nucl. Part. Phys. 28 2693*
- [59] “Computation of confidence levels for search experiments with fractional event counting and the treatment of systematic errors”, *Peter Bock JHEP01(2007)080*
- [60] <https://twiki.cern.ch/twiki/bin/viewauth/CMS/>
- [61] “Asymptotic formulae for likelihood-based tests of new physics” *G. Cowan et al, arXiv:1007.1727v3*
- [62] CMS Collaboration, “CMS Physics: Technical design report, Volume 2” CERN-LHCC-2006-001.

## Appendix A

# Glossary and Acronyms

Care has been taken in this thesis to minimize the use of jargon and acronyms, but this cannot always be achieved. This appendix defines jargon terms in a glossary, and contains a table of acronyms and their meaning.

### A.1 Glossary

- **Cosmic-Ray Muon (CR  $\mu$ )** – A muon coming from the abundant energetic particles originating outside of the Earth’s atmosphere.
- **SUSY** – A theoretical model based on a fundamental symmetry called supersymmetry in which the fermions and bosons can exchange their spin, extending the standard model to account for the stability in the observed Higgs boson mass and to also predicting the existence of many extra new particles which could be candidates of dark matter.

### A.2 Acronyms

Table A.1: Acronyms

NMLLP	Neutral Massive Long-Lived Particles.
DM	Dark Matter.
DE	Dark Energy.
GMSB	Gauge Mediated Supersymmetry Breaking
LHC	Large Hadron Collider
CMS	Compact Muon Solenoid
CR $\mu$	Cosmic-Ray Muon